

Unravelling the roles of an alternatively spliced microexon in Daam1 in nervous system development and function

Patryk Poliński

TESI DOCTORAL UPF / 2021

Thesis supervisor

Dr. Manuel Irimia Martinez

Systems Biology Department

Centre for Genomic Regulation (CRG)

UNIVERSITAT POMPEU FABRA

DEPARTMENT OF EXPERIMENTAL AND HEALTH SCIENCES



Abbreviations

-MIC - microexon lacking isoform
+MIC - microexon containing isoform
° - degree
°C - degree Celsius
a.u. - arbitrary unit
aa - amino acid
ABP - actin-binding proteins
AD - Alzheimer's disease
ADHD - attention-deficit hyperactivity disorder
AMPA - α -amino-3-hydroxy-5-methyl-4-isoxazole propionic acid
ANOVA - Analysis of Variance
Arc - Activity-regulated cytoskeleton-associated protein
Arp2/3 - Actin Related Protein 2/3 complex
AS - Alternative splicing
ASD - Autistic Spectrum Disorders
ATP - Adenosine triphosphate
AZ - Active zone
Bta - Bos taurus (cow)
Ca²⁺ - Calcium ion
CaMKII - Calcium/calmodulin-dependent protein kinase type II
CC - coiled coil
cDNA - coding DNA
cm - centimeter
Cmi - Callorhynchus milii (elephant shark)
CRG - Centre for Genomic Regulation
CRISPR-Cas9 - clustered regularly interspaced short palindromic repeats and CRISPR-associated protein 9
cRPKM - Reads Per Kilobase Million
d2 - discrimination index
Da - dalton
DAAM1 - Dishevelled Associated Activator Of Morphogenesis 1
DAD - Diaphanous-autoregulatory domain
DAPI - 4',6-diamidino-2-phenylindole
DD - dimerization domain
DG - dentate gyrus
DID - Diaphanous-inhibitory domain
DIV - day in vitro
Dkk1 - Dickkopf-1
Dre - Danio rerio (zebrafish)
DRF - Diaphanous-related formin
Dvl - dishevelled
EBs - embryoid bodies
eIF4G - Eukaryotic translation initiation factor 4G
eMIC - Enhancer of microexons
et al. - and others
F-actin - fibrous actin

FH2 - Formin-homology-2
FPLC - fast protein liquid chromatography
Fura-2AM - Fura-2-acetoxymethyl ester
Fz - Frizzled
g - gram
G-actin - globular actin
GBD - GTPase-binding domain
gDNA – genomic DNA
GFP - Green fluorescent protein
Gga - Gallus gallus (chicken)
GO – Gene Ontology
gRNA – CRISPR-Cas9 guide RNA
GSEA – Gene Set Enrichment Analysis
h - hour
hAGT - human O6-alkylguanine-DNA-alkyltransferase
HD - Huntington's disease
HET - Heterozygous
HOMO- Homozygous
Hsa - Homo sapiens (human)
IEG - immediate early gene
IgG - Immunoglobulin G
IHC - Immunohistochemistry
IPTG - Isopropyl β - d-1-thiogalactopyranoside
IR – Intron retention
KO – Knockout
LatA - Latrunculin A
LTD - Long Term Depression
LTP - Long Term Potentiation
m - meter
M - molarity
Mdo - Monodelphis domestica (opossum)
mESC - murine Embryonic Stem Cells
MIC – Microexon
min - minute
mm - millimeter
Mmu - Mus musculus (mouse)
MWM - Morris Water Maze
n - nano
ND - neuronal differentiation
NMDA - N-methyl-D-aspartate
NOR - Novel Object Recognition
NPC – Neural progenitor cells
nt - Nucleotide
p – p-value
PCA - Principal Component Analysis
Pclo - Piccolo
PCR – Polymerase chain reaction
PD - postnatal day
PDB - Protein Data Bank

PhD - Doctor of Philosophy
PKA - Protein Kinase A
PPI - protein-protein interaction
PSD - postsynaptic density
PSI - percent spliced in
PTV - Piccolo-Bassoon transport vesicles
RA - retinoic acid
RNA - Ribonucleic acid
RNA-seq - RNA sequencing
ROI - regions of interest
RP - Reserve pool
rpm - revolutions per minute
RRP - readily releasable pool
RT-PCR – Reverse transcription polymerase chain
SD - standard deviation
SDS-PAGE - sodium dodecyl sulfate-polyacrylamide gel electrophoresis
sec - second
Srrm4 - Serine/Arginine Repetitive Matrix 4
SV - Synaptic Vesicle
Syp-1 - Synaptonemal complex protein
TIRF - total internal reflection fluorescence
UV-Vis - UltraViolet-Visible Spectroscopy
WT – wild-type
Xtr - *Xenopus tropicalis* (clawed frog)
 α - Alpha
 β - Beta
 Δ - Delta
 μ - Micro

Abstract

Microexons are an unusual form of alternative splicing with high evolutionary conservation, however, their functions are still far from being understood. In this thesis, we focused on a neuronal-specific microexon that modulates the structure of the FH2 domain of DAAM1, a protein important for actin dynamics. We demonstrated that microexon inclusion directly impacts actin nucleation and polymerization capabilities of the FH2 domain, suggesting a modulatory effect on DAAM1's function. Actin dynamics is an important factor in neuronal differentiation and function. Our studies demonstrated higher neuronal activity upon microexon removal, both in an *in vitro* system of differentiated glutamatergic neurons and *in vivo*, in a microexon KO mouse model. This presumably synaptic-driven phenotype translated into further developmental imbalances in young mice, and later on, motor and learning impairments in adulthood. These results thus reveal a highly conserved and splicing-driven control mechanism of neuronal functioning, involved in higher cognitive abilities.

Resumen

Los microexones son una forma inusual de empalme alternativo con alta conservación evolutiva, sin embargo, sus funciones aún están lejos de entenderse. En esta tesis, nos centramos en un microexón neuronal específico que modula la estructura del dominio FH2 de DAAM1, una proteína importante para la dinámica de la actina. Demostramos que la inclusión de microexones impacta directamente en las capacidades de nucleación y polimerización de actina del dominio FH2, lo que sugiere un efecto modulador sobre la función de DAAM1. La dinámica de la actina es un factor importante en la diferenciación y función neuronal. Nuestros estudios demostraron una mayor actividad neuronal tras la eliminación de microexones, tanto en un sistema in vitro de neuronas glutamatérgicas diferenciadas como in vivo, en un modelo de ratón de microexón KO. Este fenotipo presuntamente impulsado por la sináptica se tradujo en más desequilibrios del desarrollo en ratones jóvenes y, más tarde, en deficiencias motoras y de aprendizaje en la edad adulta. Por lo tanto, estos resultados revelan un mecanismo de control del funcionamiento neuronal altamente conservado e impulsado por empalme, involucrado en capacidades cognitivas superiores.

Table of contents

Abbreviations
Abstract
Resumen

Table of contents

Introduction	1
The human brain is a highly complex structure	1
Neurogenesis in early development gives rise to brain complexity	3
The cytoskeleton plays a key role in neurogenesis	6
Actin-binding proteins modulate actin dynamics	12
The role of actin in early neuronal development	19
The role of actin in synapse formation and functioning	23
6.1 Synapse formation	23
6.2 Presynapse organization and functioning	27
6.3 Organization of the postsynaptic cytoskeleton	30
The role of actin in memory formation	31
As described above actin and ABPs are crucial proteins for many aspects of neurogenesis together with establishment of synaptic connectivity and memory formation. In the last Chapter of this Introduction we will focus on possible regulatory mechanisms controlling neurogenesis.	34
Alternative splicing is a molecular mechanism contributing to brain complexity	35
Objectives	45
Results	49
Molecular analysis of DAAM1	49
DAAM1 gene expression	49
DAAM1 structure and mode of action	52
Alternative splicing of DAAM1	54
Structural impact of microexon insertion in DAAM1	59
DAAM1 microexon misregulation in human neurological disorders	61
DAAM1 microexon impacts the biochemical function of the FH2 domain	63
Actin polymerization assay	64
TIRF microscopy of actin polymerization	75
Dual TIRF microscopy with SNAP labelling	81
Role of the Daam1 microexon in neuronal differentiation and functioning	89
Cell line preparation and neuronal differentiation	89

Impact of Daam1 microexon removal on early neurogenesis	91
Increased neuronal activity upon microexon removal	98
Roles of Daam1's microexon in nervous system development	105
Mice postnatal neuromotor development	108
a) Pivoting and walking analysis	108
b) Hindlimb and forelimb strength assessment	110
c) Negative Geotaxis	111
d) Grasping reflex, Prayers reflex and cliff aversion	115
Molecular analysis of the Daam1 KO mice	117
a) Axon guidance	117
b) Hippocampal structure and activity analysis	118
b) Bioinformatic analysis of the hippocampal RNA-seq	120
Neurological alterations upon Daam1 microexon KO in adult mice	125
Activity, motor coordination and balance	126
a) Grip Strength	126
b) Beam Balance	128
c) Rotating Rod (Rotarod)	130
d) Open Cage	132
e) Actimeter	134
f) Elevated Plus Maze	136
Learning and memory formation	138
a) Novel Object Recognition (NOR)	138
b) Morris Water Maze (MWM)	142
Discussion	149
Conclusions	157
Materials and Methods	159
Bibliography	177

Introduction

Introduction

1. The human brain is a highly complex structure

The brain is a complex system that through temporal as well as structural organization results in the development of higher functions. Thought, will, imagination, sensation, as well as memory, have been acquired by an evolutionarily driven ensemble of ca. 170 billion cells (in a human, adult male brain; Azevedo et al., 2009; Niven and Laughlin, 2008). Although many brain regions have been described and studied, a full understanding of their function, inter-communication as well as importance is still far from complete.

Hippocampus is a part of the temporal lobe, embedded deep into the brain's structure, and can be divided into two main parts: cornu ammonis and dentate gyrus (DG) (Anand and Dhikav, 2012). The first description of the hippocampus, showing its structural complexity, was performed by Santiago Ramón y Cajal (Figure 1). This was possible by adapting the Golgi's staining method, where the usage of silver nitrate and potassium dichromate allowed the staining of random brain cells. This simple yet revolutionary experiment allowed the description of microscopic structures, revealing the complexity of different brain regions, their organization and compositional differences. Work on the hippocampus and the entire nervous system structure granted Santiago Ramón y Cajal the title of the father of modern

neuroscience and, in 1906, a shared scientific Nobel Prize with Camillo Golgi.

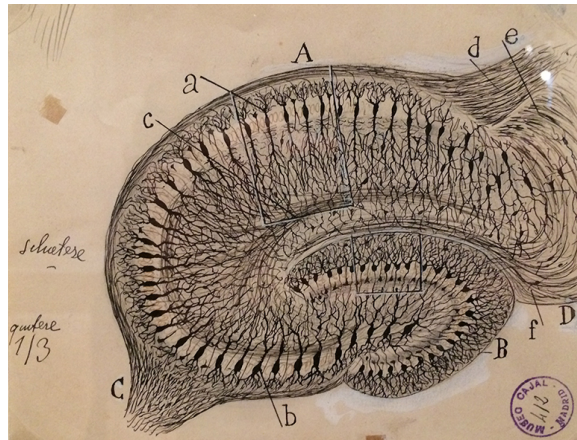


Figure 1. Drawing of the neural circuitry of the rodent hippocampus. By Santiago Ramón y Cajal.

Today our understanding of the brain has greatly advanced. However, the importance and function of particular neuronal cell types, their maturation, spatial and temporal connectivity as well as their role in memory formation is under constant investigation. So far, the most studied brain in human history belongs to H.M., a patient that in 1953 had the majority of his hippocampus removed by a world-class neurosurgeon. Together with hippocampal loss, H.M. lost all of his memories as well as the ability to save and retrieve new ones (Corkin, 2002). This unfortunate yet extraordinary example is one of many cases that took us a step closer in understanding the functioning and complexity of our brain. More importantly, today's advances in molecular biology techniques allow us to gain insights into the molecular regulation of the aforementioned processes, which is at the core of this Thesis.

2. Neurogenesis in early development gives rise to brain complexity

Brain complexity has its origins in neurogenesis, a developmental process during which new neurons are formed. Before the onset of neurogenesis, neuroepithelial stem cells proliferate constantly and rapidly, exponentially increasing the density and the size of the ventricular zone (Figure 2). This process continues until neurogenesis starts, triggered by a tightly controlled switch from symmetric to asymmetric division. This asymmetric division gives up to two different cell types: radial glia cells and commonly, intermediate progenitor cells. In humans, neurogenesis starts around the 5th week of gestation (Budday et al., 2015) and proceeds (in some brain regions, like the hippocampus) throughout the whole life (Kozareva et al., 2019).

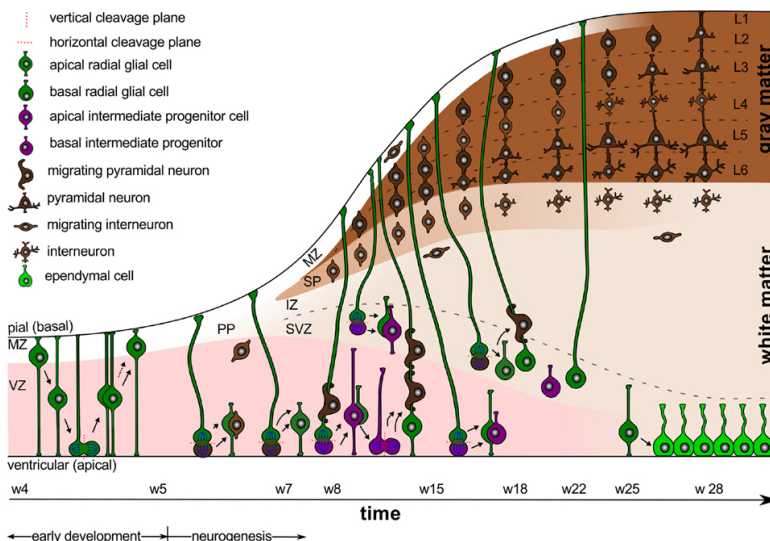


Figure 2. Schematic representation of neurogenesis timeline. Adapted from Budday 2015

Radial glial cells give rise to further intermediate progenitor cells and together, by asymmetric division, drive cortical expansion and subsequent brain folding. The intermediate progenitor cells produce pyramidal neurons, which migrate outward creating the typical six-layered cortical structure (Budday et al., 2015). The formation of the grey matter layers (L1-L6) is a long process that finishes around the 22nd week of gestation. Then, the most important time for neuronal differentiation begins. Until around the 38th week, the cortical neurons elongate their axons and dendrites and form intercellular connections called synapses. At the same time, radial glial cells continue to divide, commonly differentiating into glial cells. These mitotic events constantly increase cortical tension and support further cortical folding (Budday et al., 2015).

To simplify this complex cascade of events La Rosa et al., 2020 described four stages of neurogenesis: 1) cell division, 2) migration, 3) differentiation with maturation, and 4) integration into the cellular network. This simplified description illustrates the main spatiotemporal and cellular challenges to which a future neuron has to adapt. Cell division and migration require constant regulation of the cell's polarity and shape. Moreover, neuronal axon guidance, axon-dendrite polarity formation, the establishment of synaptic connections and integration into the neural network all strongly depend on the dynamic crosstalk of cytoskeletal proteins and their regulators.

In the next chapters of this Introduction, I will explicitly focus on the cytoskeleton as a key player in neurogenesis. More specifically, I will try to shed light on the cytoskeletal changes that drive the neurogenetic processes, with particular focus on actin as its main driver. Additionally, I will expand this knowledge with alternative splicing and memory formation, two processes that are the main focus of this thesis.

3. The cytoskeleton plays a key role in neurogenesis

The cytoskeleton is a dynamic and structurally complex ensemble of protein filaments that plays a key role in cellular morphology. The main cytoskeletal components are actin, microtubules and intermediate filaments. As described above, they are the key elements responsible for withstanding environmental stimuli but also actively generate cellular forces essential to adapt and respond to those stimuli.

Microtubules are stiff and round-shaped tubulin polymers with the ability to elongate or shrink. Self-assembly of tubulin dimers is accomplished in the presence of GTP. These hollow tubes are mainly responsible for the establishment of cellular polarity during migration due to their charged character. Additionally, microtubules are essential for cargo distribution and chromosome segregation during cell division (Dogterom and Koenderink, 2019).

The main **Actin** monomer is a globular protein of around 42 kDa called G-actin, composed of 4 subdomains (SD1-4) that form a characteristic groove (Figure 3 left panel) and an ATP binding site (Pollard, 2016). ATP hydrolysis provides the energy that allows the G-actin monomers to nucleate and subsequently polymerize into an F-actin filament. In its steady-state, F-actin preferentially polymerizes at the barbed end (net plus charge; (+)), while the opposite side, the pointed end (net minus charge; (-)), has a net loss of the G-actin monomers (Figure 3 right panel).

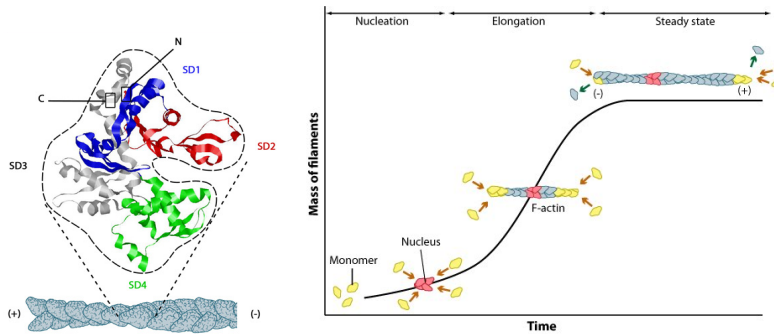


Figure 3. Actin structure and polymerization. Left panel describes the actin structure and ensemble of G-actin monomers in the F-actin filament. Actin orientation forms polarity in a steady-state. SD1-4 are consecutive actin subdomains (PDB file: [1ATN](https://www.rcsb.org/structure/1ATN)). Right panel depicts actin polymerization dynamics in the unit of time. Consecutive phases of nucleation, elongation and steady-state have been described. Adapted from <https://www.mechanobio.info/>

In comparison to microtubules, actin is a thinner and highly flexible structure. These two features are essential aspects, which give actin its dynamic character and are important to rapidly respond to the changing environment. Another key feature of actin is its versatility. Actin can easily form higher-order structures, including complex networks of many shapes and functions, accomplished by bundling and crosslinking of actin filaments (Dogterom and Koenderink, 2019).

In a cell, many context-specific molecular players are involved in the “communication” between the aforementioned cytoskeleton subcomponents (i.e. microtubules and actin). Figure 4 describes some examples of the cytoskeletal crosstalk. Actin nucleation factors (such as formins) can associate with microtubules and lead to actin polymerization (Figure 4A). This situation might occur at

the cellular protrusions where stiff microtubules create mechanical support, but also offer active sites of actin polymerization (Figure 4B). Additionally, the crosstalk process can be tightly controlled by shared regulators (Figure 4C). The RHO family of small GTPases is a good example of this control, with some members of this family interacting directly with both microtubule and actin-associated proteins and regulating their activity.

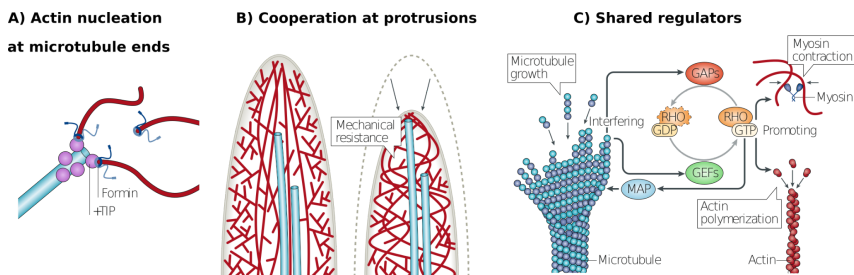


Figure 4. Examples of cytoskeleton crosstalk. A) Formin regulated actin-microtubule crosstalk at microtubule ends. B) Actin-microtubule crosstalk at the cellular protrusions. Stiff microtubules create a mechanical resistance supporting actin function. B) Small GTPases of RHO family directly regulate both actin and microtubule dynamics. Figure adapted from Dogterom and Koenderink 2019

A perfect example of a dynamic interplay between the cytoskeleton and actin and actin-binding-proteins (ABPs) can be described by a current model of filopodia formation (Figure 5). Formation of filopodia starts with an increased actin filament concentration. Here, formin proteins (i.e. Daam1) allow elongation of preexisting actin fibers and nucleation of new ones (Figure 5A). Additional elongation by actin elongating proteins (i.e. ENA/VASP) creates tension that deforms the plasma membrane. Many ABPs support structural coherence by crosslinking and filament support (Figure

5B). Finally, introduction of Fascin allows formation of stiff filament bundles that are further elongated by formin proteins allowing filopodia extension (Figure 5C). Additionally, microtubules can enter the filopodia in order to support actin structures against mechanical resistance (Mattila and Lappalainen, 2008; Papandréou and Leterrier, 2018).

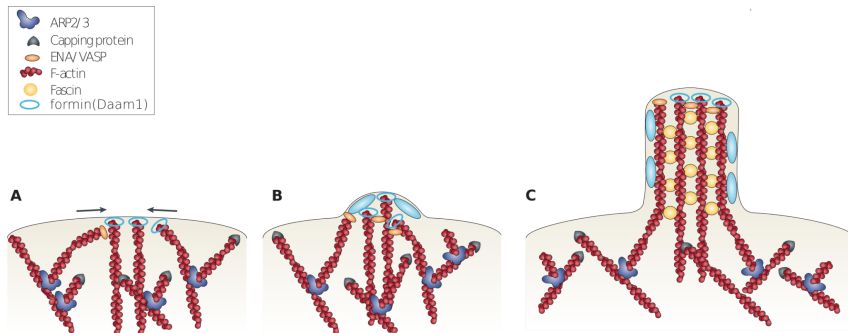


Figure 5. Schematic representation of filopodia formation model. A) Filopodia formation starts with high concentration of actin and actin binding proteins (ABPs) by the plasma membrane. B) Filopodia elongation occurs when formin proteins like Daam1 elongate existing actin fibers and nucleate new ones. C) Consecutively, structural integrity is formed by actin crosslinking proteins. This creates further mechanical resistance of the filopodia. Adapted from Mattila and Lappalainen, 2008

As described above, the cytoskeleton is characterized by a constant interplay between its subcomponents and interacting proteins. This interplay and especially its spatiotemporal control are key aspects for cellular processes like migration during neurogenesis. During migration, microtubules anchor their plus ends outside from the nucleus towards the cell boundaries, while the minus end is anchored at the centrosome (blue, Figure 6A). The main role of microtubules is mechanical stabilization and the formation of directionality. On the contrary, actin is mostly found at the

periphery of the cell where the leading edge of a migrating cell depends on different actin-filament based structures, lamellipodia and filopodia (red, Figure 6A and B). Protruding filopodia contain mainly F-actin filaments (as described in Figure 5) with their elongating barbed ends orientated towards the plasma membrane (Mattila and Lappalainen, 2008). Additional traction is provided by the focal adhesion of actin stress fibres to the extracellular matrix (green, Figure 6A and B). This polarized morphology generates the forces required for cell movement.

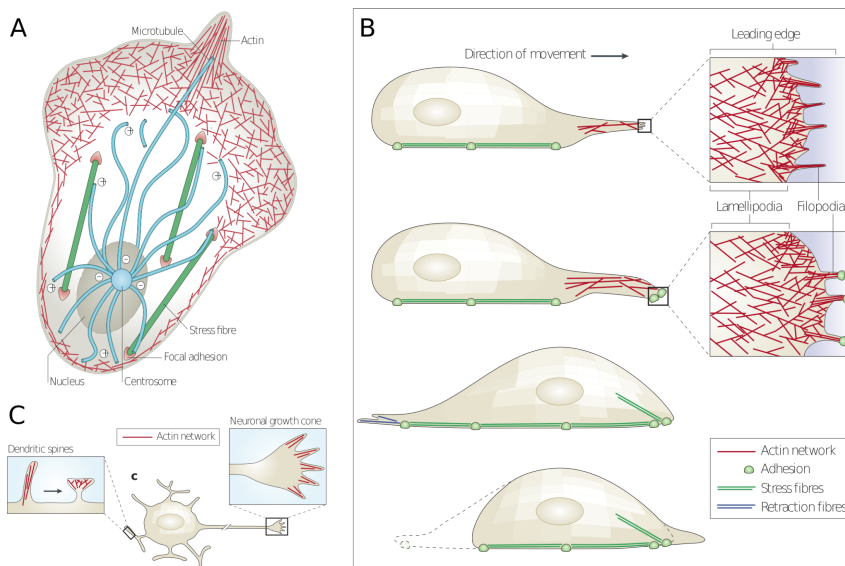


Figure 6. Actin based filopodia are important in cellular migration and neurogenesis related processes. A) Cytoskeletal crosstalk during the migration process. B) Actin based structures drive cellular migration. C) Examples of filopodia in neuronal cells are actin dependent. Adapted from Dogterom and Koenderink 2019 and Mattila and Lappalainen 2008

Like cell migration, many aspects of neurogenesis depend on the actin cytoskeleton All of which are probably driven by similar processes described above. During neuronal growth cone movement, similar lamellipodial and filopodial behaviour have been described (Figure 6C) (Da Silva and Dotti, 2002). Similarly, actin-based protrusions are thought to be responsible for synaptic spine development and consecutive synapse formation.

Till this day a complete understanding of actin behaviour and the role of ABPs in the aforementioned processes remains elusive. This is mainly due to key actin features like flexibility and small size, that allow its rapid spatiotemporal environmental response, but at the same time make it highly difficult to study. However, with the recent development of microscopy techniques and live-cell imaging, the importance of actin and ABP in neurogenesis, growth cone pathfinding, neuronal synapse formation and functioning has finally started to become clearer. I will discuss all these processes in more detail in the following chapters, but I will start with a thorough description of ABPs in the next chapter.

4. Actin-binding proteins modulate actin dynamics

As demonstrated in the previous chapter, actin is a major cytoskeletal component driving neurogenesis. In general, actin action can be modulated by the interaction with other proteins. For instance, actin-binding proteins (ABPs) are molecular motors responsible for actin turnover control and cytoskeletal crosstalk. So far, many ABPs have been described and their classification depends on the mode of action (Figure 7).

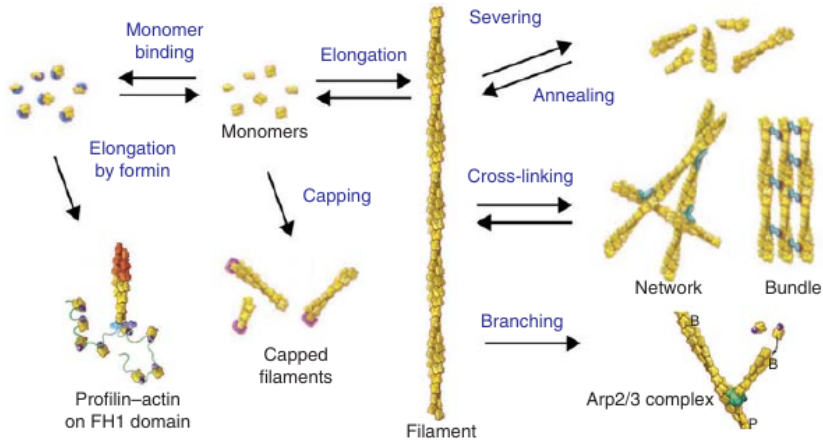


Figure 7. Classification of actin-binding proteins (ABPs) based on their mode of action. Adapted from Pollard, 2016

The main categories in which ABPs can be classified are:

- **Actin monomer binding** proteins, like profilin, facilitate polymerization.
- **Actin filament severing proteins**, like cofilin or gelsolin family, fragment actin filaments
- **Filament binding proteins**, like tropomyosin, protect actin filaments from severing or facilitate interaction with myosins.
- **Cross-linking proteins**, like fascin, stabilize higher-order structures.
- **Capping proteins**, like CAPZA, bind actin barbed ends limiting their growth.
- **Actin nucleating proteins** are the main types of machinery driving the dynamics of the motile cells (Mattila and Lappalainen, 2008). This is the most heterogeneous group of ABPs and consists of the **WH2-containing nucleators**, the **Arp2/3 complex** responsible for actin branching (Figure 8A), and **formins** that nucleate linear filament formation and elongation (Figure 8B).

Many ABPs have been found to play critical roles in neurogenesis and neuronal maturation. However, considering the versatile role of actin nucleating proteins in their mode of action, this ABP sub-group seems to be crucial in neuronal development and functioning. For instance, deficiency of the Arp2/3 complex has been associated with impairments in axon branching and dendritic spine maturation (Jung et al., 2020). Cordon-bleu (Cobl), a

WH2-containing nucleator, was also found to be involved in the neurite development processes and neuronal morphology (Ahuja et al., 2007). Formins seem to be the most versatile ABP family in their mode of action. Recent studies show the involvement of formins not only in actin nucleation and barbed end elongation but also in bundling (Jaiswal et al., 2013) and crosstalk with other cytoskeleton proteins (Foldi et al., 2017).

Interestingly, our understanding of the differences and the mode of action between actin nucleating proteins comes mainly from the *in vitro* studies. Numerous *in vitro* assays have been developed to study actin dynamics and the role of the ABPs in these processes. One example is the pyrenyl-actin assay, a standard spectroscopic experiment in which pyrene-labelled actin gains fluorescence during the G-actin monomer/F-actin filament transition (Figure 8C, left panel). This assay allows the measurement of the general polymerization kinetics, yet it does not provide any information about its molecular and structural basis. The main differences between actin nucleating proteins became clearer by the transition from pyrenyl-assay to microscopy-based techniques (Figure 8C, right panel). Another assay is the total internal reflection fluorescence (TIRF) microscopy. It has become the technique of choice to study the in-detail impact of ABPs on actin polymerization, showing detailed spatiotemporal behaviour in real-time (Breitsprecher et al., 2009).

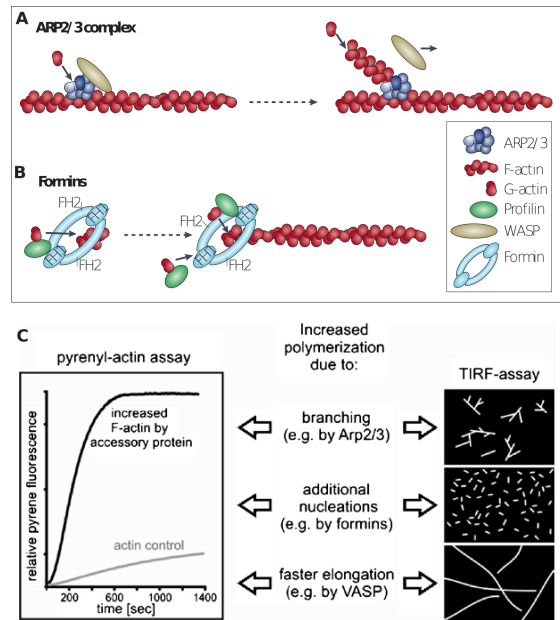


Figure 8. Heterogeneity in mode of action of actin nucleating proteins. a) Comparison of Pyrenyl-actin assay and Total internal reflection fluorescence (TIRF) microscopy to study impact of ABPs on actin nucleation and polymerization. b) Mode of action of Arp2/3 complex in F-actin filament branching and WH2 domain protein WASP in filament elongation. c) Formin based nucleation and elongation of actin filaments. Adapted from Breitsprecher et al., 2009 and Mattila and Lappalainen 2008 correspondingly.

Interestingly, recent genome-wide studies identify the DAAM1 formin as a potentially important factor in human brain connectivity and structure (van der Lee et al., 2019; Mollink et al., 2019). Considering the emerging roles of actin nucleating proteins in the development and functioning of the nervous system, in the next chapters I will focus specifically on this group of ABPs. Additionally, I will focus on formins, particularly on the aforementioned DAAM1 protein and its recently discovered roles in neurogenesis.

4.1 Formins

The family of formins consists of 8 mammalian sub-families based on their domain architectures (Kühn and Geyer, 2014). Formins are multidomain proteins characterized by a conserved Formin-homology-2 (FH2) domain that forms homodimeric structures directly responsible for processive polymerization of F-actin filaments (Figure 8A). Most of the formins also contain an FH1 domain responsible for Profilin-Actin complexes interaction (Figure 9A). The recruitment of Profilin-Actin complexes from the proximal environment is followed by the delivery of the substrate to the FH2 domain and processive F-Actin polymerization. Additionally, the coiled-coil (CC) domain as well as the dimerization domain (DD), are responsible for the organization of the tertiary structure of the protein (Kühn and Geyer, 2014; Yamashita et al., 2007, Gao and Chen, 2010).

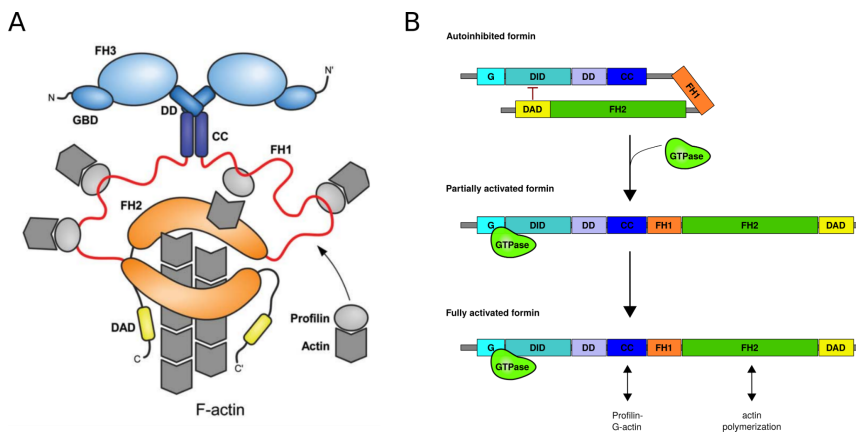


Figure 9. Model of diaphanous related formin (DRF) autoinhibition and functioning. A) Schematic representation of DRFs structural ensemble and mode of action. Adapted from Kühn and Geyer, 2014. B) Schematic

representation of DRF activation. DRF formins exist in an autoinhibited state induced by DAD and DID domain interactions. This state can be released by direct interaction of the G domain with GTPase. Full activation is reached by DRFs dimerization and, profilin-actin complex binding by FH1 domain and subsequent actin polymerization by FH2 domain.

Diaphanous-related formins (DRFs), are one formin sub-group, categorized by the presence of an autoinhibited state caused by the intramolecular interaction between the N-terminal Diaphanous-inhibitory domain (DID) and the C-terminal Diaphanous-autoregulatory domain (DAD) (Figure 9B). This autoinhibitory state can be released by the interaction with small GTPases of the Rho superfamily (more specifically, with GTPase-binding domain (GBD)), which subsequently allows actin nucleation and polymerization (Kühn and Geyer, 2014).

FH2 domain encompasses five substructures known as lasso, linker, knob, coiled-coil and post subdomain (Figure 10). Homodimerization of the FH2 domain drives actin polymerization. Head to tail interaction of a lasso from one monomer wraps around the post domain of the second unit forming a ring around the fast-growing barbed end of an actin filament (Kühn and Geyer, 2014; Otomo et al., 2005). This particular “tethered dimer“ exists at two states in equilibrium: one allowing the actin-binding and one allowing the dissociation. In this mechanism, the interconversion between the two states is crucial for actin polymerization (Otomo et al., 2005). This interconversion is allowed due to FH2 ring expansion and the high flexibility of the linker region.

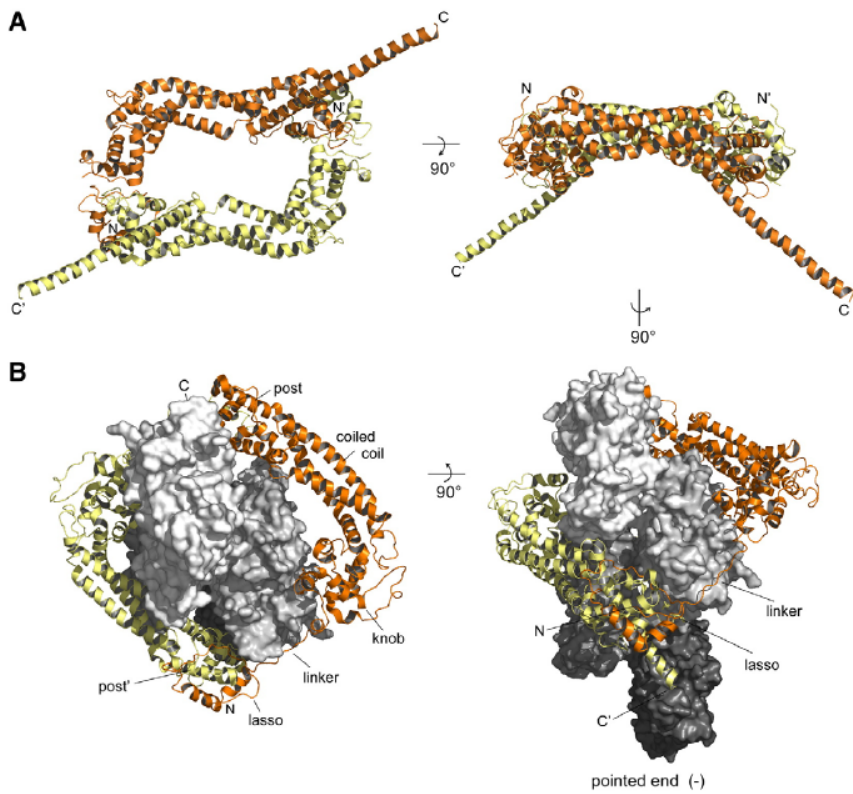


Figure 10. Crystal structure of FH2 domain homodimer. A) Head-to-tail assembly of human DAAM1 homodimer in free form (PDB: 2J1D). B) Similar to DAAM1 FH2, homodimer of Bni1 bound to actin (PDB: 1Y64). Adapted from Schönichen and Geyer, 2010

5. The role of actin in early neuronal development

The first steps of neurogenesis include the transition from radial glia to intermediate progenitors and, later on, to interneurons. These stages of neuronal differentiation have been well characterized in a controlled *in vitro* environment of primary hippocampal neurons, where three initial stages have been described: initial budding, neurite formation, and polarization (Figure 11) (Da Silva and Dotti, 2002).

During the initial budding stage, the symmetry of the round neuronal sphere is broken by a protruding, actin-driven filopodium. Lamellipodia start to form in all of the directions and the protruding edges are responsible for probing the environment. Filopodia can either extend into growth cone-like structures or be completely retracted in a dynamic back-and-forth movement. This process is still far from being understood, especially because of the limitations of the *in vitro* cell cultures that mostly lack extrinsic forces (Da Silva and Dotti, 2002; Leterrier et al., 2017).

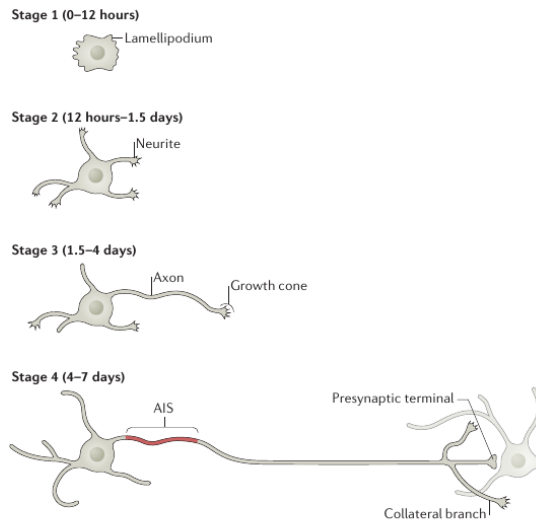


Figure 11. Development of hippocampal neurons in culture. Stage 1 of neuritogenesis starts with the formation of actin-based lamellipodial structures and consecutive extension of filopodia. During Stage 2 filopodia extend to neurites that can be retracted or extended. Clear extension and speciation of one neurite into axon marks Stage 3. Stage 4, the tip of the growing growth cone establishes synaptic connections with dendrites of other neurons. Adapted from Leterrier et al., 2017

Depending on the neuronal type, and the distance traveled *in vivo*, it was shown that a future neuron can have no leading-edge, one or multiple neurites. In cultured hippocampal neurons as a next step, the cell undergoes a significant change, with one of the neurites extending rapidly and becoming the axon, and dendrites usually developing at the later stages (Da Silva and Dotti, 2002; Leterrier et al., 2017).

A variety of extracellular signals have been shown to drive neurite and growth cone navigation. From local calcium concentrations (Gasperini, 2017), adhesion molecules like laminin, through extracellular proteins, and soluble molecules (Da Silva and Dotti, 2002). Nevertheless, more and more evidence highlights the importance of actin-binding proteins (ABP) and especially formin protein family, as key proteins driving the process of actin filament formation and growth cone movements (Foldi et al., 2017). Recently, in *Drosophila* primary neurons, the formin DAAM has been found to be responsible for filopodia integrity (Matusek et al., 2008). Additionally, Jaiswal et al. 2013 found that Daam1 protein, in mouse B16F1 cells is present not only at the actin filament barbed end (as other formins) but also along the filopodial shaft. This is probably due to the ability of Daam1 to interact directly with fascin, an actin-bundling protein. Another possible explanation of DAAM1's role in filopodia formation and integrity might be due to the involvement of DAAM in the process of actin-microtubule crosstalk, essential for proper growth cone coordination (Figure 12) (Foldi et al., 2017; Szikora et al., 2017).

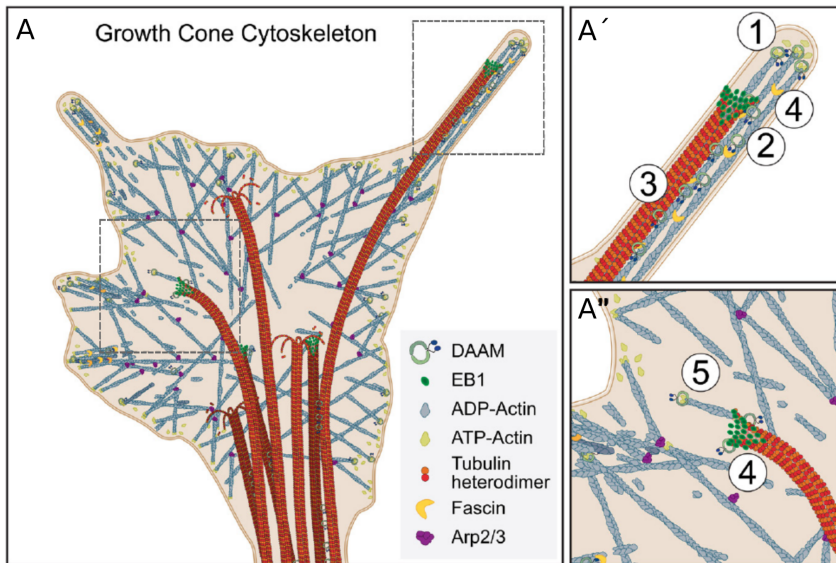


Figure 12. Actin-microtubule crosstalk in the growth cone is regulated by DAAM protein. A) Schematic model of the growth cone cytoskeleton. DAAM1 is proposed to play important roles in 1) actin barbed-end binding, polymerization and actin nucleation, 2) F-actin bundling, 3) F-actin and MT coalignment, 4) EB1 (regulates the dynamics of the microtubule cytoskeleton) binding, 5) facilitated actin filament formation at the MT plus-ends through interactions with EB1. Adapted from Foldi 2017

Interestingly, similar *in vivo* neural growth impairments related to DAAM1, have been found in planaria (Beane et al., 2012), zebrafish (Colombo et al., 2013), and chicken (Avilés and Stoeckli, 2016), further supporting the role of DAAM1 in growth cone morphology and axon guidance.

6. The role of actin in synapse formation and functioning

6.1 Synapse formation

The next steps of growth cone movement depend on its guidance toward its synaptic targets (by specific extracellular cues) and the establishment of functional synapses. Synapses are specialized intercellular connections and can be formed either by growing growth cones or already established segments of an axon (Ziv and Garner, 2004), commonly with the dendrites of another neuron. So far, little is known about the mechanical aspects of synapse formation. Recent findings of actin rings, hotspots, and formin-dependent trails (Ganguly et al., 2015) in mature axons (Leterrier et al., 2017) and dendrites (Konietzny et al., 2017) support the hypothesis that actin and ABPs are in the center of that process. Jung et al., 2020 hypothesize that this process begins with ABP-dependent filopodia initiation, consecutive elongation towards its synaptic target, and finishes at synaptic spine formation, yet exact spatiotemporal behaviour and involved molecules remain elusive (Figure 13).

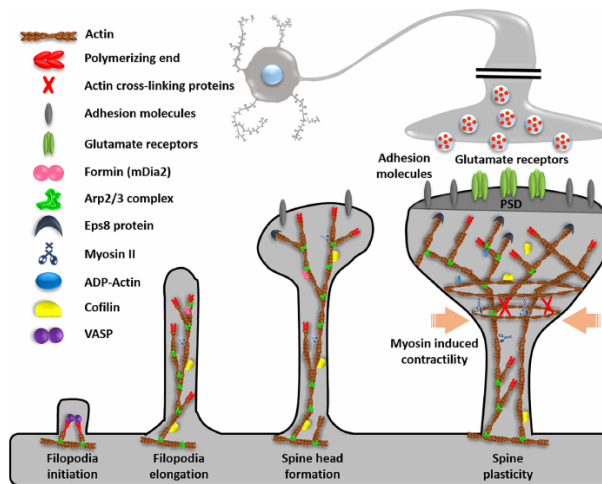


Figure 13. Schematic representation of dendritic spine formation and role of actin and actin-binding proteins (ABP). Spine formation starts by the filopodia initiation driven by the actin nucleators, and its consecutive elongation. Spine head formation and its architectural ensemble depend strongly on actin filaments and their tertiary structures regulated by ABPs. Adapted from Jung et al., 2020

Model presented by Jung et al., was supported by the usage of actin-perturbing agents like Latrunculin A. Latrunculin A (LatA) is a chemical that sequesters G-actin, causing the depletion of available monomers, preventing actin polymerization. LatA has been found to inhibit filopodia formation and synaptogenesis in young, cultured hippocampal neurons (Dillon and Goda, 2005). Interestingly, formin Daam1 was found to be enriched in pre- (Wagh et al., 2015) and postsynaptic (Salomon et al., 2008) spines. Moreover, Daam1 has been recently proven to interact directly with Piccolo, a protein responsible for presynapse organization (Wagh et al., 2015). Based on that discovery, Torres and Inestrosa, 2017 presented a hypothesis which focused on the last steps of the presynapse formation (Figure 14). The authors of the paper place in

the center of the model formin Daam1, a known partner in the Wnt/PCP signalling pathway. In this model Wnt ligand binds to its receptor Frizzled (Fz), subsequently activating intracellular dishevelled (Dvl) which in turn activates Rho and Rac GTPases. In particular, Rho GTPase in this pathway is activated through Daam1 formin that interacts directly with presynaptic organizer Pclo as well as activates Rho-associated kinase Rock inducing further cytoskeletal changes. This model is based on the experimental data proving the role of Wnt3a as well as Wnt7 in the formation of functional presynaptic sites by clustering of presynaptic proteins and recruitment of Synaptic Vesicles (SVs) during synapse formation.

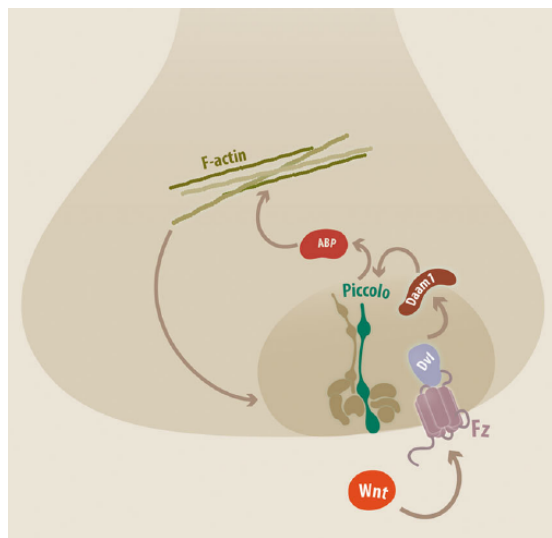


Figure 14. Model of pre-synapse formation and organization. Daam1 is a part of the Wnt PCP pathway and a direct interactor of Pclo protein responsible for cytomatrix at the active zone formation and organization and synapse functioning. Adapted from Torres and Inestrosa, 2017

After successful establishment of the intercellular connections, a functioning synapse is characterized by three main parts, the pre-and the postsynaptic terminals, and the synaptic cleft, a junction between them (Figure 15). Interestingly, in mature neurons, actin has been found to be the most prominent cytoskeletal protein at synapses, being present at both the pre-and the postsynaptic terminals (Cingolani and Goda, 2008). Microtubules do not directly regulate synapse morphology or function, yet microtubule-associated proteins have been implicated in synapse assembly.

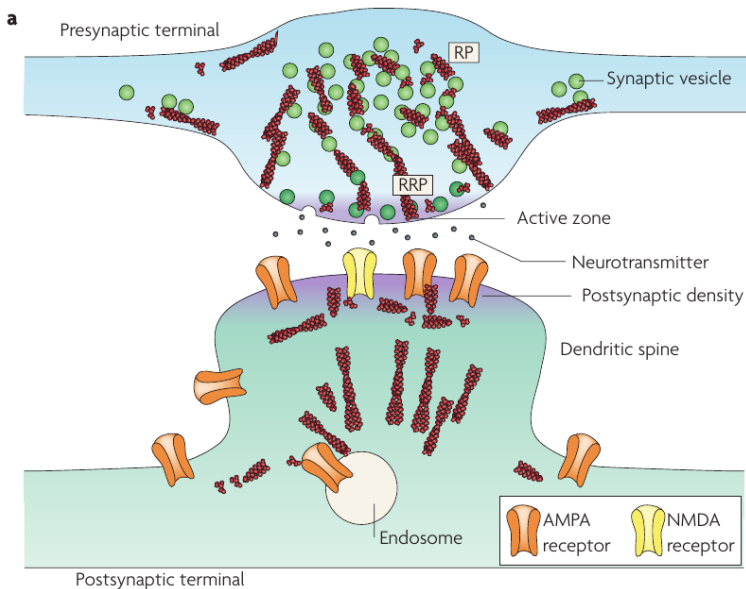


Figure 15. Schematic overview of actin in the synapse. Presynaptic terminal contains actin responsible for the delivery, cycling and spatial separation of synaptic vesicles (SVs). RP - Reserve pool, RRP - readily releasable pool. Actin in the postsynaptic terminal is involved in receptor transfer and clustering. Adapted from Cingolani and Goda, 2008

6.2 Presynapse organization and functioning

The **pre-synapse** is a highly organized structure that can be divided into the active zone and the synaptic head. The active zone (Figure 16 red zone) is a dense region characterized by clustering of multiple specialized proteins responsible for rapid exocytosis. Throughout the head, at least three functionally different synaptic vesicles pools have been described: **readily releasable pool**, with synaptic vesicles (SVs), docked and ready for the release at the active zone, proximal **recycling pool** that maintains and delivers the SVs to the active zone and, and further placed **reserve pool** used only during prolonged exocytosis (Rizzoli and Betz, 2005). Within the presynapse, actin is one of the most abundant proteins and can be found either in monomeric or polymerized states. Figure 16 describes the state of the art model of the presynapse with SVs and actin shown (Wilhelm et al., 2014).

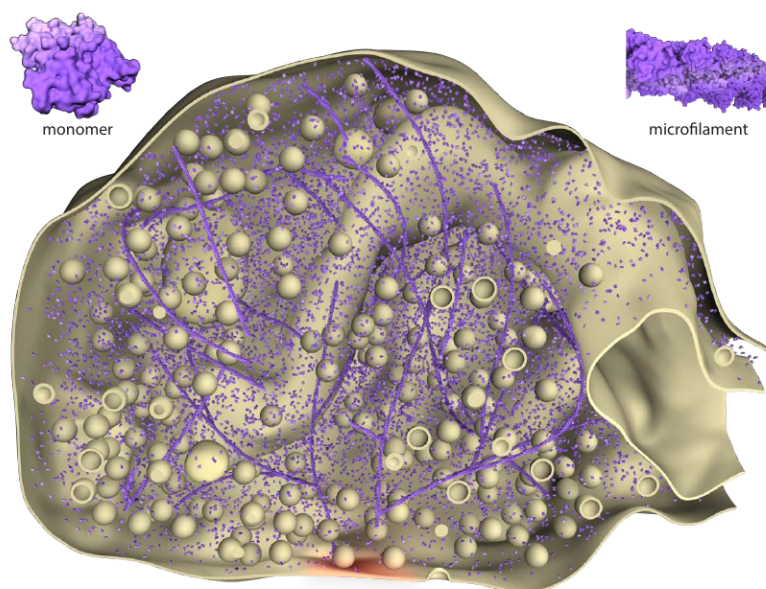


Figure 16. A 3D model of the presynapse indicating actin (violet) in its monomeric and polymerized form. Visible synaptic vesicles (SVs) with 42 nm diameter (average). Adapted from Wilhelm et al. 2014

The presynaptic actin network is involved in the organization of SV pools as well as synaptic vesicle cycling (Dillon and Goda, 2005; Papandréou and Leterrier, 2018). Actin is thought to be responsible for vesicle spatial segregation, specifically by forming a physical barrier that prevents the dispersion of SVs. Here synapsins are thought to link vesicles to the F-actin matrix as they have been found to migrate from presynapse upon latrunculin A treatment (actin filaments depolymerization) as well as neuronal stimulation (Dillon and Goda, 2005).

Actin is also thought to be crucial in the active transfer of SV between the pools upon stimulus, yet this process might be

synapse-dependent and might vary between cell types (Cingolani and Goda, 2008). Figure 16 shows F-actin filaments, forming branched road-like paths that are used to deliver SVs towards the active zone (red region) or from it. Studies performed on chromaffin cells shed light on the mechanistic basis of the synaptic vesicle cycle. Hereupon neuronal stimulation and elevated intracellular Ca^{2+} levels, myosin V has been found to traffic vesicles along F-actin towards the active zone (Cingolani and Goda, 2008). These synaptic vesicles are then primed and docked by the cytomatrix at the active zone machinery and subsequently released upon stimulus. Subsequently, SVs undergo endocytosis, a process that has been recently proven to be mediated by formin-dependent actin assembly (Soykan et al., 2017).

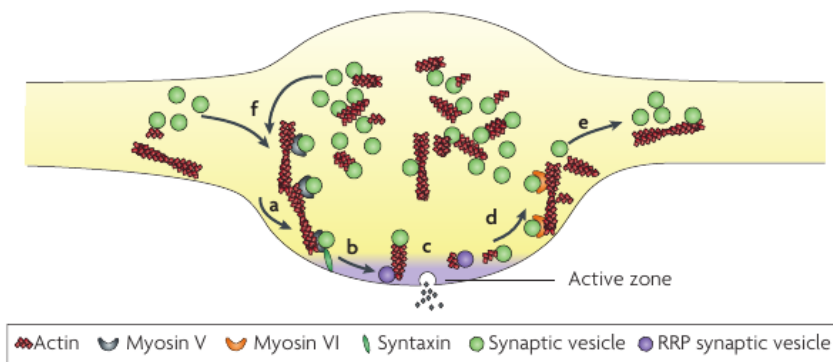


Figure 17. Actin drives the synaptic vesicle cycle. a) F-actin filaments form a path used to deliver synaptic vesicles (SVs) from the recycling pool towards the active zone. b) SVs integrated and primed at the active zone form a readily releasable pool (RRP). c) Upon stimulus SVs from the RRP undergo exocytosis and release neurotransmitters towards the synaptic cleft. d) Actin is involved in the endocytosis of SVs and their recycling. e) recycled synaptic vesicles can be transported out of the presynapse or f) back to the synaptic vesicle cycle. Adapted from Cingolani and Goda, 2008.

6.3 Organization of the postsynaptic cytoskeleton

The cytoskeleton of **postsynaptic** terminals has been mostly characterized in dendritic spines. Here three types of actin networks have been described based on their localization: 1) actin found in the proximity to postsynaptic density (PSD), 2) actin network found throughout the dendritic spines head, and 3) actin in the neck of the spine. Interestingly, neck spine actin is thought to be involved in shaping the morphology of the spine. The other two actin networks have been found to be involved in receptor mobility. Here the receptors can be transported into- or out of- the synapse, towards the PSD. PSD is a similar to AZ dense region of the postsynapse characterized by multiple proteins essential for the signal receiving from the presynapse. Additionally, actin present in the proximity of the PSD is responsible for anchoring and lateral diffusion, allowing modulation of the receptor number. F-actin depolymerization has been found to be connected with AMPA and NMDA receptors dispersion at excitatory synapses and reduced levels of gephyrin at inhibitory synapses (Cingolani and Goda, 2008).

7. The role of actin in memory formation

As described above, actin is a crucial protein, found to be responsible for multiple aspects of synapse functioning. Additionally, actin was found to be a crucial protein in memory formation. Due to the current hypothesis memories are formed by specific connectivity patterns between neurons. This neuronal circuit drives the directionality and strength of synaptic signal transmission using mainly excitatory neurons in a glutamate-dependent process. So far, one of the best-studied factors that can influence synaptic transmission is the morphology of dendritic spines. Dendritic spines can be observed in a variety of shapes, from thin elongated to stubby or mushroom-like (Cingolani and Goda, 2008). Moreover, the presence and the shape of the dendritic spine can be modified throughout its existence, in an experience-dependent plasticity process (Lamprecht, 2021). Synaptic plasticity is directly related to actin turnover and it has been categorized in length dependent way:

Short term plasticity is a synaptic event based on overall actin increase upon a single stimulus. This usually occurs in pre as well as post-synapse and subsequently returns to the basal state circa 5 min post-stimulation.

Long term plasticity is described as persistent synaptic reorganization upon changes related to the actin cytoskeleton. This can be stable between days or even months, depending on the strength of the initial stimulus and its later usage.

Subsequently, processes that induce long term spine modifications have been divided into (Figure 17):

- **Long Term Potentiation (LTP)** is a long-lasting process that shifts the G-actin/F-actin ratio toward F-actin in dendritic spines usually resulting in a stable spine volume increase.
- **Long Term Depression (LTD)** is genuinely described as deterioration or a synaptic weakening and occurs upon the persistently weak neuronal activity or its lack. This is related to an increase in the G-actin ratio and dendritic spine reduction.

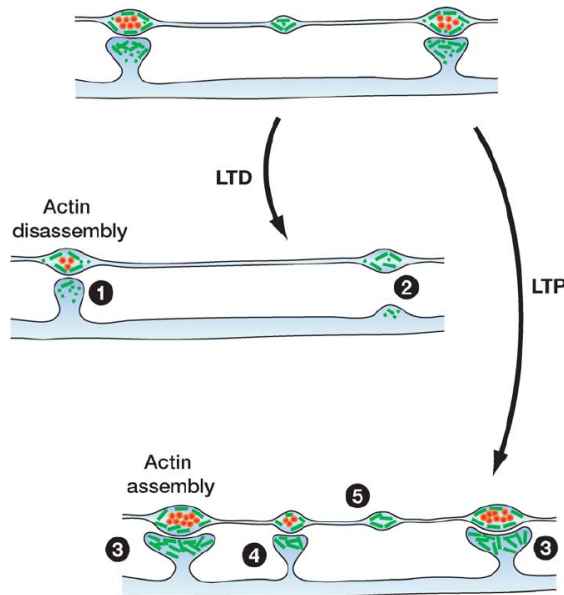


Figure 17. Actin remodeling during long term plasticity. Long term depression (LTD) is associated with spine decrease or removal connected with G-actin increase. Long term potentiation (LTP) is usually related to synapse formation or enlargement connected with F-actin increase. Adapted from Dillon and Goda, 2005

The general model mentioned above describes the terminal, structural basis of synaptic plasticity. On a molecular level, this process is still far from understood and multiple environmental and cellular factors might regulate the aforementioned processes. At the level of hippocampal excitatory synapses, glutamate released from the presynaptic density triggers activation of postsynaptic NMDA receptors, leading further to calcium influx. Ca^{2+} uptake and subsequent activation of protein kinases promote further spine morphology changes by the recruitment of novel AMPA receptors and actin remodeling (McLeod and Salinas, 2018).

Lastly, recent studies show that synaptic plasticity is also controlled by the Wnt pathway, similarly to the Wnt pathway briefly introduced during the synapse formation that involved formin Daam1 (Torres and Inestrosa, 2017). In hippocampal neurons, Wnt7a binds to the corresponding Frizzled-7 receptor that was shown to be required for AMPA receptor recruitment (Figure 18). This synaptic potentiation mechanism was shown to be dependent on activation of Calcium/calmodulin-dependent protein kinase type II (CaMKII) and Protein Kinase A (PKA) kinases, yet a full understanding of the process is still vague. Moreover, overexpression of Wnt antagonist Dickkopf-1 (Dkk1) in hippocampal neurons was connected to excitatory synapse loss, enhanced LTD, and long-term memory impairments (Figure 18). Upregulation of Dkk1 was connected to neurodegenerative diseases like Alzheimer's disease (Purro et al., 2014; Sellers et al., 2017).

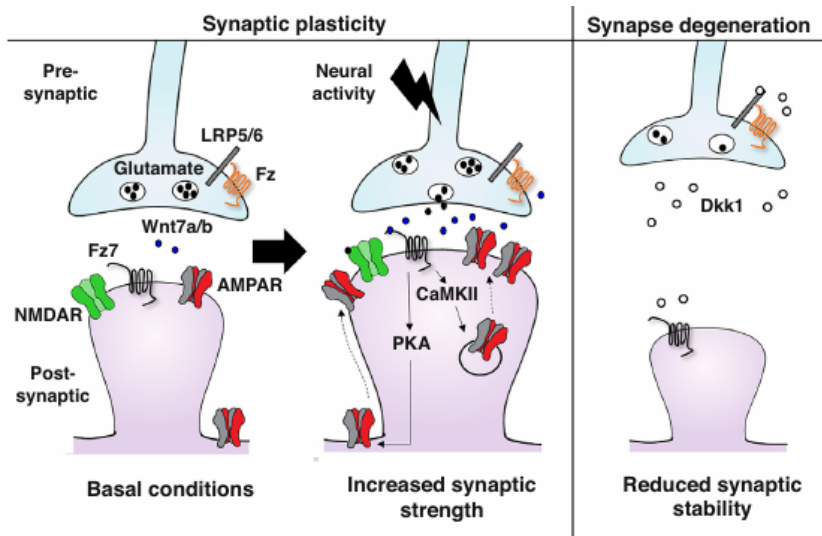


Figure 18. The Wnt pathway is involved in synaptic plasticity and integrity. Adapted from McLeod and Salinas 2018.

As described above actin and ABPs are crucial proteins for many aspects of neurogenesis together with establishment of synaptic connectivity and memory formation. In the last Chapter of this Introduction we will focus on possible regulatory mechanisms controlling neurogenesis.

8. Alternative splicing is a molecular mechanism contributing to brain complexity

Epigenetic control of specific gene expression patterns and subsequent post-transcriptional splicing of the pre-mRNA molecules are the main control mechanisms during neurogenesis. Alternative splicing (AS) affects more than 90% of human genes, greatly increasing our proteome with tightly regulated and tissue-specific patterns (Ellis et al., 2012; Zheng, 2020). Multiple studies have proven the importance of AS for neuronal development, maturation, functioning, and activity. Many alternatively splicing events have been found to be tightly neuronally-regulated with either up or downregulation in neurons (Figure 19A). Here of special interest are the neural-regulated events impacting the proteome with the strongest enrichment in cytoskeletal genes (Figure 19B)(Irimia et al., 2014).

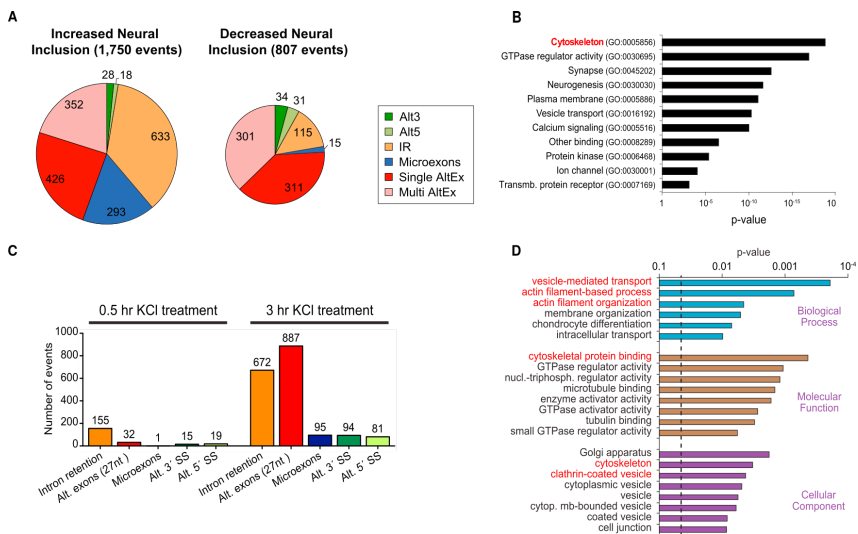


Figure 19 Neuronal-specific and activity-dependent alternative splicing events. A) Pie charts describing neuronal-specific AS. B) GO enrichment score for neural-regulated AS predicted to generate protein isoforms. C) Bar graphs describing changed AS events upon KCl treatment. D) GO enrichment score of microexons upon neuronal activation. $|\text{dPSI}| \geq 15$; Alt3/Alt.3'SS, alternative splice-site acceptor; Alt5/Alt.5'SS; alternative splice-site donor; IR, intron retention; Microexons, 3–27 nt exons; Single/Multi AltEx, single/multiple cassette exons. Adapted from Irimia et al., 2014; Quesnel-Vallières et al., 2016 .

The importance of AS in neuronal functioning, and potentially in memory and learning, becomes even more obvious if one focuses on AS turnover after neuronal depolarization. Quesnel-Vallières et al. 2016 have found many classes of alternative splicing events to be changed upon KCl treatment of cultured hippocampal neurons (Figure 19C). After extensive neuronal depolarization (3h period) majority of the events have been classified as alternative exons or intron retentions (Figure 19C). With intron retention events probably resulting in non mediated decay of their mRNA transcripts, exon skipping events resulting in proteome shift could play a role in long term memory formation. Additionally, using bioinformatic approaches, the authors found a gene ontology enrichment in cytoskeleton-related processes. Here of special interest is a recently discovered group of small exons called microexons (3-27 nt long exons)(Irimia et al., 2014). Around 30% of all discovered neural microexons (95/293) have been found to be differentially spliced upon neuronal depolarization with strong enrichment in actin filament organization, actin filament-based process, and cytoskeletal protein binding (Figure 19D).

Figure 20 describes only a few splicing factors that have been found to impact neurogenesis-related processes. Here of special interest is Srrm4 (nSR100; Serine/Arginine Repetitive Matrix 4), a neural-specific splicing factor known as the “master regulator” of the aforementioned, microexon splicing program. Despite the relatively recent discovery of Srrm4 and its role in microexon regulation, Srrm4 has been found to play a crucial role in neuronal differentiation (figure 20 A), neuronal migration during gastrulation (figure 20 B), as well as synapse formation and its functioning (figure 20 C).

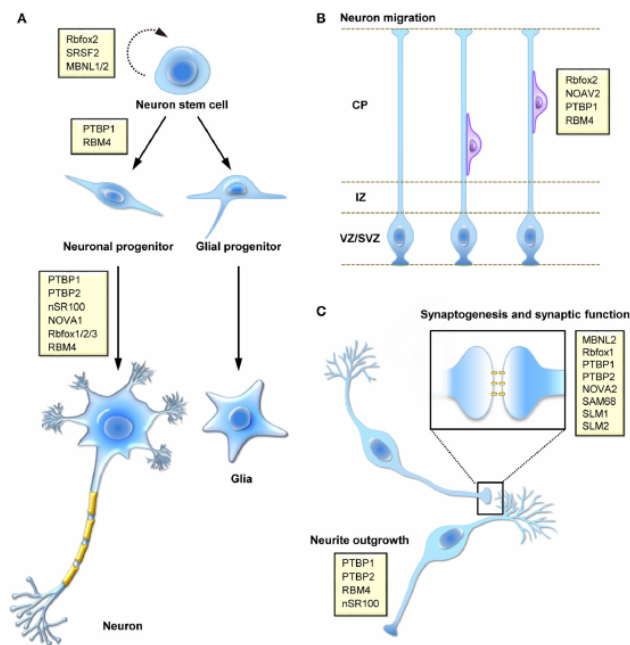


Figure 20. Splicing factors regulating mammalian neurogenesis. A) Neuronal differentiation B) Neuronal migration during gastrulation. C) Synaptogenesis and synaptic functioning. Adapted from Su et al., 2018

Initially, SRRM4 has been found to be misregulated in the brains of people with autism spectrum disorder (Irimia et al., 2014). Upon

exhaustive investigation of *Srrm4*'s function, Quesnel-Vallières et al. 2015 found that mice lacking *Srrm4* were not viable, as they died hours after birth due to respiratory failure connected with neuronal impairments. Loss of *Srrm4* impacted the proper development of the nervous system, partially by the misregulation of neuronal migration and neurite outgrowth (Quesnel-Vallières et al., 2015). Haploinsufficiency of *Srrm4*, even though viable, causes similar to human autistic-like behavior in mice in a sexually dimorphic manner. Mutant neurons had misregulated number and morphology of synaptic spines (Figure 21A) together with impaired synaptic transmission (Figure 21B) proving further the importance of microexons in neuronal functioning (Quesnel-Vallières et al., 2016).

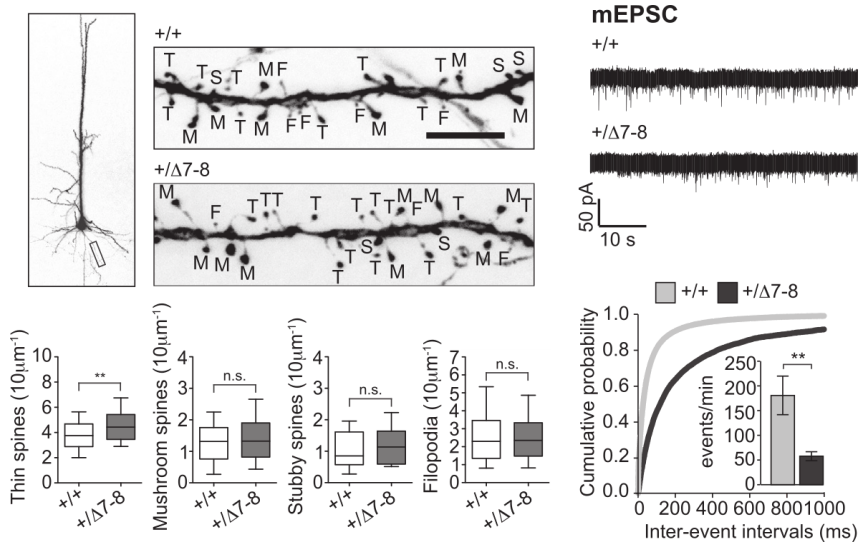


Figure 21. *Srrm4*^{+/ Δ 7-8} mice have impaired synapse morphology and function. A) Dendritic arbor analysis in EGFP⁺ pyramidal neurons from Thy1-EGFP mice. Spine types are defined as M - mushroom, T - thin, S - stubby, or F - filopodia. Thin spine number was upregulated in mutant mice (***p* = 0.006), n.s., not significant. B) miniature excitatory postsynaptic currents (mEPSC) frequency is increased in *Srrm4*^{+/ Δ 7-8} mice. Adapted from Quesnel-Vallières et al., 2016

Microexons

Except for connection to various diseases and remarkably tight neural-specific inclusion, the microexon splicing program has other exceptional features. Due to evolutionary comparison, microexons emerged circa 400–450 million years ago, and seem to be rather resilient to evolutionary-driven changes (Irimia et al., 2014). On a molecular basis, the majority of microexons seem to be frame-preserving events, mostly impacting the disordered, surface-exposed regions of proteins with close proximity to functioning protein domains (Irimia et al., 2014; Quesnel-Vallières et al., 2015; Raj and Blencowe, 2015). These molecular features suggest a role in modifying protein-protein interactions (PPIs) which might be crucial for modifying synaptic plasticity.

So far only a handful of microexons have been studied, mostly connecting their function to neuritogenesis, neurite outgrowth, and neuronal migration. Nevertheless, a detailed description of the impact of microexon inclusion on protein functioning remains elusive (Ohnishi et al., 2014, 2017; Quesnel-Vallières et al., 2015).

One of the last microexons described belongs to a Eukaryotic translation initiation factor 4G (eIF4G). Removal of this 21 nt microexon has been found to impair the expression and translation of synaptic proteins. Mice lacking the microexon displayed social behaviour defects but also learning and memory deficits (Figure 22A) further confirming microexons' role in synaptic plasticity. This

was confirmed by an impaired synaptic function of hippocampal neurons, surprisingly causing no change in short-term plasticity, but impairing long-term potentiation (Figure 22B) (Gonatopoulos-Pournatzis et al., 2020).

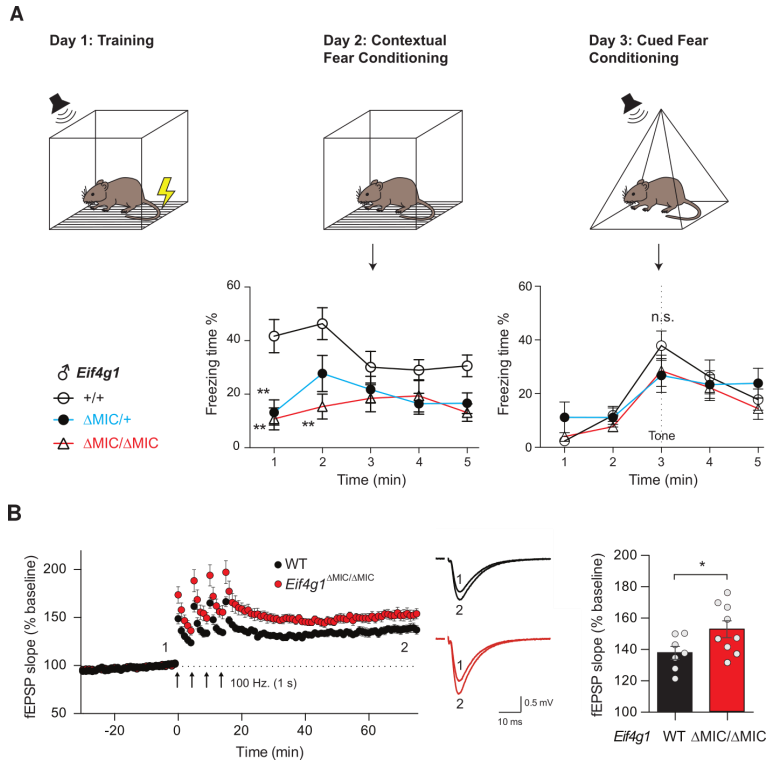


Figure 22. Microexon in eIF4G is responsible for long term memory.

A) Upper panel: Schematic representation of fear-conditioning experiment performed to test long term memory. Lower panel: quantification of the percentage of freezing time during 5 min of experiment performed 24 h (Day 2) or 48 h (Day 3) after the training session. B) Left panel: Long Term Potentiation (LTP) induction by four 100-Hz (1s), separated by 5 min each. Right panel: Averaged fEPSP between 50 and 60 min post-induction

Described here role eIF4G is just one example on how AS can potentially impact higher cognitive functions like memory and learning. This highly interesting discovery is unfortunately not focusing on the actin skeleton changes that as described in the

Introduction to this Thesis are the main molecular and structural basis responsible for memory and learning. Considering all of the aforementioned features together with microexons evolutionary conservation, tight neuronal-specific inclusion, enrichment in synaptic proteins, and inclusion change upon neuronal depolarization I would like to investigate the putative role of microexons in modification of actin cytoskeleton.

Objectives

Objectives

The main goal of the thesis was to elucidate the physiological relevance of the microexon of Daam1. For this goal, I have set the following objectives:

- 1) To perform a structural analysis of the DAAM1 protein and its change upon microexon inclusion.
- 2) To do a biochemical analysis of the impact of the microexon inclusion on the function of the FH2 domain.
- 3) To assess the functional impact of microexon removal in neuronal cells differentiated *in vitro*.
- 4) To unravel the role of microexon inclusion during nervous system development and early function.
- 5) To characterize the role of Daam1 microexon in learning and memory formation in adult mice.

Results

Results

1. Molecular analysis of DAAM1

In the first part of the project, we have used bioinformatic tools as well as proteomic approaches in order to understand the molecular role of the microexon insertion into DAAM1 transcripts. This approach had one main goal: to understand the molecular importance of the DAAM1 microexon splicing and its putative physiological relevance for the protein function. The aforementioned steps constructed a strong base for the hypothesis formation about the function of the microexon and drew an easy and logical path for investigating microexons' importance using biochemical approaches.

1.1. DAAM1 gene expression

To understand the function of a splice variant, one first has to understand the function of the protein in its canonical form. In order to do so, we started from the analysis of the gene expression pattern of the DAAM protein family in the vertebrate clade. Dishevelled-associated activators of morphogenesis (DAAM) proteins are highly evolutionarily conserved proteins with two distinct paralogs in vertebrates, *DAAM1* and *DAAM2*, which likely resulted from the whole genome duplications that occurred at the origin of vertebrates. No cell type/tissue-specific gene expression pattern has been observed for DAAM1 and DAAM2, as they are

both expressed at relatively comparable levels across most of the analyzed tissues (**Figure I.1**).

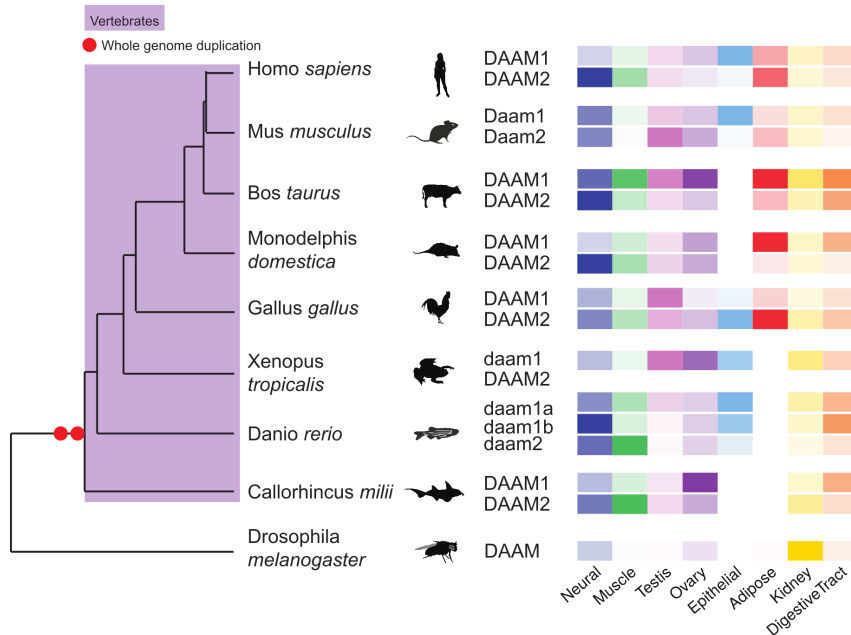


Figure I.1. Evolutionary conservation and relative gene expression pattern across tissues of the DAAM family. Gene orthologs of human DAAM1 and DAAM2 (from Ensembl) are represented for eight vertebrate species and *Drosophila melanogaster*. Relative expression levels across tissues are represented in the right panel.

Additionally, a more detailed analysis of the transcriptomic profiles of the DAAM1 gene has been made with data from VastDB (Tapial et al. 2017; <http://vastdb.crg.eu>) “An atlas of alternative splicing profiles in vertebrate cell and tissue types”. This platform allows easy and user-friendly comparison of both gene expression and alternative splicing profiles which we will consider in the next sub-chapter. **Figure I.2** shows gene expression patterns based on collected RNA-seq samples for humans.

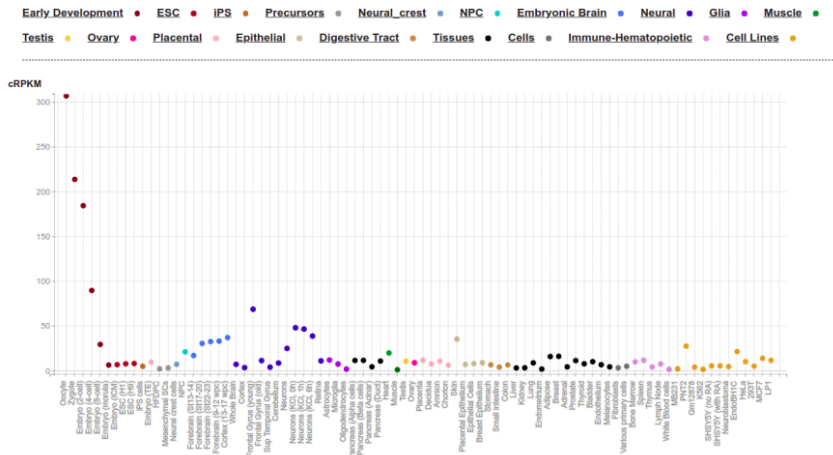


Figure 1.2. RNA-seq gene expression estimates for DAAM1 in human based on VastDB.

The DAAM1 gene has been detected in all analyzed samples, with expression in most of them below 50 cRPKM. Surprisingly, the highest gene expression has been detected in oocyte and early-stage embryos (zygote, 2, 4-cell stage embryos; 213, 184, and 89 cRPKM accordingly) probably connected with DAAM1’s role in the Planar Cell Polarity process (Nishimura et al., 2012). This expression pattern seems to be similar in other analyzed mammals (mouse, and cow) with a drastic change in chicken and zebrafish (<http://vastdb.crg.eu>), probably due to the differences in the reproductive system. This higher expression during early development is potentially interesting and might help to understand the function of the canonical variant of the protein, which we will consider in further chapters of this thesis.

1.2. DAAM1 structure and mode of action

Arguably, the next step in understanding the function of a protein-coding gene involves the analysis of the protein structure, together with the characterization of its domains. Both aspects are essential for understanding the molecular “mode of action” of a protein, and consecutively of its splice variants. DAAM1 is a typical formin incorporating 7 well defined and relatively well-described domains. Figure I.3.A shows DAAM1 protein 3D structure predicted using the highly accurate, artificial intelligence supported program AlphaFold2 (Jumper et al., 2021). Previously characterized domains have been colour-coded for visualization.

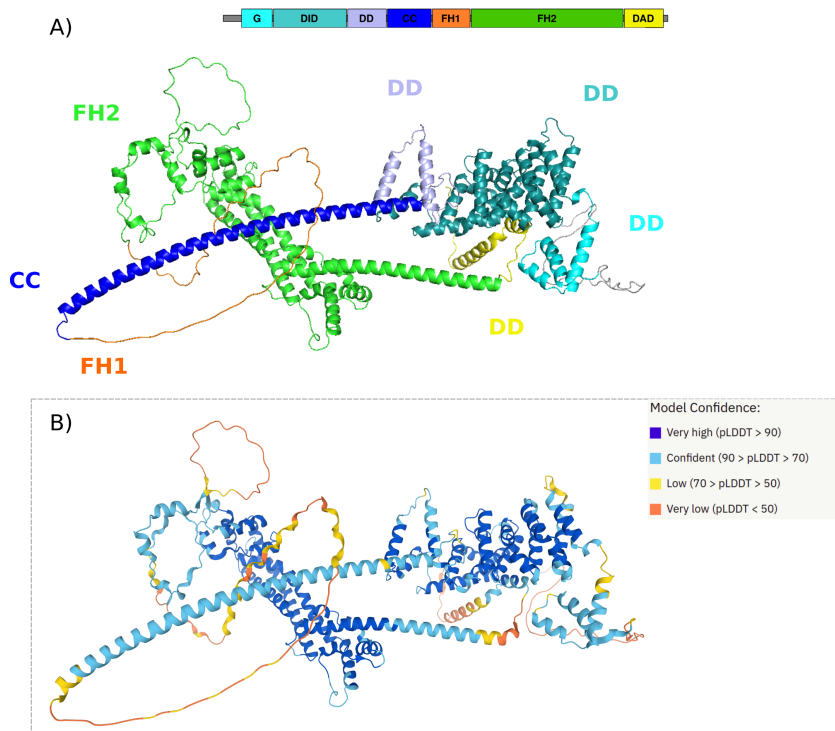


Figure I.3. DAAM1 protein structure.

A) Schematic representation (upper panel) and structure prediction (lower panel) of DAAM1 protein based on B. Representative colours describe predicted domain boundaries. B) Model confidence based on AlphaFold2 (Jumper et al., 2021). The confidence level of structure prediction where the colour coding from orange to dark blue corresponds to very low to a very high degree of confidence respectively. Symbols correspond to domains as follows: (G) GTPase-binding domain; (DID) Diaphanous-inhibitory domain; (DD) dimerization domain; (CC) coiled-coil domain; (FH1) Formin-homology-1 domain; (FH2) Formin-homology-2 domain; Diaphanous-autoregulatory domain (DAD).

As visible in the figure, DAAM1 is a highly structured protein, consisting mostly of helices and coil regions, cut through with beta-strands. Two distinct disorder regions are visible, namely the flexible FH1 domain and the loop region of the FH2 domain.

The biggest domain present (Figure I.3, green domain) is a catalytic formin homology 2 (FH2) domain, which is the characteristic domain of the Formin family. DAAM1 belongs to Diaphanous-related formins characterized by the autoinhibitory regulation described in detail in the Introduction section.

1.3. Alternative splicing of DAAM1

While some recent publications highlighted a possible function for DAAM1 in neurological disorders in humans (van der Lee et al., 2019; Mollink et al., 2019), the gene is not preferentially expressed in the neural context (see the previous paragraph). This lack of neural-restricted expression patterns suggested that other regulatory mechanisms might be employed to specifically modulate DAAM1 action at the neural level. Thus, we decided to investigate the possible impact of alternative splicing on DAAM1 function in neurons.

For every alternative splicing ‘event’ the relative use of the alternative sequence can be quantified as the proportion of transcripts that include that sequence to the total number of transcripts from that gene. This measure is called ‘Percent Spliced In’ or PSI. According to VastDB (<http://vastdb.crg.eu>), only two substantially alternatively spliced exons have been detected for DAAM1 (Figure I.4):

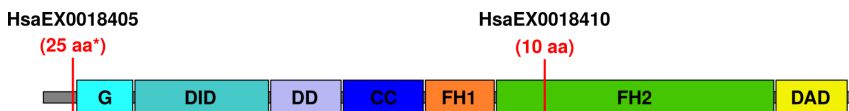


Figure I.4. Alternative splicing of DAAM1.

Schematic representation of DAAM1 protein with putative domain boundaries marked. Two exon inclusion events have been highlighted with their predicted localization on protein level. Alternative splicing events are named in correspondence to the VastDB nomenclature (HsaEX0018405 and HsaEX0018410). Predicted amino acid length (aa) has been highlighted in red

together with the putative protein localization. * asterisk marks probable protein truncation due to frameshift. Domains are described as in figure I.3.

- [HsaEX0018405](#): this event involves a 74 bp exon with no tissue specificity and potentially low inclusion (PSI oscillating around 10). This exon is inserted between the first and the second exon of the transcript resulting in a frameshift, and translation of short 146 amino acid peptide. This exon has been detected solely in the embryonic derived samples (8-cell, and morula), endothelium and white blood cells. Taking together the cellular type and the low inclusion levels one would expect a role (if any) of this exon as another level of cellular control of protein levels.

- [HsaEX0018410](#): this event involves a 30 bp microexon. Based on the transcriptomic data, this microexon is incorporated directly in the FH2 domain of DAAM1 (at the protein level), and has tightly restricted inclusion in neural tissues (average PSI in neural samples = 67.19, PSI in other tissues ~0). Figure I.5 shows VastDB based PSI profile of DAAM1 microexon inclusion in humans.

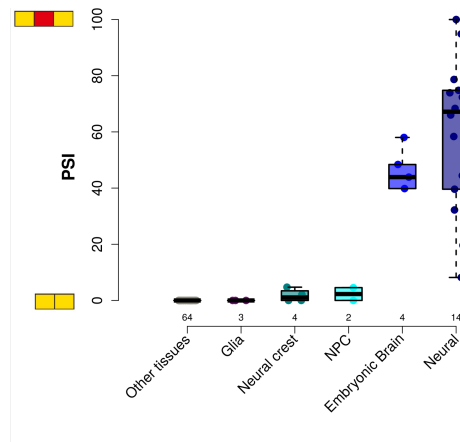


Figure I.5. neuronal-specificity of DAAM1 microexon.

Percent Spliced In (PSI) describes the percentage of mRNA transcript with microexon included based on RNA-seq. PSI values are taken from VastDB.

As discussed in the Introduction, in addition to their neuronal-specificity, microexons are characterized by their high evolutionary conservation and structural impact on disordered, protein-interacting regions (Irimia et al., 2014). We have found that the DAAM1 microexon is highly conserved from the elephant shark (*Callorhynchus milii*) to humans with a length varying from 27 to 30 nucleotides. Figure I.6 describes evolutionary conservation at the amino acid level.

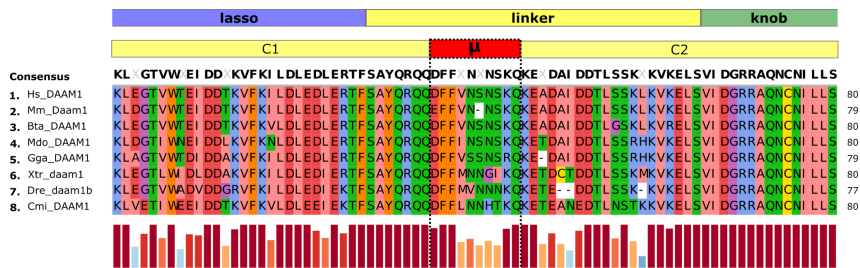


Figure I.6. Evolutionary conservation of the amino acid sequence of DAAM1 microexon.

Microexon (μ), upstream (C1) and downstream exons (C2) are highlighted together with subdomain boundaries. Consensus sequence conservation is described in the bottom panel in the form of bars. **Hsa**: Homo sapiens (human), **Mmu**: Mus musculus (mouse), **Bta**: Bos taurus (cow), **Mdo**: Monodelphis domestica (opossum), **Gga**: Gallus gallus (chicken), **Xtr**: Xenopus tropicalis (clawed frog), **Dre**: Danio rerio (zebrafish) **Cmi**: Callorhinchus milii (elephant shark).

We have used RT-PCR in order to confirm the neural-specificity of the microexon in mouse and zebrafish, predicted with *vast-tools* (<https://github.com/vastgroup/vast-tools>). In both cases, we have been able to validate the neural-specific inclusion of the microexon, which showed nearly complete inclusion in multiple brain regions as opposed to all other tissues. This result is in line with our predictions and reassures us of the microexons' neuronal-specific nature.

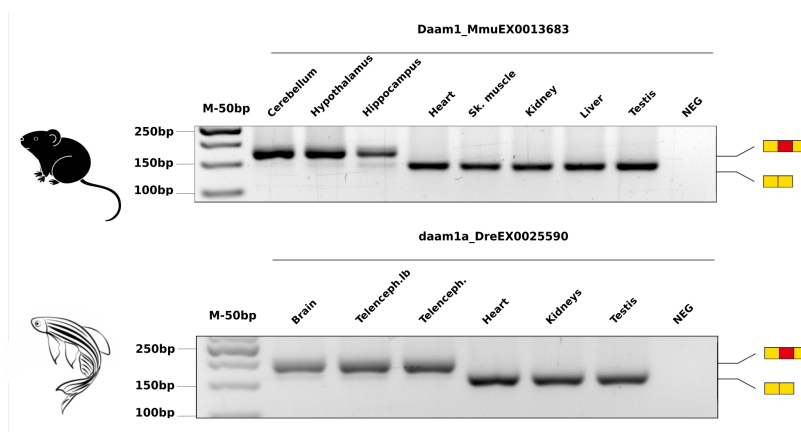


Figure I.7. RT-PCR validation of DAAM1 microexon neural-specificity. Microexon inclusion was analyzed in different tissues from mice (Mmu) and zebrafish (Dre). Inclusion and the skipping bands are indicated on the right side of the gel. Detection was performed with primers in adjacent exons and run on 2.5% agarose in the SB buffer.

Additionally, the microexon of DAAM1 is inserted directly in the disordered linker region of the FH2 domain, probably not impacting the general structure (described in Chapter 1). This feature will be further studied in the next subchapter, as understanding the structural impact of the microexon insertion will be the key to elucidating its physiological importance.

1.4. Structural impact of microexon insertion in DAAM1

DAAM1 microexon is directly inserted into the linker region of the FH2 domain, responsible for both domain flexibility and processive polymerization of actin (Figure I.8)(Otomo et al., 2005).

We have modelled the core structure of both spliced variants of the DAAM1 FH2 domain (i.e. the inclusion isoform and the skipping isoform) using a human DAAM1 FH2 dimer as a template (PDB [2Z6E](#), Yamashita et al., 2007). The ten residues encoded by the microexon (red, DFFVNSNSKQ) are inserted into the disordered linker region. This insertion allows the increase of the loop length from 26 amino acids (as in non-neural tissues) to 36, possibly impacting domain function.

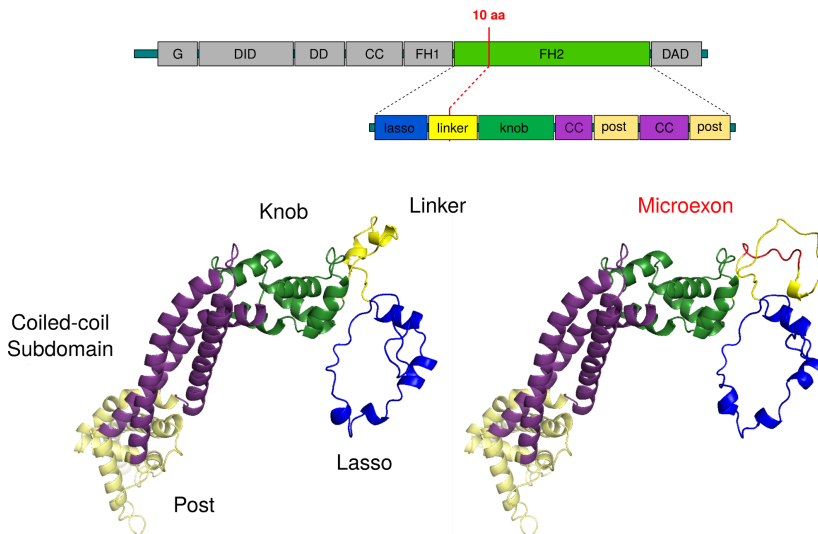


Figure I.8. Structural impact of DAAM1 microexon insertion.

The upper panel shows the schematic representation of DAAM1 protein

together with the subdomain division of the FH2 domain. Domains are labelled as in figure I.3. The lower panel describes the structure of the FH2 domain without microexon (left), and with microexon insertion (right). Subregions of the lasso, linker, coiled-coil as well as knob and post regions share the same color-code in the upper and lower panels.

Interestingly, multiple biochemical assays have shown that the FH2 domain of DAAM1 has very weak polymerization activity compared to other mammalian formins (Lu et al., 2007). Among the hypotheses to explain this low activity, two plausible reasons have been suggested. Yamashita et al., 2007, hypothesized that the linker region length is responsible for low domain processivity, which was partially confirmed by random shortening of the linker region. A different yet complementary hypothesis was formed by Lu et al., 2007. Here the authors suggested that the intramolecular interactions of the linker region plays an important role in that process. Direct mutations of the β -strand also confirmed the hypothesis, proving further a multi-layered functionality of the linker region. Unfortunately, the presence of neuronal-specific microexon microexon was an oversight in previous investigations, and its role remains elusive.

To further understand the described before low activity of DAAM1 and microexon's role in that process, we have decided to compare the loop region of all 15 formin proteins. In fact, the linker region is poorly conserved and the additional insertion of 10 amino acids makes the DAAM1 linker longest among all of the formins. This suggests that the microexon insertion may further impact its polymerization activity

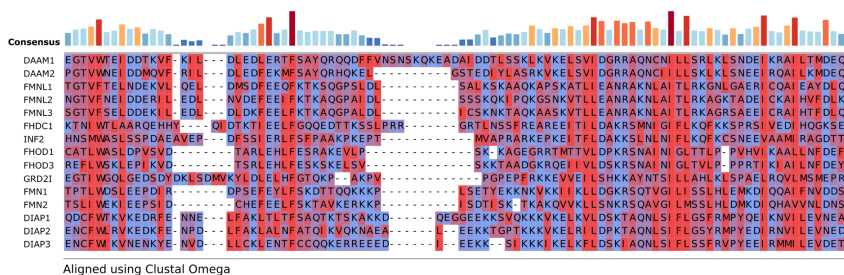


Figure I.9. Amino acid conservation of the linker region from human formin proteins. Consensus sequence conservation is described in the upper panel in the form of bars. Sequence alignment was performed using Clustal Omega.

1.5. DAAM1 microexon misregulation in human neurological disorders

Additionally, inspired by neuronal specific character of the microexon we analyze the possible role of DAAM1 microexon in human neurological disorders using publically available RNA-seq data. Interestingly, in 2 independent studies and in 2 different brain regions we found that people with bipolar disorder have slightly lower mRNA inclusion of the microexon in DAAM1 compared to the control group. Figure I.10. presents microexon percent spliced in (PSI) values in the dorsolateral prefrontal cortex in both males and females. We observe microexon inclusion for both sexes, yet the difference did not reach significant levels (Figure I.10. $p = 0.136$, ANOVA; GSE53239). We found a similar pattern in the dorsal striatum of people with bipolar disorder (Average PSI in Control = 16.01, and Bipolar disorder = 13.6; GSE80336). Unfortunately, due to low sequencing depth and low reads coverage of the splice

junctions, additional analysis needs to be performed to validate this finding.

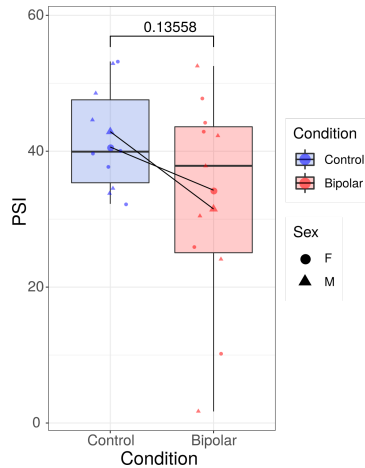


Figure I.10. DAAM1 microexon splicing in humans with bipolar disorder.
Analyzed from publicly available data: GSE53239.

The summary of the results collected in this chapter suggests a strong putative role of the DAAM1's microexon in modulating the FH2 domain mode of function. Interestingly this functional adaptation happens inclusively in neurons, arguably one of the most important cell types necessary for higher cognitive functions. In order to further understand the role of DAAM1's microexon, the next chapters of this thesis will focus on consecutive dissection of microexon's molecular role on FH2 domain functioning (Chapter 2), its importance in neuronal differentiation and function *in vitro* (Chapter 3), as well as microexons role in early development (Chapter 4), and plausible neurological alterations it might cause in adulthood (Chapter 5).

2. DAAM1 microexon impacts the biochemical function of the FH2 domain

The first chapter of this thesis presented a structurally driven hypothesis of how the DAAM1 microexon may impact FH2 domain-actin interactions. In this chapter, we test this hypothesis using tailored biochemical assays and state of the art microscopy approaches. The role of this chapter is to begin assessing the functionality of the microexon and its impact on DAAM1 protein function, mainly in the actin nucleation and polymerization processes. Yamashita et al., 2007, used an *in vitro* system called “actin polymerization assay” to assess the importance of the length of the DAAM1 linker for FH2 domain’s function. The authors of this article did not evaluate the effect of the FH2 linker modifications produced by alternative splicing, which might expand our understanding of the function of this protein. Here, I utilized a similar approach, yet instead of using random linker truncation I used physiologically occurring processes of loop modification. Additionally together with Davide Normanno (Surrey Lab, CRG) we expanded our knowledge on microexons' mode of function using state of the art microscopy techniques.

2.1. Actin polymerization assay

a) Protein purification

In order to perform biochemical assays, I first focused on purifying the proteins of interest. Here, I decided to purify the C-terminal part of human DAAM1 encompassing the FH2 domain (FH2-COOH) in two splice variants (with and without microexon). I focused on the C-terminal part of the DAAM1 protein in order to minimize the size of the protein product, as well as to assure domain functionality. Purified protein fragments would not contain the inhibitory domain (DID), nor the FH1 domain, which in the cellular environment facilitates actin polymerization by its interaction with the actin-binding protein profilin. In the *in vitro* environment, an abundance of the G-actin monomers and the lack of competition between the variety of Actin Binding Proteins (ABPs) allows us to omit the cellular functionality of the FH1 domain and accurately describe the function of the FH2 domain in isolation. A similar approach was already applied while studying the function of mouse Daam1 variant (amino acids 596–1078), proving *in-vitro* functionality of the FH2-COOH region, further supporting our functional hypothesis (Lu et al., 2007). Figure II.1.A describes a schematic representation of the designed construct and its domains. Figure II.1.B describes a schematic representation of the monomeric structure of designed FH2-COOH fragments in two splice variants.

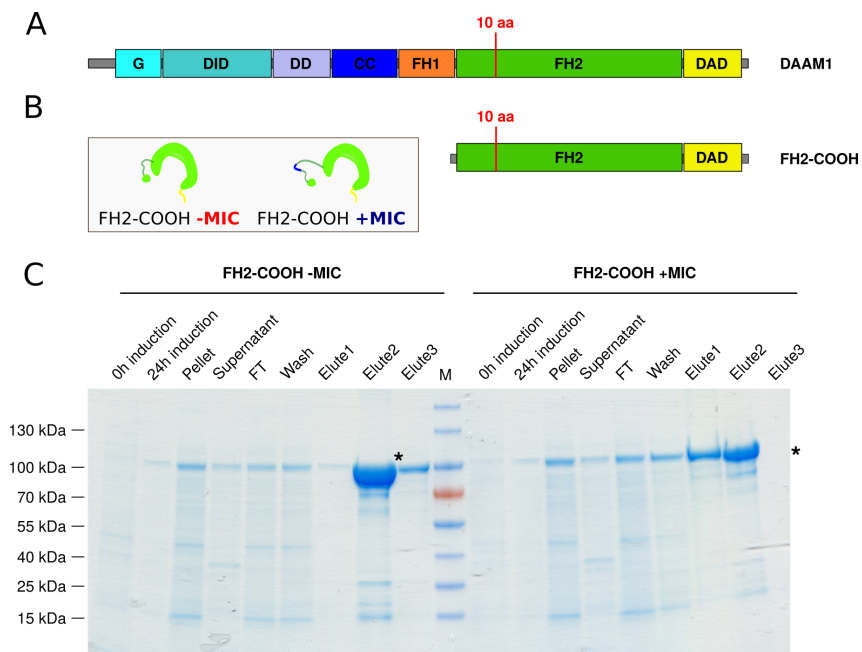


Figure II.1. Bacterial purification of the FH2-COOH fragments of DAAM1. A) Schematic representation of the domain structure of DAAM1 protein. Domains are described as in figure I.3. FH2-COOH fragment represents the protein fragment purified. B) Schematic representation of the FH2-COOH fragments purified in two splice variants (with (+MIC) and without (-MIC) microexon), in monomeric conformation. C) Coomassie-stained SDS-PAGE gel of fractions from bacterial purification. +MIC - microexon containing FH2-COOH DAAM1 fragment, -MIC - DAAM1 FH2-COOH fragment without microexon. M - marker, FT - flow through, * asterisk describes the expected protein size.

I subcloned the corresponding cDNA fragments into the protein expression plasmids kindly received from the Maurer Lab (CRG) by the courtesy of Sebastian Baumann and Maria Lluïsa Gili Sebastián. After construct validation, I purified the DAAM1's FH2-COOH fragments, with and without the alternatively spliced microexon (hereafter called -MIC and +MIC, respectively). The purification steps were performed as advised by Moseley et al., 2006, with small modifications (Materials and Methods section).

Figure II.1.C shows a summary result of the protein purification after expression in bacteria, protein solubility analysis, and subsequent affinity-based purification. An increase in the expression of the proteins of interest is visible upon Isopropyl β -d-1-thiogalactopyranoside (IPTG) treatment, with protein products migrating similarly to the 100kD marker band. This is visible while comparing the samples collected before (time point 0h induction) and after IPTG induction (time point 24h induction). Protein size is in line with our prediction, as the molecular weight of the designed proteins of interest should range between 91.966kDa and 90.79kDa (+MIC, and -MIC, respectively). At this stage, the purified FH2-COOH fragments contain an additional N-terminal Immunoglobulin G (IgG) tag that increases solubility, and a C-terminal human O6-alkylguanine-DNA-alkyltransferase (hAGT) tag, that facilitates protein folding and allows its fluorescence labelling. Next, I performed a protein solubility analysis based on strong sample centrifugation (24.000 rpm for 30 min at 4°C), and assessment of protein presence in soluble and insoluble fractions. Despite the fact that the majority of the protein (both constructs) finishes in the inclusion bodies (Pellet, Figure II.1.C), a substantial amount of the proteins of interest is present in the soluble fraction. The soluble protein fraction was subsequently submitted for the streptavidin dependent affinity purification, which provided a sufficient amount of protein for biochemical analysis for both constructs. Streptavidin-Biotin affinity-based purification was performed (StrepTrap_HP_1ml) in order to clean and isolate the proteins of interest. Figure II.1.C describes collected fractions

where the flow-through (FT) is a column unbound fraction, “Wash” is a fraction not specifically bound to the column and the “Elute” fractions (Elute1-3) describe purified protein of interest. The protein of interest was eluted and isolated from the column by application of biotin homolog (5mM [d-Desthiobiotin](#)). Elution fractions contain relatively clean protein products with sizes slightly below 100kDa, which correspond to previously described molecular weights. Lastly, a second step of protein purification was performed in which the tags cleavage and chromatography purification were performed.

Fast protein liquid chromatography (FPLC) is a widely used technique that allows protein purification, the assessment of its folding, and its size evaluation in native conditions. Figure II.2.A describes an example chromatogram, where the migration pattern of one of the FH2-COOH constructs after the tag cleavage can be seen. The chromatogram based migration pattern confirms that the protein does not form aggregates in the native conditions. Additionally, both purified splice variants migrated in their monomeric as well as homodimeric structures essential for their mode of action.

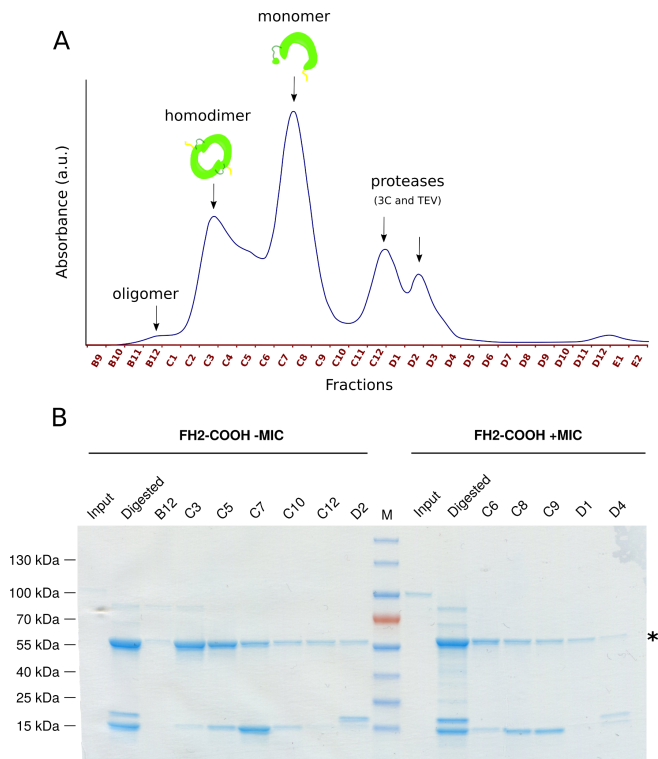


Figure II.2. DAAM1 FH2-COOH fragment purification using FPLC.

A) FPLC elution profile for DAAM1 FH2-COOH fragment purified from bacteria. FPLC run was performed using Superose12 (10/30).

B) Coomassie-stained SDS-PAGE gel of fractions through FH2-COOH fragments purification using FPLC. * asterisk describes the expected protein size.

SDS-PAGE (Figure II.2B) describes the fractions collected during the FPLC purification stages, the undigested “Input” samples (Purification step 1), as well as “Digested” FPLC subjected fractions (IgG and hAGT cleaved). Consecutive fractions show chromatography based samples corresponding to chromatogram fractions collected (Figure II.2A for -MIC). Due to SDS-PAGE based purity of fractions, samples C3 and C6 (+MIC and -MIC accordingly) were used for further experiments.

b) Turbidity assay setup

After successful purification of two alternatively spliced fragments of DAAM1, I have moved to the activity and functionality assessment. As described before actin polymerization assay is an experiment that allows to analyze actin dynamics, and was previously used to investigate DAAM1's FH2 domain impact on this process. Despite the wide usage of the assay, many obstacles have to be resolved. The protein quality, purity as well as percentage of Pyrene-labelled Actin might impact the experimental conclusion. In this assay the protein of interest is usually mixed with Pyrene-labelled G-actin monomers. Actin nucleation and polymerization occur in Mg^{2+} and ATP rich buffer, while a formation of F-actin filaments generates a higher fluorescent signal easily recorded by UV-Vis spectrophotometer. Problematically, Mg^{2+} -bound actin nucleates and polymerizes spontaneously *in vitro*, which makes ABPs functionality assessment difficult (Moseley et al., 2006). In order to adjust experimental conditions we have decided to analyze self polymerization capabilities of our actin by performing its titration. Figure II.3. describes the actin polymerization experiment where solely G-actin self nucleation and polymerization abilities were assessed in a range of conditions. Actin polymerization was observed while using the concentration of G-actin monomers between 0.5 to 2 μ M. Actin polymerization rate was calculated automatically using the R script written by Federica Mantica, a PhD student in our laboratory. The script was written

based on Doolittle et al., 2013, and applied for all of the Pyrene-based actin polymerization assays quantifications for consistency. Clear stages previously described as actin nucleation, polymerization and steady-state have been observed. By comparing our results with the literature (Moseley et al., 2006; Yamashita et al., 2007), we selected $0.5\mu\text{M}$ and $1\mu\text{M}$ actin as optimal concentration in the next experiments.

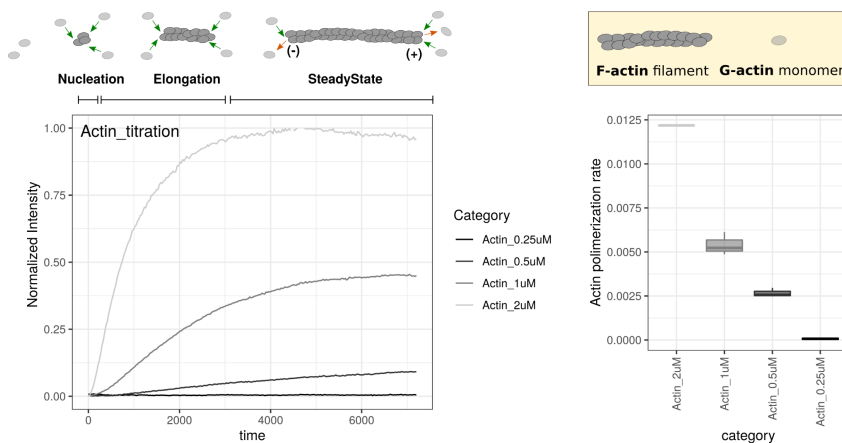


Figure II.3. Concentration-dependent actin self-assembly. The left panel represents actin self-assembly measured by incubation of the pyrene-labelled actin in various concentrations. Schematic representation of Nucleation, elongation, and steady-state phase of actin filament assembly based on $1\mu\text{M}$ Actin. The right panel represents the actin polymerization rate calculated based on Doolittle et al. 2013

Next, we proceeded to assess the functionality of the purified proteins. Here two different FH2-COOH titrations have been performed with either $0.5\mu\text{M}$ or $1\mu\text{M}$ G-actin as a substrate (Figure II.4. A and B accordingly).

Figure II.4.A describes the result of actin polymerization assay with 0.5 μ M actin and FH2-COOH titration including both splice variants. Due to calculations of actin polymerization rate, all of the conditions applied suggest **higher activity of the -MIC protein variant**. The polymerization rate difference between splice variants varies depending on the proteins concentrations applied. Unfortunately, the experimental setup seems to be in the lower threshold limit of our equipment as most of the starting intensity values are unreliable, showing extreme variability in the majority of conditions.

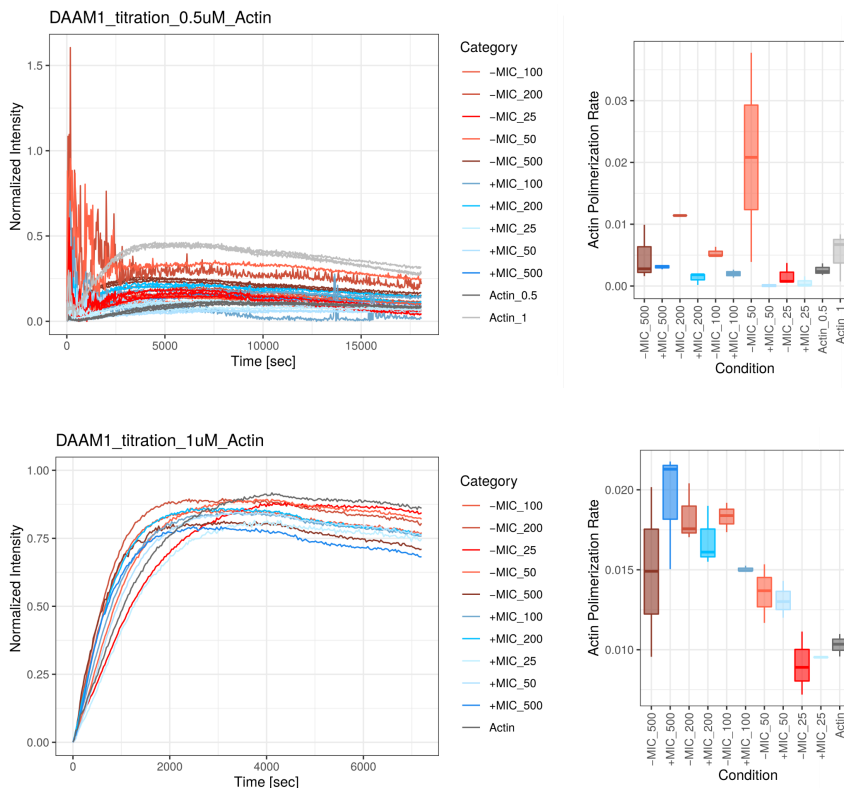


Figure II.4. Actin assembly activities of two splice variants of DAAM1

FH2-COOH fragments. Actin assembly was measured by incubation of the pyrene-labelled actin in the presence of various concentrations of DAAM1 FH2-COOH. Right panels represent actin polymerization rate calculated based on Doolittle et al. 2013 A) Actin assembly using 0.5 μ M actin using various Concentrations of human FH2-COOH fragment of human DAAM1. B) Actin assembly using 0.5 μ M actin using various concentrations of the FH2-COOH fragment of human DAAM1.

Considering the low reliability of the previous results (the probable result of the low actin concentrations), we have decided to repeat the titration experiment using a higher, 1 μ M actin concentration (Figure II.4.B). This titration experiment was more reliable, showing more stable intensity recordings and further supporting our previous observations. Consistently, microexon lacking FH2-COOH fragment (-MIC) has higher actin polymerization rate capabilities with the highest difference in conditions between 100-200nM. By correlation of our results together with literature, we have decided to use 200nM protein to reproduce literature conditions as faithfully as possible.

Finally, I have performed the actin polymerization assay 6 times using two separate protein purifications (using 200nM FH2-COOH fragments and 1 μ M G-actin) to make the most reliable conclusions and test the reproducibility of the construct based activity difference. Figure II.5.A shows an example experiment performed where 5 technical replicates are visible. Based on summary data from 6 experiments performed, Figure II.5.B shows the summary of the actin polymerization rate quantified per condition. FH2-COOH protein with microexon removed (-MIC variant) shows a significantly higher actin polymerization rate. This is partially

consistent with previously published data where random linker shortening (in some cases) increased the domain activity (Yamashita et al., 2007). Figure II.5.C describes normalized intensity increase throughout the experiment course. Here, 5 technical replicates from Figure II.5.A are averaged for clarity. Based on actin self polymerization, clear nucleation, elongation and steady-state can be described as indicated before. The addition of either of the FH2-COOH variants impacts the actin dynamics, spreading its course. Here, particularly **-MIC shows** more striking differences described by nearly non-detectable nucleation lag phase, **a more rapid elongation phase and higher fluorescence reached during the steady-state**. Altogether these results show the higher activity of -MIC variant probably coming from stronger binding and/or affinity to actin. Figure II.5.D describes one possible model of the mode of action of FH2-COOH fragments where during the steady-state, net polymerization rate for the -MIC variant is higher (+2) in comparison to +MIC variant (+1).

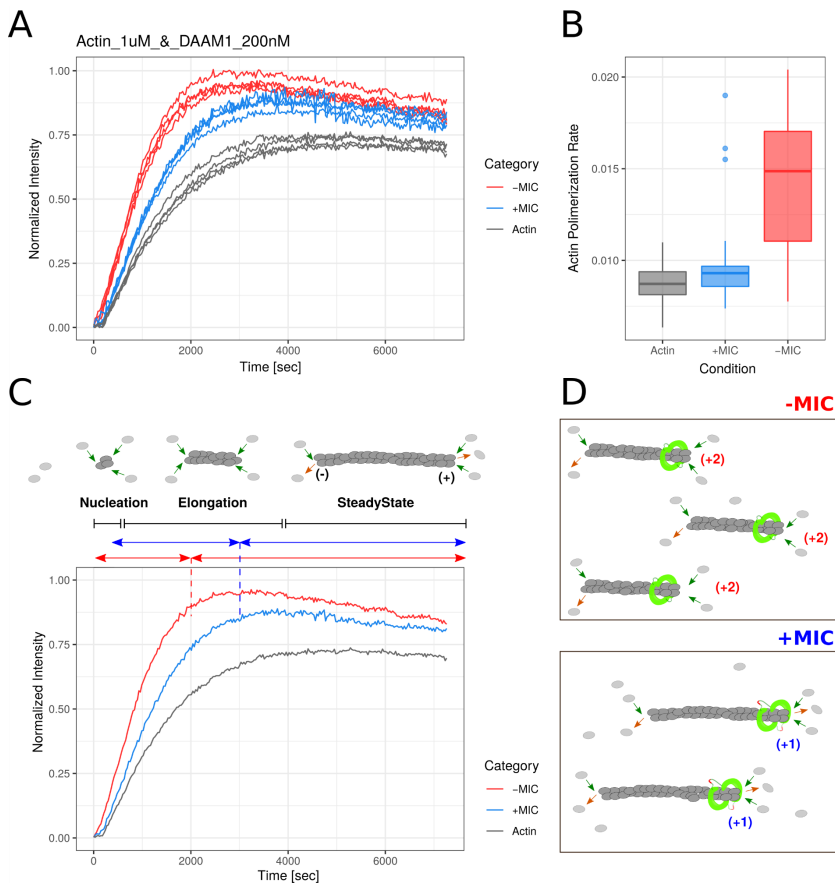


Figure II.5. Actin assembly differences between two splice variants of DAAM1 FH2-COOH fragments. Actin assembly was performed using $1\mu\text{M}$ actin, and 200nM FH2-COOH fragments. A) Example of an experiment performed. B) Actin polymerization rates summary of six independent experiments. Actin polymerization rates were calculated as slopes of curves at 50% assembly and shown as means \pm SD based on Doolittle et al. 2013. C) Splice variants of DAAM1 FH2-COOH fragment impact actin dynamics. Polymerization curves are an average of A) with a schematic representation of nucleation, elongation, and steady-state phase of actin filament assembly. D) Schematic representation of the actin dynamics at the steady-state. (+1) and (+2) represent plausible net values of actin dynamics depending on the splice variant.

2.2. TIRF microscopy of actin polymerization

The actin polymerization assay described above is a powerful technique yet due to the readout simplicity the resulting conclusions have their limits. To further assess the role of DAAM1 microexon in the actin dynamics, I decided to perform TIRF microscopy. As described in the Introduction (Chapter 4. actin-binding proteins; Figure 7C), TIRF is a microscopy technique that has been previously used to investigate subtle differences between actin nucleating factors. This technique not only allows visualization of the quaternary structures of actin filaments but also to understand the impact of ABPs on actin dynamics. To my knowledge, so far only two studies analyzed DAAM1-derived FH2 domain activity using TIRF microscopy. The first study focused on DAAM1 based microtubule/actin interaction (Szikora et al., 2017), while the second one on DAAM1's involvement in actin filament bundling (Jaiswal et al., 2013). None of these studies considered DAAM1's splice variants and their putative role in modulating actin dynamics and structure. All of the TIRF microscopy experiments have been performed together with the TIRF microscopy expert Davide Normanno (CRG, Surrey Lab), while data analysis was performed together with Raúl Gómez Riera (Advanced Light Microscopy Unit, CRG).

Figure II.6. describes the first TIRF imaging results of actin polymerization using protein and actin concentrations similar to previous reports (200nM FH2-COOH, and 1.8 μ M G-actin

monomers). Short F-actin filaments are visible immediately after the start of the experiment for both splice variants (Figure II.6.A). After 15 min from the start of the experiment, a steady state was reached and no further changes were visible even after extending the duration of the experiment. In these conditions clear differences in the mode of action between +MIC and -MIC are visible (Figure II.6.A, 15 min). Figure II.6.B shows (coloured arrows) the evolution in time of individual actin filaments at higher magnification. Due to the limits of manual quantification, which implies that only limited areas can be analyzed, we randomly selected five regions from each reaction chamber. Significant differences between +MIC and -MIC conditions have been observed when analyzing the total intensity of a region of interest (ROI; $p=0.015$ student's t-test), the filament number ($p=0.008$ student's t-test), as well as the filament length ($p=3.14e-28$ student's t-test). This result suggests a possible difference in the actin network structure upon splice variant exposure. Unfortunately, in these conditions the reaction speed is fast and the steady-state occurs rapidly, making it difficult to investigate the actin dynamics in detail. This is probably due to technical limitations, including the stationary nature of the reaction (no mixing during the reaction), relatively small reaction volume and the usage of glucose and methylcellulose in the reaction mixture. These compounds are standard chemicals necessary for filament sedimentation, which is crucial for imaging in TIRF microscopy. Regardless, the application of these chemicals changes the viscosity of the microenvironment of the reaction.

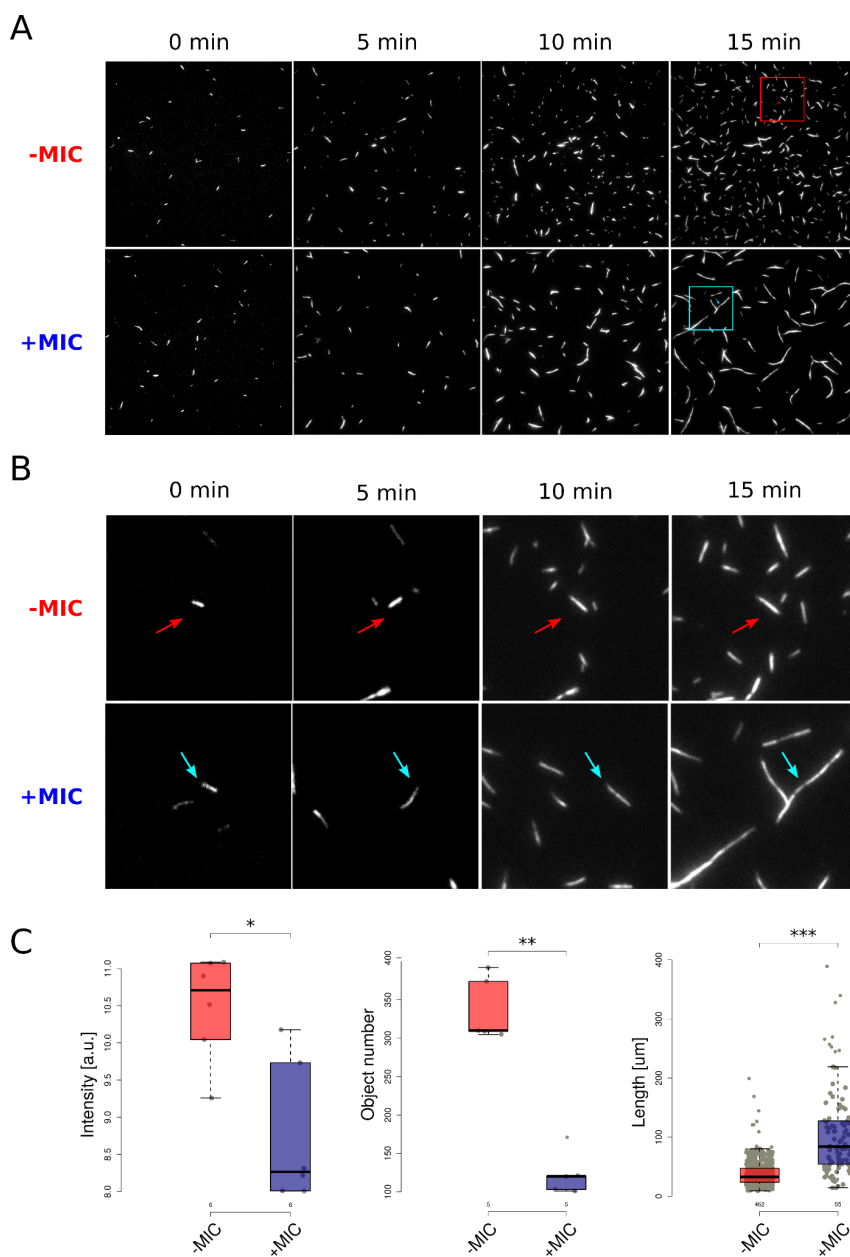


Figure II.6. Actin polymerization experiment using TIRF microscopy.

A) Time series of fluorescence micrographs showing the F-actin filaments stained with SiR-Actin in presence of microexon containing (+MIC) or

non-containing (-MIC) splice variant of the FH2-COOH fragment of human DAAM1. B) Magnification of F-actin fibres from A) highlighted as a square. Arrow indicates the same actin fibre between the timepoints. C) Summary quantification of F-actin fibre features (from left to right: intensity, number of objects, length of the actin structures) after 15 min of reaction from 5 different regions of interest selected randomly. Significance codes: * $p \leq 0.05$, ** $p \leq 0.01$, *** $p \leq 0.001$.

Considering these limitations, we then aimed at optimizing the experimental conditions for the TIRF microscopy investigation of actin dynamics (similarly at what we did for the actin polymerization assay). Variable actin concentrations were used spanning from $1.8\mu\text{M}$ to $0.05\mu\text{M}$. Based on these experiments we have concluded that the best condition to analyze actin dynamics using TIRF microscopy is using $0.2\mu\text{M}$ actin concentration and these conditions will be used in the next experiments.

After adjusting the conditions we have decided to perform detailed actin dynamics and morphology analysis. Experiments were performed for two hours and example time points are presented in Figure Figure II.7.A. Figure II.7.B shows higher magnification of an individual actin filament evolution in time. Together with Raúl Gómez Riera, we have analyzed the temporal evolution of the actin network morphology. Previously published plugin AnalyzeSkeleton was used in order to segment and skeletonize the actin filaments for further analysis. (<http://fiji.sc/AnalyzeSkeleton>; Arganda-Carreras et al., 2010; Polder et al. 2010). Figure II.7.B contains the comparison between acquired and skeletonized actin filaments at

the 90th minute of the experiment. Further analysis was performed allowing the comparison of the length, intensity, and branching of actin filaments in real-time and subsequent comparison between conditions (Figure II.7.C). The **-MIC variant impairs actin filament length** (length of actin fibres during steady-state averaged for -MIC \approx 40pixel, +MIC \approx 70pixel, and Actin \approx 75 pixel), further supporting our previous result. This is probably due to the higher affinity to actin fibres and lower dissociation rate as hypothesized before (high K_{on} and low K_{off} rate). We then decided to analyze some additional features based on the observations made by Jaiswal et al., 2013 concerning DAAM1's involvement in actin filament bundling. We have observed that the **-MIC variant** at longer times **allows higher actin filament bundling** based on filament intensity (Average intensity of fibres during steady-state reached: -MIC \approx 165a.u. , +MIC \approx 150a.u., and Actin \approx 135a.u.). Surprisingly, **neural-specific +MIC variant allows faster actin bundling** in our conditions and additionally allows the more efficient formation of tertiary structures. Next, we analyzed the actin filament branching parameter (Branches number during steady-state reached: -MIC \approx 1.25, +MIC \approx 2, and Actin \approx 1.5). The higher actin filament bundling by the -MIC variant could explain the higher "actin polymerization rate" quantified during the actin-pyrene assay. Based on TIRF microscopy results we can conclude that that's not the case and that the difference between the splice variants is more complex than we previously thought.

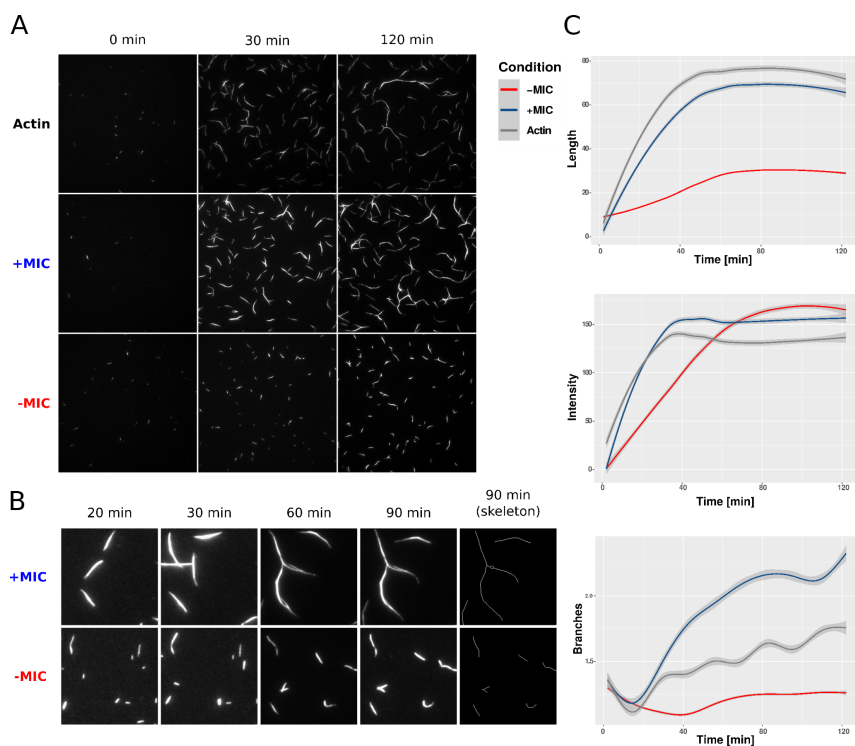


Figure II.7. Actin dynamics and morphology change upon microexon removal. A) Time series of fluorescence micrographs showing the F-actin filaments stained with SiR-Actin in presence of microexon containing (+MIC) or non-containing (-MIC) splice variant of the FH2-COOH fragment of human DAAM1. B) Magnification of F-actin fibres from A), together with the skeletonized fibres (90 min skeleton) using Fiji plugin AnalyzeSkeleton (Arganda-Carreras et al., 2010; Polder et al. 2010). C) Quantification of actin fibres Intensity, Length and Branching throughout the course of the experiment.

The hypothesis of higher affinity of DAAM1 to actin fibres upon microexon removal pushed us further in order to investigate not only the actin dynamics but also protein dynamics on actin fibres by using fluorescently labelled FH2-COOH fragments.

2.3. Dual TIRF microscopy with SNAP labelling

In order to analyze the actin and FH2 domain dynamics at the same time, together with Davide Normanno, decided to perform dual TIRF microscopy experiments. To do so, our two splice variants were subcloned and now conjugated with a SNAP-tag® that can be fluorescently labelled. Unlabelled fluorescently SNAP-FH2-COOH proteins with and without microexon (+MIC-SNAP and -MIC-SNAP accordingly) were purified by our in-house Protein Technologies Unit following the protocol described previously. Figure II.8.A describes a gel filtration derived chromatogram where spectra for both purified proteins have been overlapped. No significant size difference has been observed between purified variants implying similar folding capabilities. Additionally, for both protein variants, similar migration patterns have been observed with two major elution peaks corresponding to dimeric and monomeric fractions, as described before. This homodimerization further supports the proper folding and interaction of purified protein fragments essential for the actin and FH2 domain dynamics analysis.

Purified SNAP-FH2-COOH fragments were subsequently labelled with a fluorescent dye (SNAP-Surface® Alexa Fluor® 488) showing similar labelling efficiency (around 80% protein labelled for both variants). Figure II.8.B depicts a schematic representation of the fluorescence labelling of SNAP-FH2-COOH homodimer performed. Figure II.8.C is a summary figure, representing all of the

proteins purified and used during the course of the biochemical experiments reported here. As visible in the right panel, only fluorescently labelled fractions of SNAP-FH2-COOH protein variants show a fluorescence signal (+SNAP for fluorescently labelled fractions). Subsequently, I have performed an actin polymerization assay, as before using newly purified proteins for comparison (Figure II.8.D). Actin polymerization rate calculated was significantly impaired in all new constructs purified (before and after fluorescent labelling), showing on average a lower rate than actin control. This can probably be due to improper protein functioning or simply due to technical incompatibility of the novel constructs with spectroscopy-based character of the actin-pyrene assay.

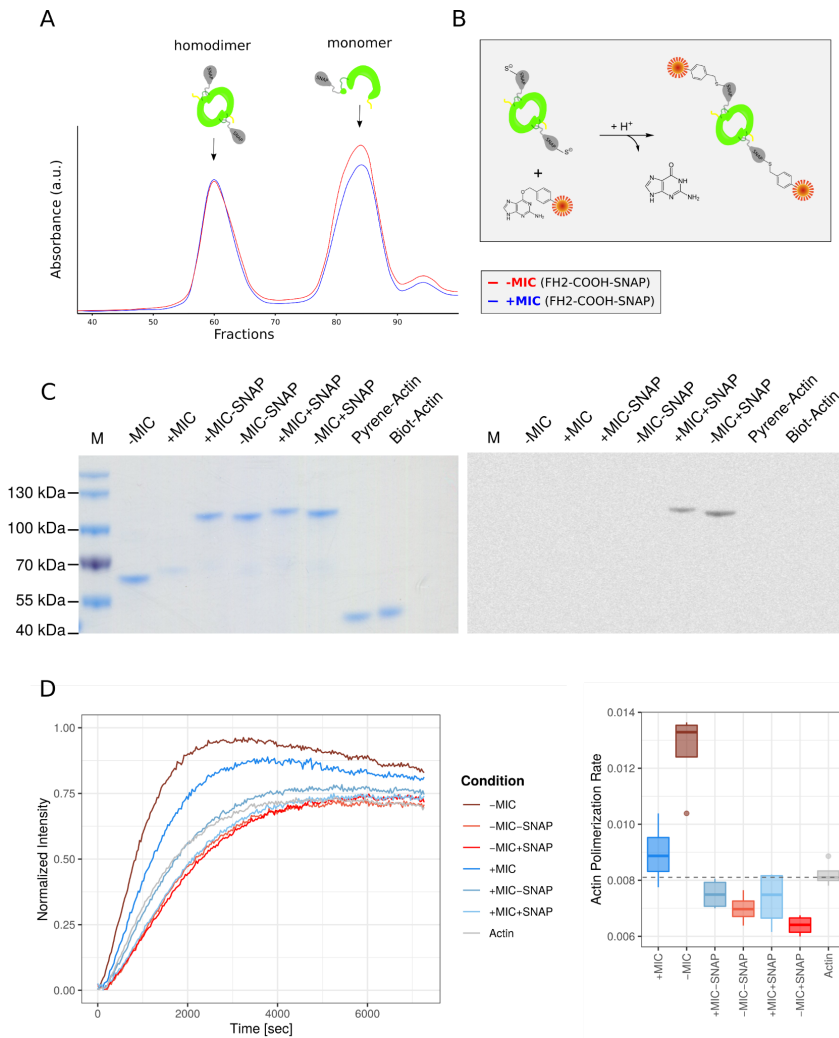


Figure II.8. Purification and activity of SNAP labelled DAAM1 FH2-COOH constructs. A) Representation of the FPLC elution profiles of DAAM1 SNAP-FH2-COOH fragments purified from bacteria. FPLC run was performed using HiLoad® 16/600 Superdex® 200 pg column. B) Schematic representation of fluorescence labelling of purified SNAP-FH2-COOH fragments. C) Left - Coomassie-stained SDS-PAGE gel summary of used proteins of interest throughout the course of this Thesis. Right - Fluorescence measurement of the SDS-PAGE gel (Left) at the 488 nm absorbance. D) Actin assembly differences between purified DAAM1 FH2-COOH fragments. Actin assembly was performed using 1µM actin, and 200nM of protein of interest. The right panel represents the actin polymerization rates calculated as slopes of curves at 50% assembly and shown as means ± SD based on Doolittle et al. 2013.

Regardless, we have decided to analyze the effect of fluorescently-labelled, SNAP-tagged protein variants on actin dynamics using TIRF microscopy. Figure II.9. confirms the functionality of newly purified and fluorescently labelled protein variants and confirms the different phenotypes observed previously for the two different variants. **+MIC+SNAP protein variant allows consistently higher actin elongation and branching, and -MIC+SNAP protein variant limits the elongation of actin structures but increases filament bundling** (Figure II.9.), as described before.

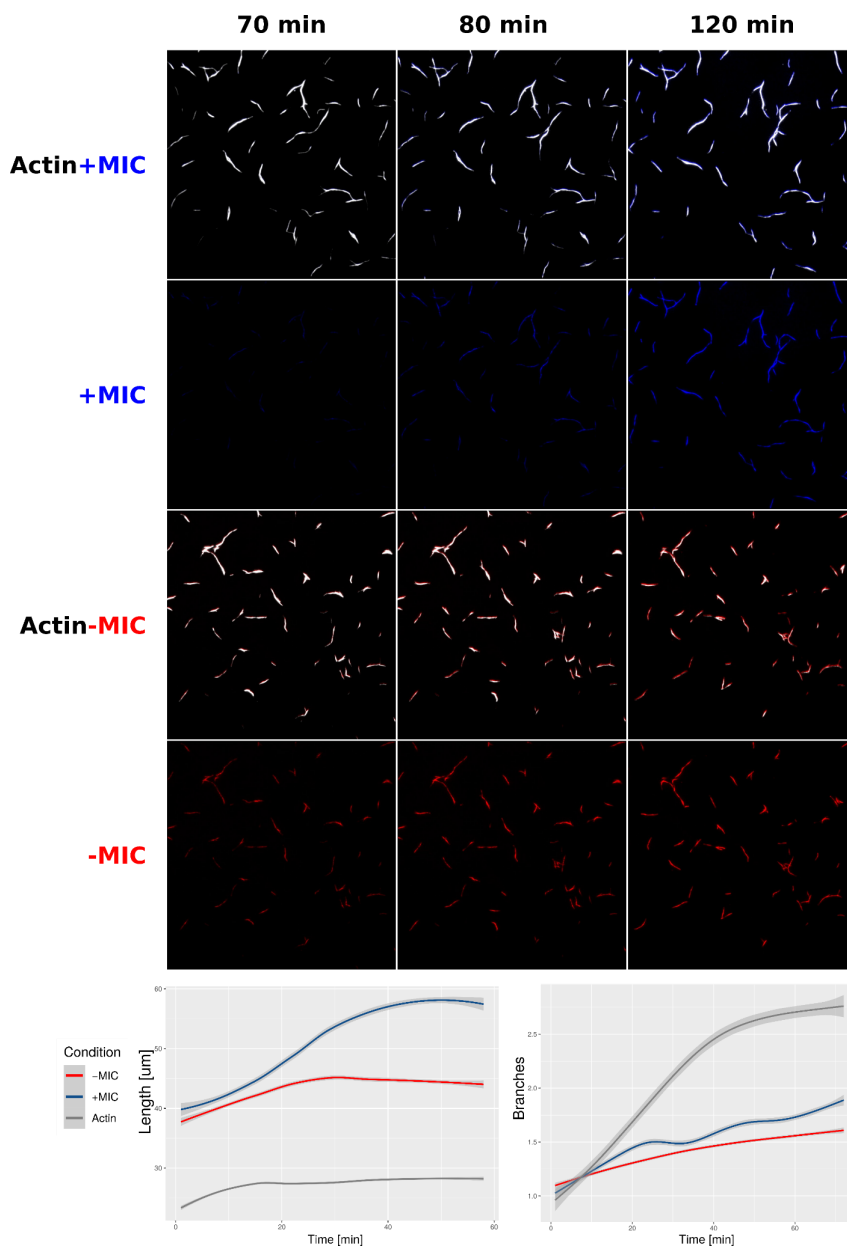


Figure II.9. Dual TIRF microscopy of actin polymerization. Dual TIRF was performed using two splice variants of fluorescently labelled DAAM1 SNAP+FH2-COOH proteins. Lower panel describes quantification of actin length and branch number.

Next, after reaching similar phenotypes for actin dynamics, we have finally decided to analyze the behaviour of fluorescently labelled SNAP-FH2-COOH protein variants on actin fibres (Figure II.9.). The first molecules of the -MIC+SNAP variant can be seen on actin fibres around 50 minutes after the experiment starts, while the +MIC+SNAP variant colocalization is seen around the 80th minute. Figure II.10.A describes single actin fiber magnification. Additionally, we have decided to use this time point (80 minutes) to quantify and compare the fluorescence signal of SNAP-FH2-COOH fragments on actin fibres. Manual analysis of individual actin bundles has shown **clear differences in the amount of protein-bound**, where the **intensity of -MIC+SNAP structures reaches significantly greater values** ($p=8.012e-07$; Wilcoxon rank-sum test; Figure II.10.B). Lastly, together with Raúl Gómez Riera, we have analyzed the amount of protein on actin filaments as a function of time. Figure Figure II.10.C describes the mean intensity of SNAP-FH2-COOH protein variants on single actin fibres.

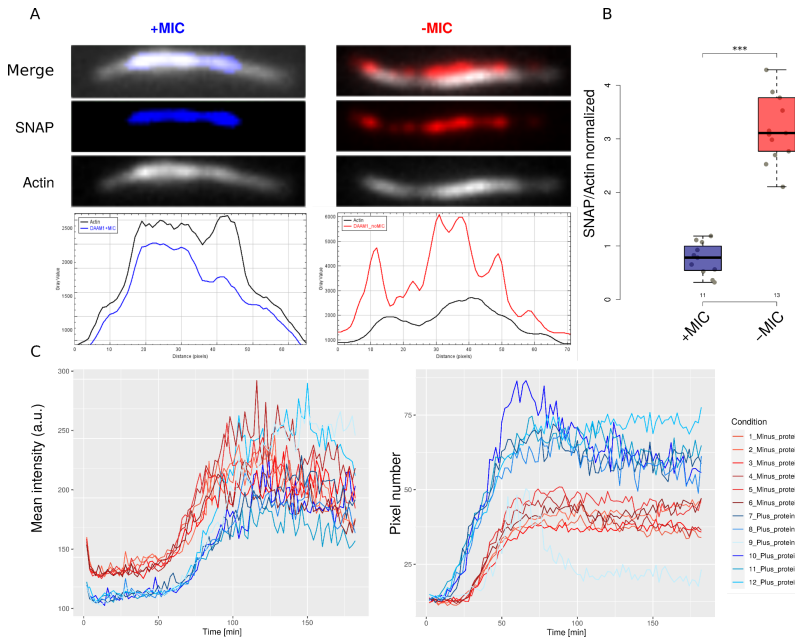


Figure II.10. Microexon lacking variant of FH2-COOH binds actin more efficiently. A) Manual quantification of protein concentration on actin fibers. Upper panel shows example fibres analyzed. Lower panel describes corresponding arbitrary fluorescence spectra. B) Quantification of SNAP/Actin fluorescence proportion. C) Automatic quantification of protein intensity and amount (by pixel number) on actin fibres in time. Significance codes: * $p \leq 0.05$, ** $p \leq 0.01$, *** $p \leq 0.001$.

In vitro analysis presented in this chapter took us one step closer to understanding the molecular basis of microexons' function. This approach was instrumental to put into evidence the microexons' role in modifying protein function, impacting actin dynamics and even its structure. Unfortunately, this biochemical approach has several limitations connected with the simplicity of the system. The cellular environment on the other hand is more complex. In the next chapter of this thesis, we will investigate the impact of microexon removal in cellular systems focusing on cultured neurons.

3. Role of the Daam1 microexon in neuronal differentiation and functioning

In this chapter, I have decided to investigate the role of microexon removal during *in vitro* differentiation of murine Embryonic Stem Cells (mESC) towards glutamatergic neurons. Together with the help of Marta Miret Cuesta (technician in our laboratory), we have prepared mESCs lacking the microexon at the genomic DNA (gDNA) level. Prepared cell lines were further differentiated into glutamatergic neurons using previously established protocols (Bibel et al., 2004, 2007). This system provides us with the perfect opportunity to study both early neuronal lineage commitment as well as neuronal functioning. The presented approach describes a more physiological environment (in comparison to our biochemical approach) yet less complex than the whole-animal *in vivo* approach.

3.1. Cell line preparation and neuronal differentiation

In order to determine the role of Daam1's microexon in neuronal differentiation and function, Knock Out (KO) cell lines were generated using the CRISPR-Cas9 system (Ran et al., 2013) with a double guide RNA strategy (Sakuma et al., 2015). As described in the first chapter, Daam1 microexon inclusion is a neuronal-specific event. In order to confirm microexon removal at the RNA level, we used a well-established protocol of differentiation of mESCs towards fully mature glutamatergic neurons (Bibel et al., 2004,

2007). Schematic representation of the differentiation performed is summarized in Figure III.1.A. Figure III.1.B shows the results of RT-PCR assays for two of the cell lines generated. In the control wild type (WT) condition, a slight microexon inclusion was already observed after four days of exposure of embryoid bodies (EBs) to retinoic acid (RA), reaching full inclusion soon after plating of neuronal precursor cells (NPCs) on a neuronal-specific substrate (DIV0). A similar microexon inclusion pattern was captured by publicly available RNA-seq data, further supporting microexons inclusion during differentiation (Figure III.1.C). Next, I analyzed the microexon inclusion in our KO cell lines at the mRNA level. An RT-PCR assay confirmed a clean microexon deletion with no associated mis-splicing (Figure III.1. B lower panel). Three WT and three KO cell lines were prepared and subsequently used in further cellular experiments.

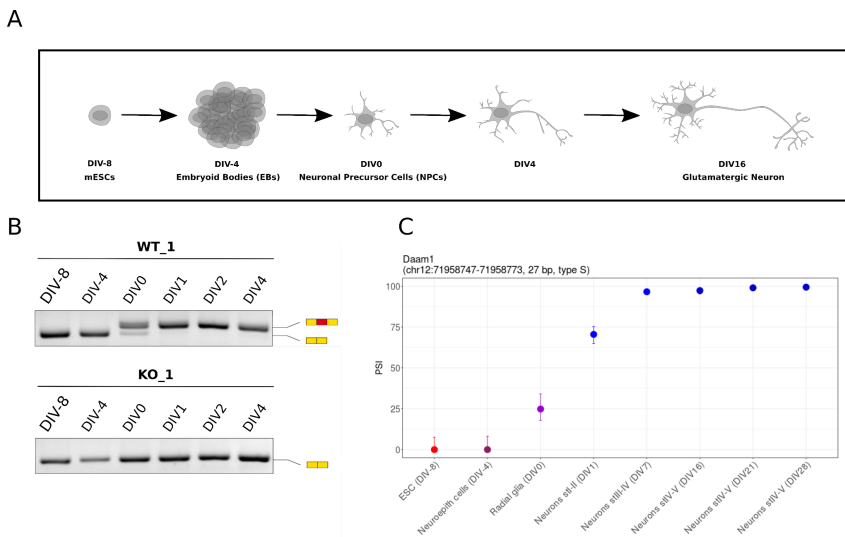


Figure III.1. Switch-like inclusion of Daam1 microexon during Neuronal Differentiation. A) Schematic representation of Neuronal Differentiation

protocol. B) RT-PCR validation of Daam1 microexon inclusion during neuronal differentiation. Microexon inclusion was analyzed at different time points corresponding to A). Detection was performed with primers in adjacent exons and ran on 2.5% agarose in the SB buffer as in Figure I.7. C) RNA-seq based PSI values for Daam1 microexon inclusion during the neuronal differentiation, based on VastDB. Percent Spliced In (PSI) describes the percentage of mRNA transcript with microexon included based on RNA-seq.

3.2. Impact of Daam1 microexon removal on early neurogenesis

To date, DAAM proteins were proven to be crucial players for neurite morphology and filopodia integrity in cultured cells (Jaiswal et al., 2013; Matusek et al., 2008; Szikora et al., 2017). Here, we assessed the impact of the microexon removal on the early stages of neuronal differentiation. In order to analyze the neuronal morphology, we stained DIV0+4h (day in vitro 0, 4 hours after plating) neurons with three different stainings (Figure III.2. A; more in the materials and methods section). Figure III.2. B depicts the schematic representation of early developmental stages described before in the Introduction section. Corresponding representations of fixed neuronal precursor cells 4 hours after plating have been highlighted in Figure III.2. A and B. No gross effect on the Daam1's cellular localization was observed upon microexon deletion. Fluorescence signal corresponding to Daam1 was observed in the regions corresponding to soma, neurites, growth cones as well as the singular filopodia, for both WT and KO cell lines. Pictures from multiple regions of interest (ROI) were analyzed and arbitrary fluorescence per ROI quantified for each

signal (Figure III.2. C). No significant differences between genotypes was detected for any of the stainings.

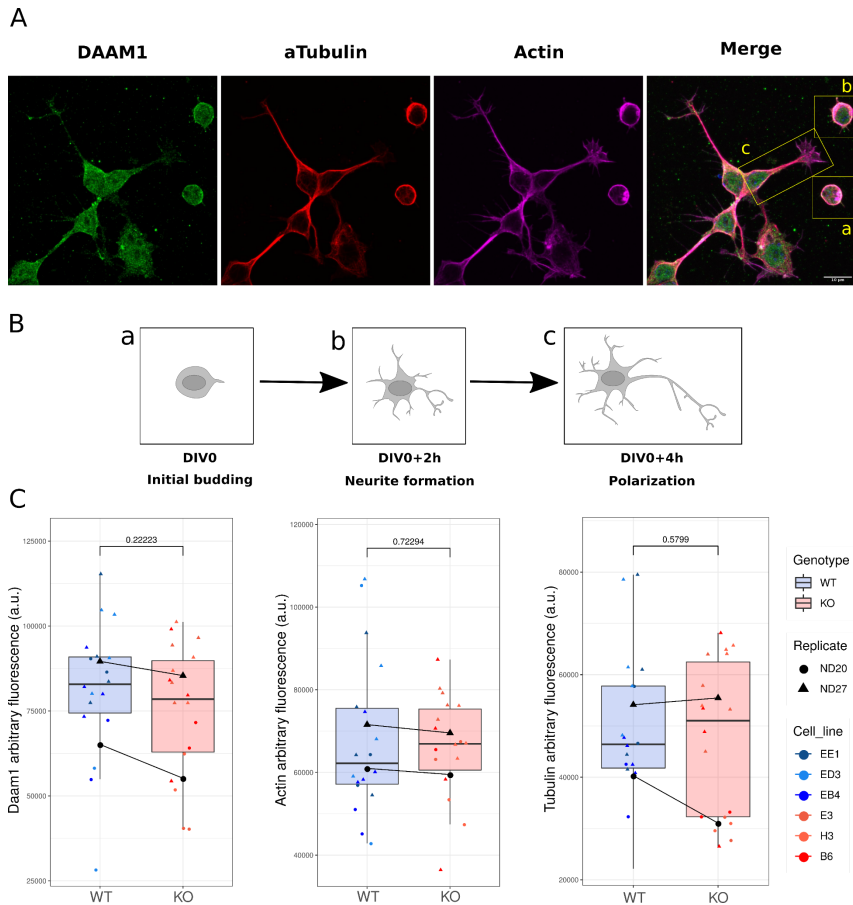


Figure III.2. Daam1 protein localization in neuronal precursor cells (NPCs). A) Representative images of NPCs (DIV0+4h), labelled against F-actin, alpha-tubulin and Daam1. B) Early stages of neuronal differentiation based on De silva and Dotti et al. 2002, and their representative stages during the experiment performed in A). C) Arbitrary fluorescence analysis of randomly selected regions of interest.

Since actin polymerization plays a key role in the growth cone formation, I performed additional analysis of prepared before fluorescence signals, with specific focus on growth cones. Single neurites encompassing growth cones were extracted and the

fluorescence was quantified in the regions spanning 10 μ m from the tip of the growth cones (Figure III.3A and B). **A small yet significant decrease in the Daam1 and Tubulin signal within growth cones was detected in KO compared to WT lines** (p=0.042 and p=0.030 respectively; ANOVA considering replicates, Figure III.3C). These results might indicate a lower amount of the Daam1 protein within the neuronal growth cones upon microexons removal. This, together with the analysis of axonal DAAM1 localization, and its role in microtubule coordination might explain lower amounts of α Tubulin in the growth cones. Nevertheless, the borderline statistical significance and the lack of reproducibility between the technical replicates urge caution and a more detailed analysis should be performed to confirm this observation.

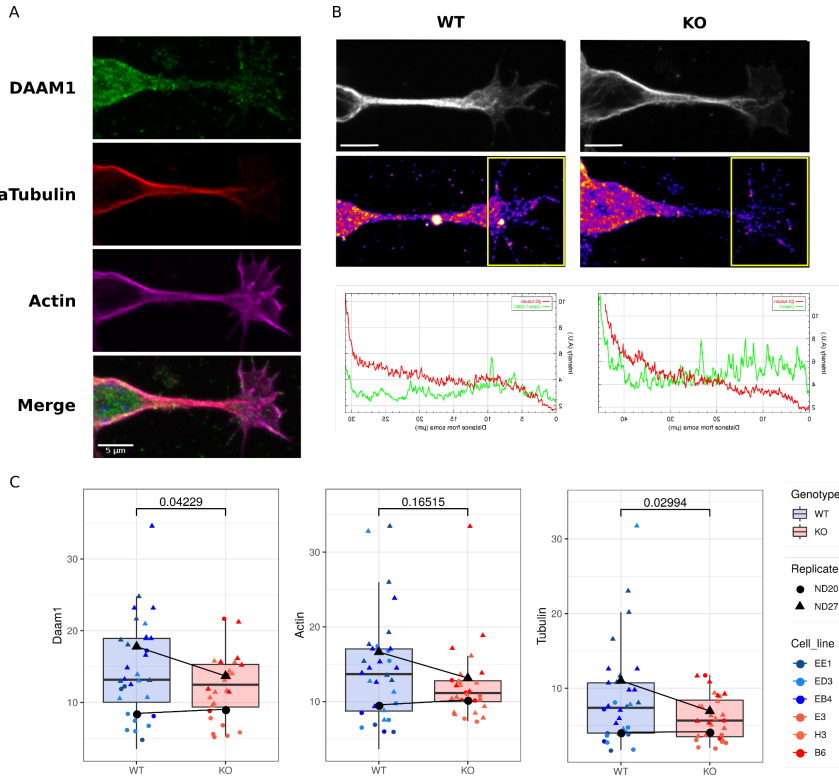


Figure III.3 Daam1 microexon impairs the localization in growth cones.

A) Growth cones of differentiating neuronal precursor cells (DIV0+4h), labelled against F-actin, tubulin and Daam1. B) Representative images of Daam1 distribution in the neurites and growth cones with corresponding arbitrary fluorescence along neurites. C) Arbitrary fluorescence analysis of spectra derived from the last 10 μ m from the tip of the growth cones.

As mentioned before, previous research investigated the DAAM role in filopodia formation and integrity (Jaiswal et al., 2013; Matusek et al., 2008). Matusek et al., 2008 found that, upon DAAM downregulation or overexpression, filopodia length and number changed significantly in the neurites of *Drosophila* primary neuronal cultures. To investigate the potential impact of microexon removal on filopodia formation and growth I evaluated filopodia morphology. Figure III.4.A shows an example of filopodia

selection. The length of all filopodia was measured showing a **slightly higher length of filopodia in the KO cell lines** compared to the controls ($p=0.033$, ANOVA considering technical replicates). The longer filopodia phenotype could be partially explained by our biochemical results from the previous chapter. The FH2 domain lacking the microexon binds actin more efficiently, causing higher actin nucleation. One possibility would be that, in this cellular system, the Daam1 splice variant lacking the microexon causes faster nucleation of actin, followed by more efficient elongation of filopodia by WASP proteins. Additionally, I quantified the number of filopodia along the longest neurite and within growth cones. No significant differences were detected in KO cell lines compared to the controls (Figure III.4. C and D respectively).

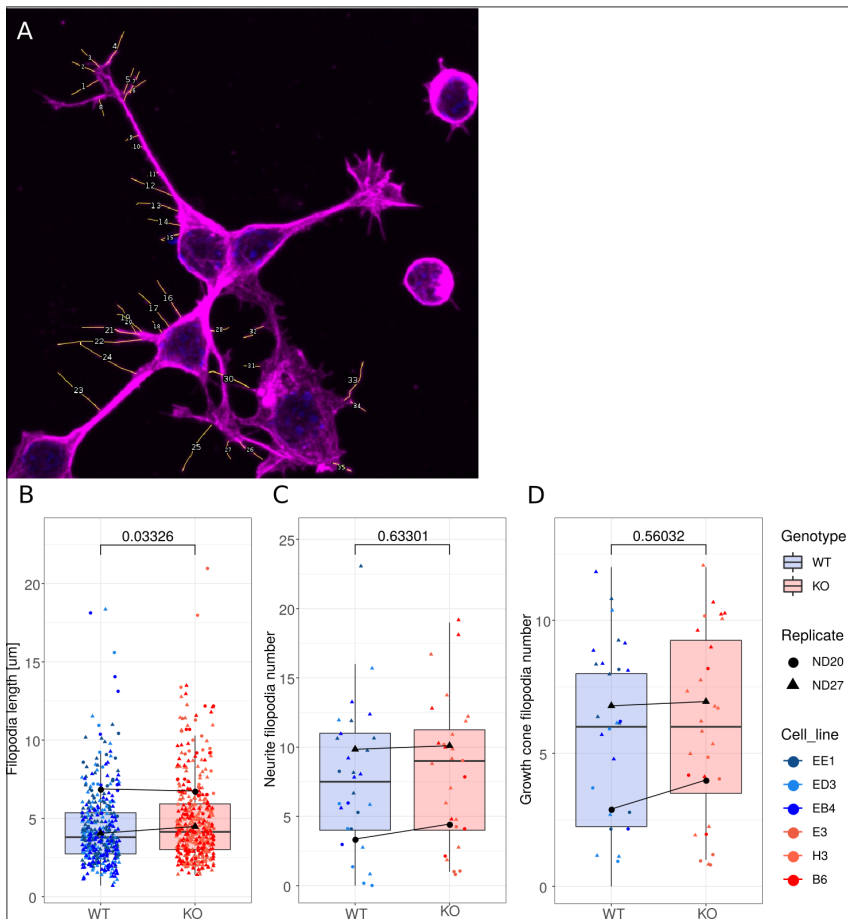


Figure III.4. Filopodia formation analysis in neuronal precursor cells (NPCs) at DIV0+4h. A) Representative image of F-actin staining of NPCs with examples of filopodia analyzed. B) Analysis of filopodia length in NPCs. C) Analysis of filopodia number in neurites. D) Analysis of filopodia number in growth cones.

Lastly, I analyzed the distribution of Daam1, Actin and α Tubulin proteins along the filopodia. Previously Jaiswal et al. 2013 found that Daam1 localization within filopodia in mouse cancer B16F1 cells changes depending on its interaction with Fascin. In order to assess Daam1 localization changes upon microexon removal, relative spectra of Daam1, Actin and α Tubulin were analyzed. I

performed a quantification of the signal intensity along the first 5 μm of filopodia starting from its tip. The length of all filopodia analyzed spanned between 6 to 14 μm . Similarly to previous observations, a small decrease in Daam1 protein was detected in KO lines compared to the controls ($p=0.015$, ANOVA considering technical replicates) suggesting possible mislocalization within the filopodia (Figure III.5. B).

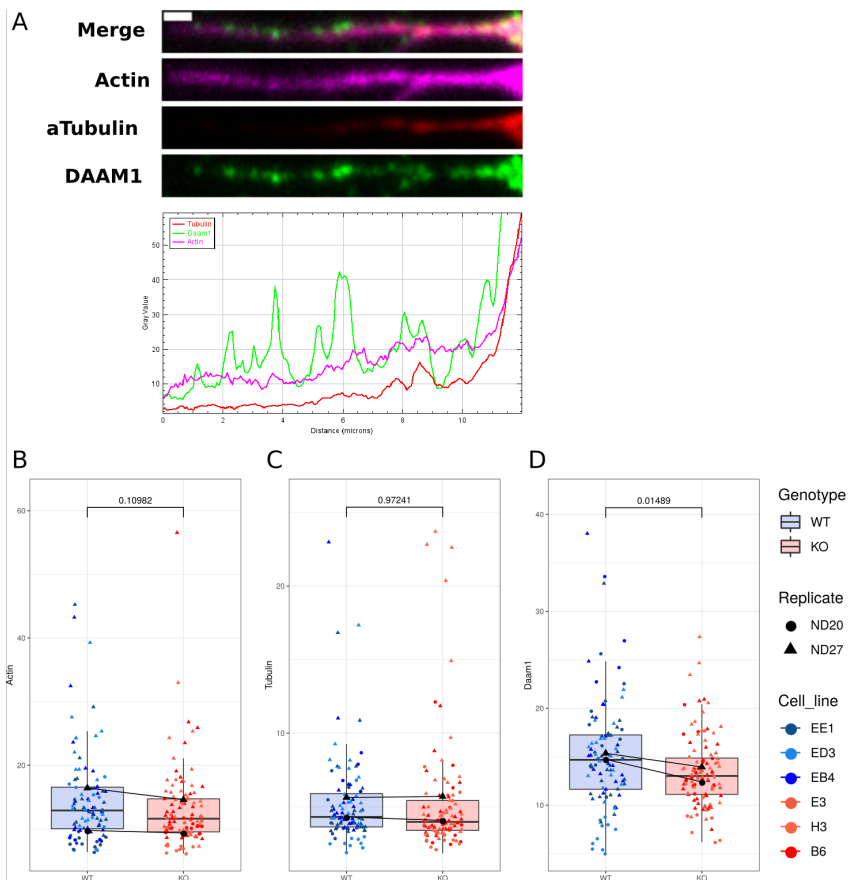


Figure III.5. Protein distribution in neuronal precursor derived filopodia.
A) Representative images of analyzed filopodia (DIV0+4h), labelled against F-actin, aTubulin and Daam1 together with fluorescence spectra. Arbitrary fluorescence analysis of spectra derived from the last 5 μm from the tip of the filopodia where the B) Actin, C) aTubulin, D) and Daam1 have been analyzed.

All filopodia length spanned between 6-14 μm .

These results suggest rather no major role of Daam1 microexon in filament morphology. Regardless, taking into account relatively low significance and the variability between the replicates, a more detailed analysis should be performed to reassure of this observation. The fluorescence analyses presented here are a valuable tool for the analysis of neuronal morphology. Nevertheless, one should take into account the early stage of the neuronal differentiation analyzed as well as the static character of a fixed cellular system.

3.3. Increased neuronal activity upon microexon removal

After the morphology analyses during the early differentiation stages, I decided to analyze the role of Daam1 microexon in live cells at different stages of neuronal differentiation. I focused on the analysis of calcium ions, which are versatile intracellular signalling molecules essential for a variety of processes throughout neurogenesis. Calcium ions are involved in many processes, from cellular proliferation to growth cone guidance and synaptic function (Grienberger and Konnerth, 2012). Together with Gerard Cantero Recasens (Malhotra lab at CRG), performed calcium imaging experiments in cultured cells to assess the possible impact of Daam1 microexon removal on calcium signalling s. We observed no significant differences at the early stages of neuronal differentiation

(DIV1 and DIV7) further supporting no major role of microexon in early development. Interestingly, starting from DIV14, a time point when neuronal synaptogenesis is first observed, significant differences in calcium influx have been observed between WT and KO cell lines (Figure III.6). KO cell lines show higher Ca^{2+} influx upon neuronal depolarization. This difference could be a result of morphological changes in neuronal synapses or differences in synaptic vesicle cycle, both actin-dependent. As described in the Introduction, actin is an essential player in both morphology of the neuronal synapses as well as their function. In the Section 2 (TIRF microscopy), we showed that the microexon removal impairs the formation of complex actin structures, characterized by filament branching. Structural differences observed could in fact impact neuronal exocytosis as neurotransmitter-containing synaptic vesicles are dependent on the spatiotemporal segregation of SV pools maintained by complex actin structures. Here, removal of the microexon could potentially loosen the tightly controlled organization and delivery of SV towards the active zone as well as their exo- and endocytosis, resulting in increased SV release and thus neuronal activity.

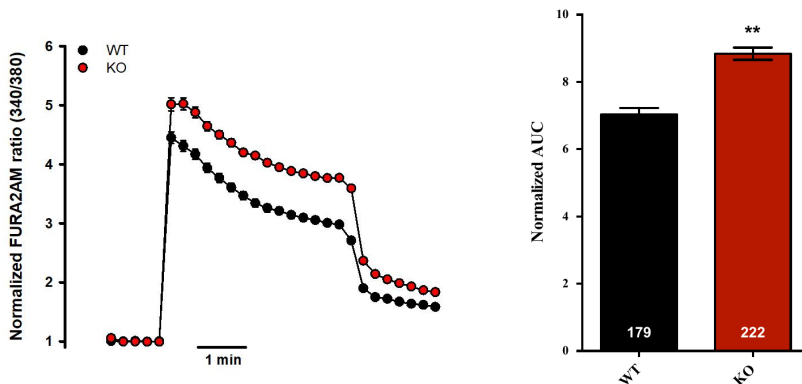


Figure III.6 Daam1 microexon removal increases calcium influx in mature neurons. Significance codes: * $p \leq 0.05$, ** $p \leq 0.01$, *** $p \leq 0.001$.

Therefore, in order to further investigate the role of the microexon in neuronal function, we have decided to expand our investigation focusing on differentiation stages where synaptic connections are thought to be formed.

Daam1 was found to colocalize in presynaptic regions (Wagh et al., 2015). Considering that differences in calcium currents correlate with the synaptic formation stages in cultured glutamatergic neurons, we next analyzed the Daam1 localization in synaptic regions. We found that Daam1 co-localizes with the synaptic marker Syp-1 in both KO and WT cells with no major differences, suggesting that microexon removal does not abolish synaptic localization of Daam1 (Figure III.8).

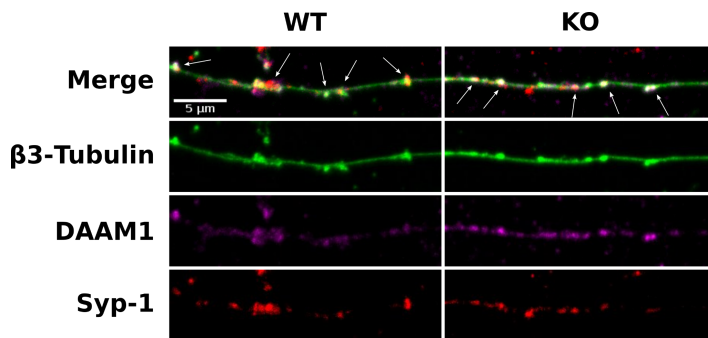


Figure III.7 Daam1 localized in synaptic terminals. Representative images of neuronal synapses, labelled against synaptic marker Syp-1, B3-Tubulin and Daam1 in control and Daam1 microexon lacking cultures.

To further understand the impaired functioning of our neurons, we have decided to repeat the calcium imaging experiments challenging the system with commonly used chemical inhibitors. Latrunculin A (LatA), promotes F-actin depolymerization by sequestering available G-actin monomers. Using a DMSO vehicle as a control, showed consistently higher neuronal activity in KO cell lines in both DIV14 and DIV21 (Figure III.8A and B, respectively). Application of 5 μ M LatA for 30min resulted in reduced calcium influx in both WT and KO cell lines. Considering the higher initial calcium flux of the KO neurons, we have calculated the ratio between calcium flux change before and after LatA application. KO neurons consistently showed a stronger reduction, probably as a result of an already impaired actin network within the neuronal synapses. Next, the application of a small molecular inhibitor of formin FH2 domains (SMIFH2), which inhibits formin-driven actin polymerization, had an opposite to LatA effect. We found that exposure of neuronal cultures to SMIFH2 slightly increased the calcium influx in WT and KO cell

lines. Again, in DIV21 the difference upon SMIFH2 exposure is greater for KO than WT cell lines. This further supports the impaired activity of Daam1 FH2 domain during actin polymerization, as blocking formins by the SMIFH2 has a similar effect to microexon KO.

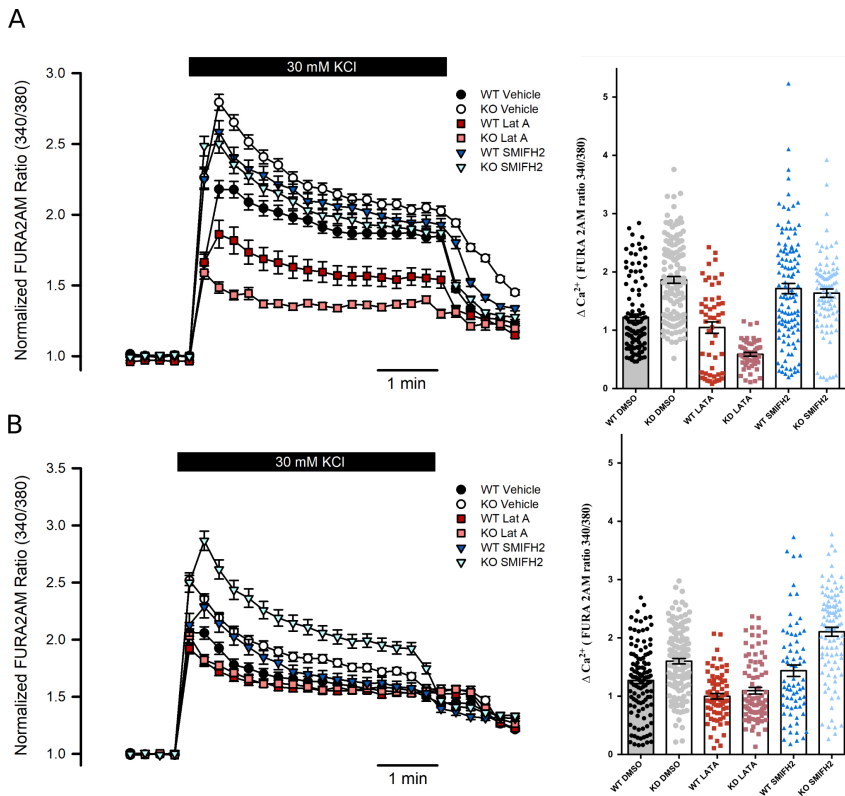


Figure III.8 Effects of the formin inhibitor SMIFH2 and actin polymerization inhibitor Latrunculin A (LatA) on calcium currents on differentiated glutamatergic neurons.

A) Effects of inhibitor application in glutamatergic neurons DIV14.

B) Effects of inhibitor application in glutamatergic neurons DIV21.

To further assess the differences in activity of glutamatergic neurons, we investigated the expression of immediate early gene (IEG), at the protein level. IEGs are part of the first cellular response to different stimuli and markers of neuronal activity. So far many IEGs have been described with different specificity. Here, we decided to focus on the amount of Activity-regulated cytoskeleton-associated protein (Arc), as it was found to interact with F-actin and ABPs, and as it is thought to play a crucial role in long-term synaptic plasticity (Nikolaienko et al., 2018; Park et al., 2008). Elevated levels of Arc were detected by immunohistochemical validation in neuronal cultures ($p=1.91e-06$; Figure III.9). Quantification of Arc immunostaining performed in three technical replicates and considering three WT and three KO cell lines consistently showed an increase in the number of neurons expressing Arc. These data suggest that up-regulation of IEGs is strongly linked to increased activity of neurons further confirming the impact of microexon removal in neuronal functioning.

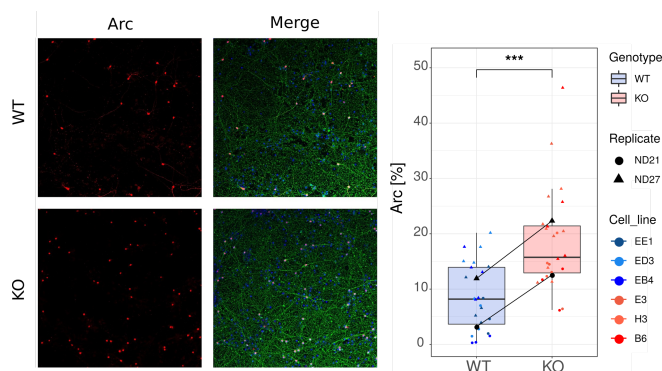


Figure III.9 Daam1 microexon removal increases protein levels of Arc in glutamatergic neurons (DIV21). Left panel - Immunohistochemistry of Arc, B3-Tubulin and DAPI staining. Right panel - Arc positive nuclei quantification across images. Significance codes: * $p \leq 0.05$, ** $p \leq 0.01$, *** $p \leq 0.001$.

4. Roles of Daam1's microexon in nervous system development

The last steps of this project were focused on the *in vivo* evaluation of the importance of Daam1's microexon for the development and functionality of the nervous system. We have used mice as a model organism, as during previous analysis we identified functional impairments in glutamatergic neurons derived from murine embryonic stem cells (mESCs). Moreover, the mouse is a perfect model for behavioural analysis with multiple, well established behavioural experiments that will help us to understand the role of the microexon in nervous system functioning, memory formation and learning. Generation of the mouse mutant line was performed by blastocyst injections of genetically modified mESCs. This was performed in collaboration with Marta Miret Cuesta and our on-site Tissue Engineering Facility (Materials and Methods section for more details). After a successful generation of a stable mouse model, together with Marta Miret Cuesta and in collaboration with Mara Dierssen Sotos (CRG Barcelona, Spain) we performed behavioural experiments during the pre-weaning development. Analysis of pre-weaning behaviour is critical for assessing nervous system development and provides a perfect opportunity to identify changes upon genetic manipulations in mice. Many motor tests in neonatal mice have been established, allowing the characterization of motor deficits (Feather-Schussler and Ferguson, 2016) or psychomotor impairments (Roper et al., 2020). Figure IV.1 describes the developmental time points at which the experiments

were performed, with a performance summary which will be described in detail below. Experimental stages were adjusted in order to reduce handling as well as correlate phenotypes with established developmental landmarks (eye-opening, dentate gyrus formation etc.). Lastly, based on the previous reports on Daam1's function in axon growth and brain connectivity (Matusek, 2006; Matusek et al., 2008; Colombo et al., 2013; Avilés and Stoeckli, 2016; Mollink et al., 2019) we have formed a collaboration with Eloísa Herrera González de Molina (Instituto de Neurociencias, Alicante, Spain) to unravel the impact of Daam1 microexon removal in these processes. All of the experiments have been performed comparing WT and KO siblings, coming from the crossing of heterozygotic parents. This approach allowed us to analyze the differences from the same genetic background and on top of it normalize possible epigenetic effects.

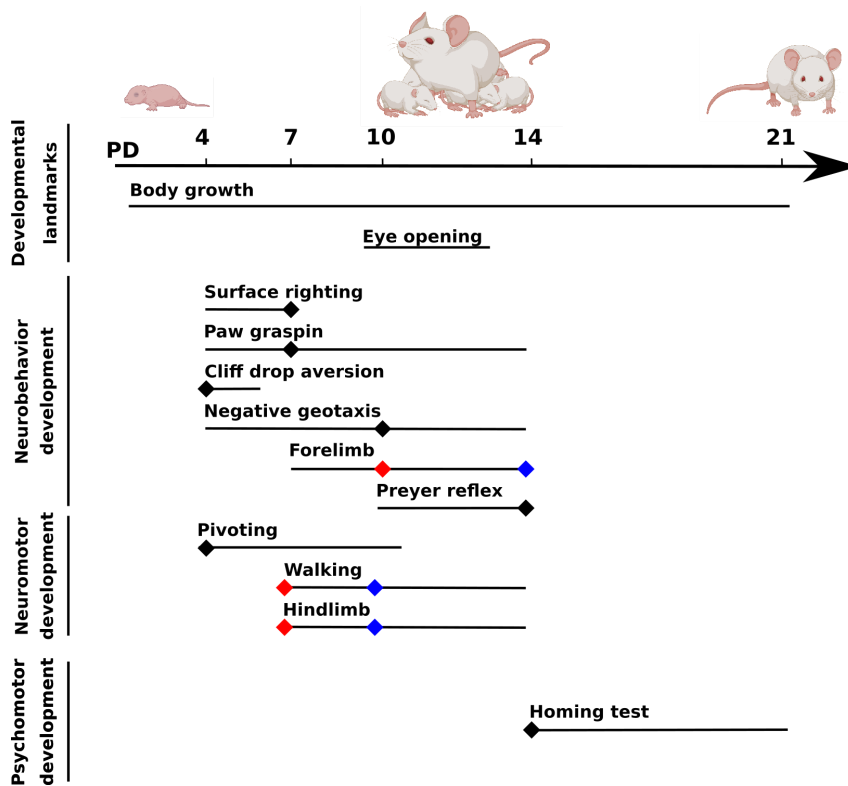


Figure IV.1. Mouse postnatal development timeline and neurodevelopmental experiments performed. All neurodevelopmental experiments have been performed on postnatal days 4, 7, 10, 14 and/or 21. The line represents the span between the start and the end time point of the protocol. Diamond-shaped marker stands for the average age at which the majority of mice perform the experiment. Red marker - start performance by KO mice, Blue marker - start performance by WT mice. Black diamond - similar performance regardless of the genotype. PD - postnatal days. Adapted from Roper et al. 2020

4.1. Mice postnatal neuromotor development

a) Pivoting and walking analysis

We started the neurodevelopment analysis by analyzing the establishment of the cranio-caudal behaviour of our pups. We have analyzed the transition between rotatory locomotion (called pivoting typical for early neonatal stages) and straight-line walking. This transition occurs usually between postnatal days 7 and 10 (PD7 and PD10) as a result of the increase in limb coordination and neuromotor strengthening (Roper et al., 2020). As expected, major differences in behaviour were observed across timepoints in the control wild-type (WT) pups (Figure IV.2.A). At the early stages typical rotatory motion was observed, which decreased naturally with time. WT mice decreased their pivotings on PD10 followed by immediate, straight-line walking (Figure IV.2.B). Surprisingly, cranio-caudal behaviour occurs slightly differently in the knock-out (KO) mice, with heterozygous (HET) individuals displaying an intermediate phenotype. Although not significantly, the pivoting number was lower at PD7. At PD10, however, this trend was reversed and mutant mice had significantly higher rotatory locomotion ($p=0.011$). Moreover, mutant mice started their walking significantly faster ($P=0.010$, PD7), after which a delay in comparison to the WT was observed (PD10: HET $p=0.008$, KO $p=0.001$).

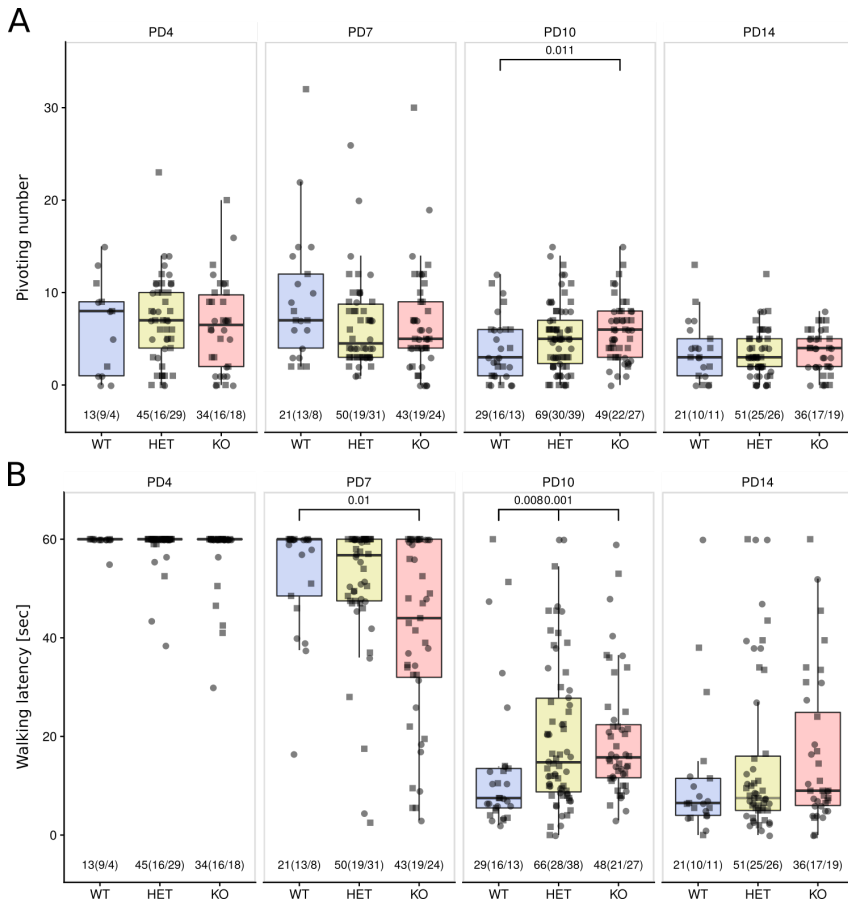


Figure IV.2. Cranio-caudal behaviour changes mice upon Daam1 microexon removal. A) Analysis of the mice's pivoting pattern during development. B) Analysis of the walk latency during mice development. Numbers below each boxplot represent the total mice number, and in brackets males and females respectively.

b) Hindlimb and forelimb strength assessment

Differences observed in the cranio-caudal analysis could result from altered neuromotor strengthening. Therefore, we next assessed the hindlimb and forelimb strength of our pups. Hindlimb and forelimb strength analysis has been proven to be informative assessments of the proper neuromuscular function in the cerebral palsy mice model (Feather-Schussler and Ferguson, 2016).

In order to assess the forelimb strength, including arm and paw strength, we placed each mouse on a thin wooden bar and they could hang to it using their front limbs only. During the suspension, latency to fall off from the bar was measured. Falling is eventually caused by muscle tension and fatigue, which leads to bar release. Mice were able to perform the experiment starting from PD7, with a constant increase in suspension time throughout the time course. No significant differences between genotypes were observed at PD7 (IV.3 A). On the contrary, at PD10, heterozygous mice showed a significant increase in suspension time ($p = 0.009$, Wilcoxon rank-sum test), while the full KO mice showed the same trend but did not reach statistical significance ($p = 0.335$, Wilcoxon rank-sum test).

Next, we assessed the hindlimb strength and posture. During the experiment, a pup is placed gently inside a tube, facing downwards and suspended only by its hindlegs, which are bent over the edge. No difference was observed in hindlimb suspension time (Figure IV.3 B), yet the microexon KO mice showed significantly better

posture (represented by the higher score reached) at PD10 (Figure IV.3 C; $p=0.007$, Wilcoxon rank-sum test). At the PD10 stage, the majority of KOs and HETs scored the maximum hanging score, showing higher hindlimb separation, probably as a result of stronger hindlimbs (Figure IV.3 C; Average hanging score of WT: 2.821 (n = 13), HET: 3.25 (n = 66), and KO: 3.553 (n = 47)).

c) Negative Geotaxis

After the basic neuromotor behaviour assessment, we focused on more complex neurobehaviours. A negative geotaxis test allows the assessment of multiple aspects of neuronal development at the same time. For this experiment, a mouse is placed on the slope facing down and the behaviour is analyzed. Mice will turn upwards and the latency to do so is recorded and compared. This seemingly simple experiment depends on the coordination of many developmental aspects. First of all, vestibular function is required to detect gravitational cues. Additionally, paw strength and motor coordination are assessed as a proxy of sensory and proprioceptive function (Feather-Schussler and Ferguson, 2016; Roper et al., 2020; Ruhela et al., 2019).

Three features were used to assess the negative geotaxis performance:

- the degree of the rotation achieved after 2 minutes,
- the time latency to move upwards (full 180°),
- and the directionality of the movement (left or rightwards).

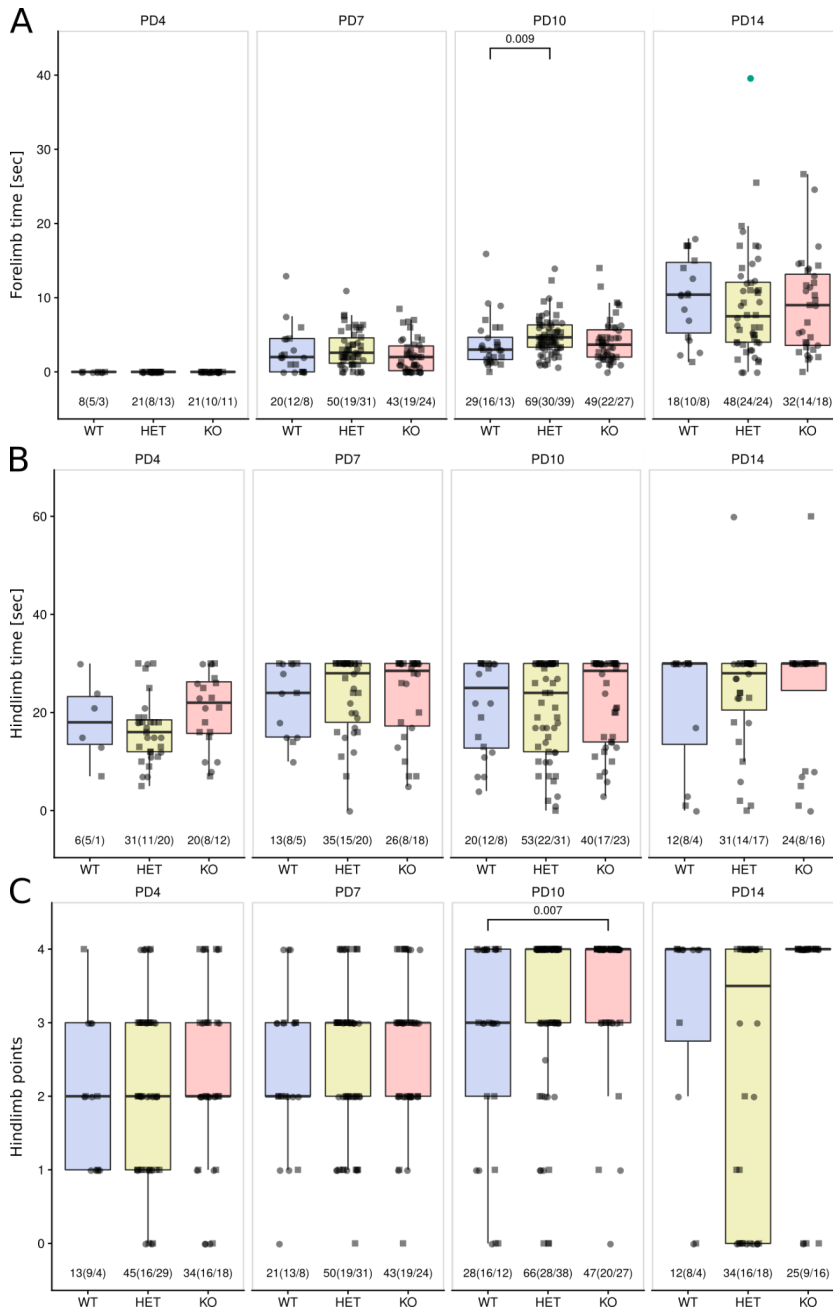


Figure IV.3. Daam1 microexon removal increases hindlimbs and forelimbs strength in mice during early development.

A) Analysis of the forelimb strength through the fall latency during development. B) Hindlimb posture analysis correlated with strength. C)

Analysis of the hindlimb strength correlated with the fall latency throughout the early development. Numbers below each boxplot represent the total mice number, and in brackets males and females respectively.

As expected, performance improved throughout development. However, no significant differences in the score or latency time were observed between the WT and KO mice (Figure IV.4 A and B). At PD10, a potentially interesting pattern was observed where the majority of the microexon-lacking mice (either HET or KO), did not turn at all during the entire duration of the experiment (Figure IV.4 A;). The results, yet potentially interesting, did not reach significant differences. Surprisingly, at PD7 significant differences in the rotation side preference were observed (Figure IV.4 C). To quantitatively assess this, we performed the following analysis. During the Negative geotaxis experiment, two trials per mouse were performed where the mouse is rotated from facing upwards on the slope to facing downwards. Here, for both trials, we analyzed the side to which they rotated: rotation towards the right side was scored as a “+1” point and the left side as a “-1”. Thus, a mouse can accumulate up to two points (positive or negative). By comparing the distribution of scores per genotype, we found that, specifically at PD7, KO mice showed a significant bias to turn to the right side ($p=0.022$, Wilcoxon rank-sum test).

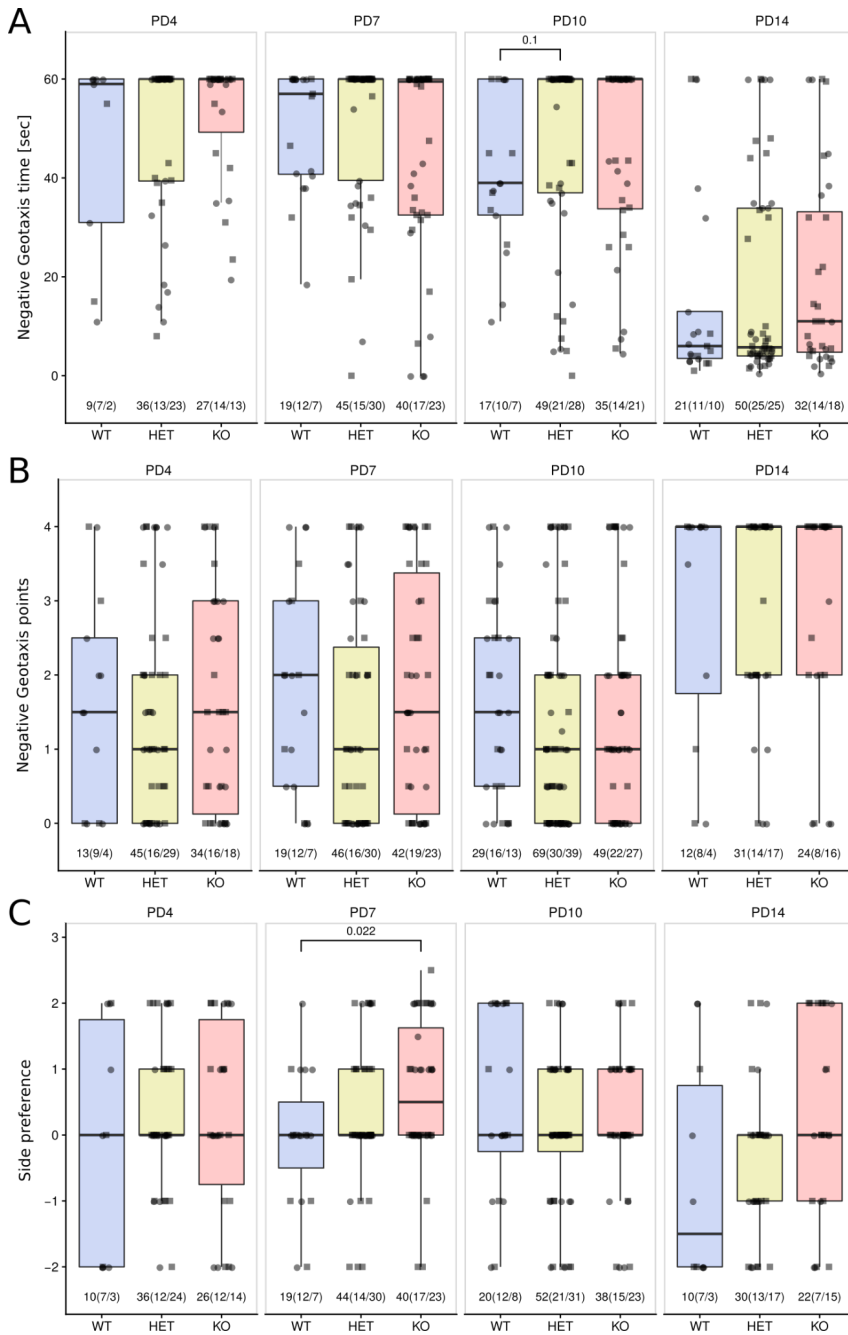


Figure IV.4. Negative Geotaxis assessment. Daam1 microexon removal increases hindlimbs and forelimbs strength in mice during early development. A) Analysis of the performance latency considered as a 180°

rotation up the incline. B) Performance score during the experiment. Each 45° rotation granted 0.5 points to a subject. C) Analysis of the rotation side chosen by a mouse. Numbers below each boxplot represent the total mice number, and in brackets males and females respectively.

d) Grasping reflex, Prayers reflex and cliff aversion

Lastly, we performed the assessment of basic reflexes that are important for neurobehaviour. Cliff aversion was analyzed as the response to escape from the edge of a “cliff”, here scored as one point when there is a clear response (escape) and zero points when no response was observed. As expected, already at PD4, a substantial fraction of mice performed the experiment, and no significant differences were observed throughout the analyzed development (Figure IV.5 A). Similarly, no significant differences were found while assessing the grasping reflexes of our pups (Figure IV.5 B). Here, the grasping reflex was assessed as a clear response upon the light touch of the paw’s bottom side, where each response was granted one point. The stronger response was usually observed in the forelimb paws, where already at PD4 clear responses were recorded. Subsequently, mice showed clear responses in the hindlimbs from later stages. No significant differences were observed between genotypes (Figure IV.5 B). Lastly, we have analyzed the Prayer’s reflex defined as a clear, full-body response to a noise. Here, nearly all mice gained the reflex at PD14 regardless of the genotype (Figure IV.5 C).

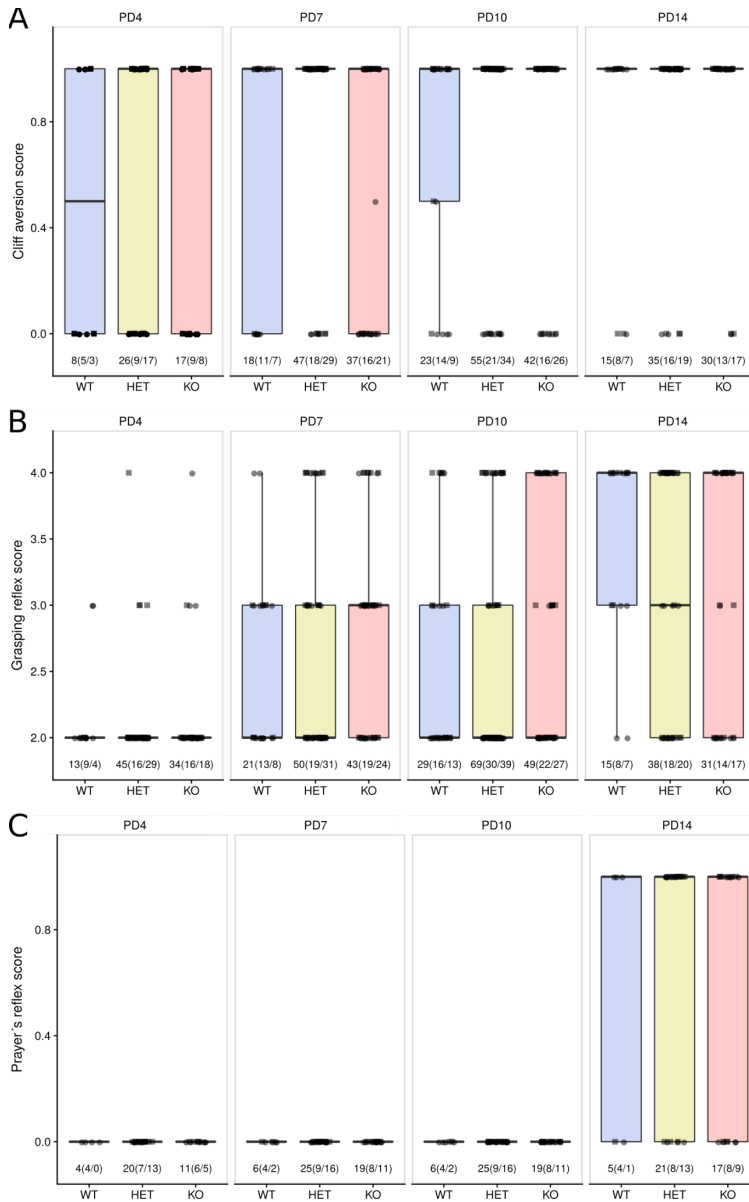


Figure IV.5. Grasping reflex, Prayers reflex and cliff aversion analysis during early development. A) Analysis of the cliff aversion test analyzed as clear escape from the cliff edge (1 point) or lack of response (0 points). B) Grasping performance score counted as the number of paws where the reflex was observed. C) Preyer's reflex score was analyzed as a clear response to noise (1 point) or its lack (0 points). Numbers below each boxplot represent the total mice number, and in brackets males and females respectively.

4.2. Molecular analysis of the Daam1 KO mice

In the 3rd Chapter, the potential roles of the Daam1 microexon in early neuronal development and synaptic-dependent neuronal activity were investigated. Alterations in filopodia formation, elongation and integrity could potentially impact neuronal migration and axon guidance processes *in vivo*. In this section, we assessed these processes with the help of the Herrera lab (Instituto de Neurociencias de Alicante). Additionally, we tried to confirm *in vivo* the higher neuronal activity upon microexon KO that we reported in the mESC-derived excitatory glutamatergic neurons. In order to do so, we focused on the hippocampus, which (as described in the Thesis Introduction) is one of the most thoroughly investigated parts of the brain and where various sensory, emotional as well as cognitive components converge.

a) Axon guidance

We performed *In Utero* Cortical electroporation in order to analyze possible axon guidance defects. Figure IV.6.A is a schematic representation of the experiment performed. Figure IV.6.B presents comparison of coronal sections between WT and KO mice at P4 electroporated with EGFP encoding plasmid at embryonic day 15.5 (details in Materials and Methods). No gross differences in axon guidance were observed. In both WT and KO animals there was no clear defects in corpus callosum (CC) crossing towards primary somatosensory cortex (S1). Additionally, we analyzed possible defects in neuronal morphology with specific focus on the distance

from neuronal soma towards the first branch as advised in (Kawabata Galbraith et al., 2018). No significant difference was observed in analyzed animals (Figure IV.6.C).

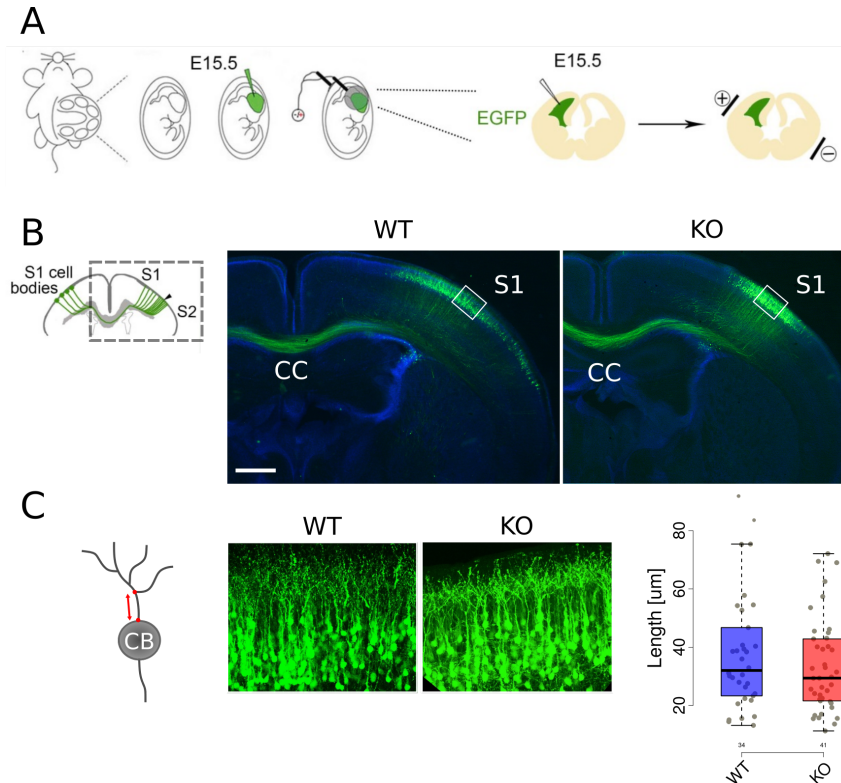


Figure IV.6. In utero electroporation and contralateral callosal projections analysis. A) Schematic representation of *In Utero* electroporation performed. B) Coronal sections of P4 mice unilaterally electroporated with plasmids encoding GFP. C) Analysis of the dendrite length to the first branch. CC - corpus callosum, S1 - primary somatosensory cortex. Scale bar 500 μm .

b) Hippocampal structure and activity analysis

Hippocampal structure and activity were analyzed after transcardiac perfusion of PD21 mice, brain extraction and consecutive brain sectioning (more details in Materials and Methods section). Brain

cryosectioning was performed by Alexis Ràfols Mitjans from the Tissue Engineering Unit (CRG), and Bregma sections between -1.34 mm to -2.54 mm were submitted for IHC. No gross differences in the hippocampal structure were observed between WT and KO mice. Next, we performed size quantifications of one of the hippocampal subcomponents, namely the dentate gyrus (DG). No significant differences were observed between the size of the DG in WT and KO mice (Figure IV.7). However, in line with the cell culture experiments, significant differences were identified in the relative number of Arc positive nuclei between WT and KO mice (Figure IV.7, Arc normalized to the DG area, $p = 2.3e-11$, Wilcoxon rank-sum test). Arc immunostaining was performed using the same antibody as the one used in the neuronal cultures. This phenotype further confirms previous observations of increased neuronal activity in neuronal cultures.

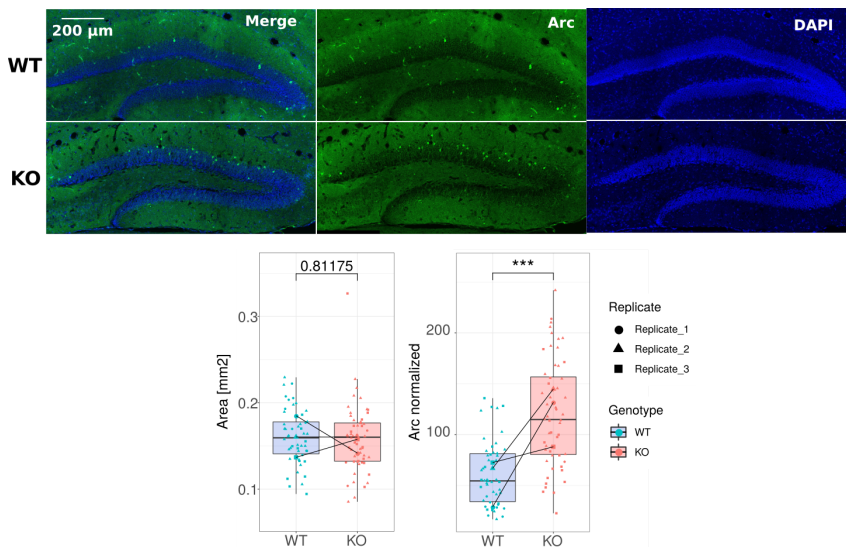


Figure IV.7. Daam1 microexon removal increases protein levels of Arc in the dentate gyrus of the hippocampus in mice (PD21). Upper panel - Arc

immunohistochemistry with DAPI stained nuclei. Lower panel - Dentate gyrus size quantification and Arc positive nuclei quantification in hippocampal dentate gyrus across images. Arc nuclei number was normalized to the dentate gyrus size. Significance codes: * $p \leq 0.05$, ** $p \leq 0.01$, *** $p \leq 0.001$.

b) Bioinformatic analysis of the hippocampal RNA-seq

The high neuronal activity found in neuronal cell cultures and further in mouse hippocampal slices suggests potential transcriptional changes. In this subchapter, we thus investigated possible genome-wide transcriptional changes that might have resulted from the deletion of the microexon of *Daam1*. We performed RNA-seq at two developmental stages, namely PD14 and PD21, within which any changes in gene expression could help us to understand the neurobiological impairments of our mice. The RNA-seq analysis was done in collaboration with Luis Pedro Iñiguez (computational expert from our laboratory).

We first did a principal component analysis (PCA) on our data (Figure IV.8). Here two main factors were found to be responsible for the sample clustering. PC1, explaining 41% of the variation in gene expression across our samples, corresponds to the age of the mice analyzed. On the other hand, PC2, which explains around 12% of the gene variance between samples, correlates with sex. Separation of male and female samples was stronger at PD21, which is in line with the sexual maturation of pups. In the next steps of the analysis, mice sex was considered as a factor for correction in the Deseq2 analysis.

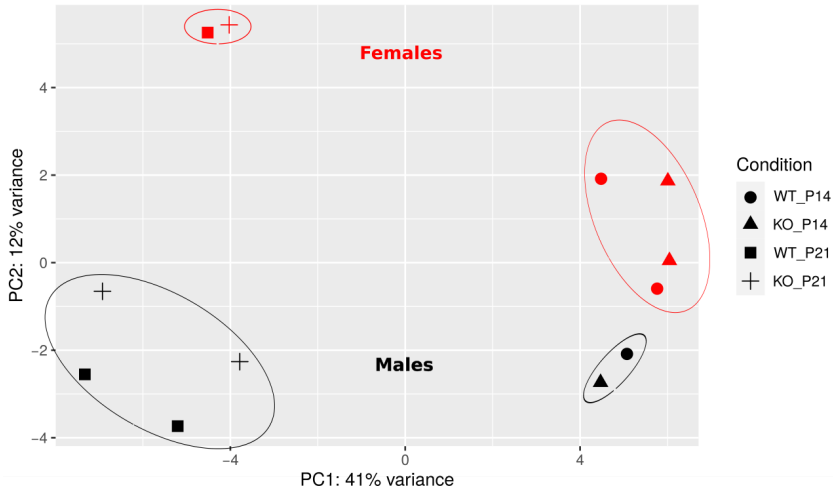


Figure IV.8. Principal Component Analysis (PCA) of mice hippocampus.

Next, we used Independent Hypothesis Weighting (Ignatiadis et al. 2016) as well as the Log fold change (LFC) shrinkage (Zhu, Ibrahim, and Love 2018) in order to perform an initial analysis of differentially expressed genes between the stages and between the genotypes. Figure IV.9 describes the results of LFC shrinkage for better visualization and ranking of data. As expected, many significantly differentially regulated genes were found between stages within the same genotype (WT_PD14 vs PD21: 1602 genes, KO_PD14 vs PD21: 1554 genes; Figure IV.9 A and B respectively). Next, we searched for differentially expressed genes between the genotypes at particular developmental stages. Very few significantly differentially expressed genes (adjusted $p < 0.05$) were found: 14 genes at PD14 (Figure IV.9 C), and 20 genes at PD21 (Figure IV.9 D).

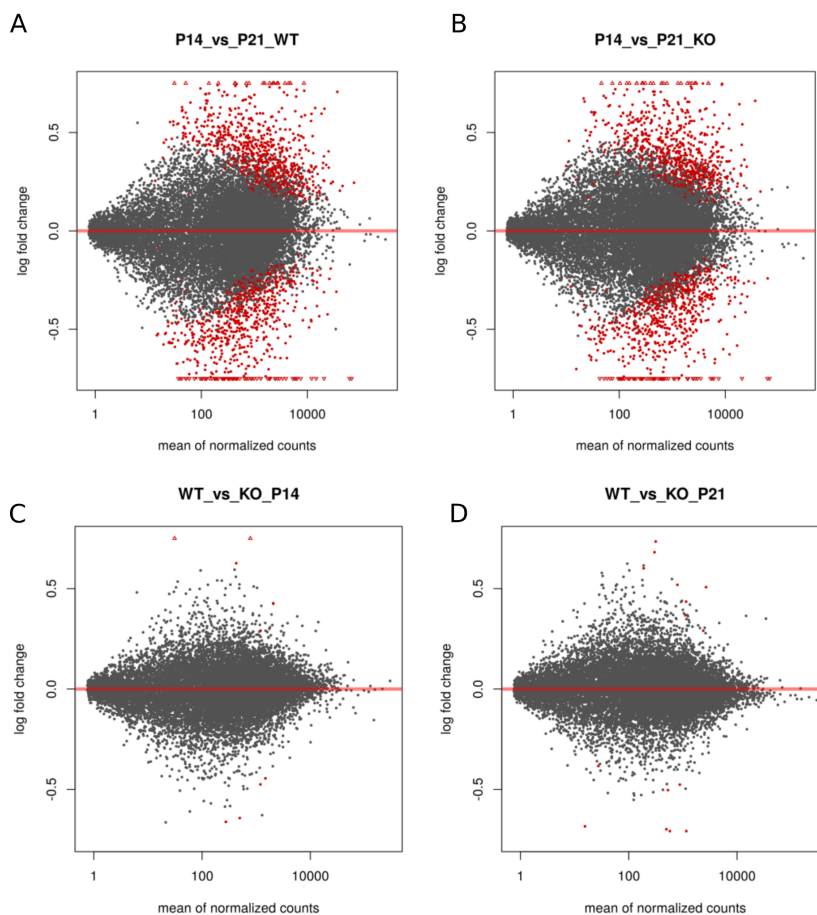


Figure IV.9. MA-plot of differentially expressed genes using shrunken log₂ fold changes. Differentially expressed genes were analyzed while comparing A) WT mice between the developmental stages PD14 and PD21, B) KO mice between the developmental stages PD14 and PD21, C) WT and KO mice at PD14, and D) WT and KO mice at PD21. Points are coloured red if the adjusted p-value is less than 0.05.

The differentially expressed genes at PD21 were next submitted for enrichment analysis using Enrichr (Chen et al., 2013; Kuleshov et al., 2016, Xie et al. 2021). Interestingly, genes encoding proteins with FH2 actin-binding domains were the most enriched category among Pfam InterPro domains (Figure IV.10. A). Analysis of Gene

Ontology terms related to Biological Processes further revealed the Wnt signalling pathway, mainly planar cell polarity pathway to be the most significantly enriched term (Figure IV.10 B).

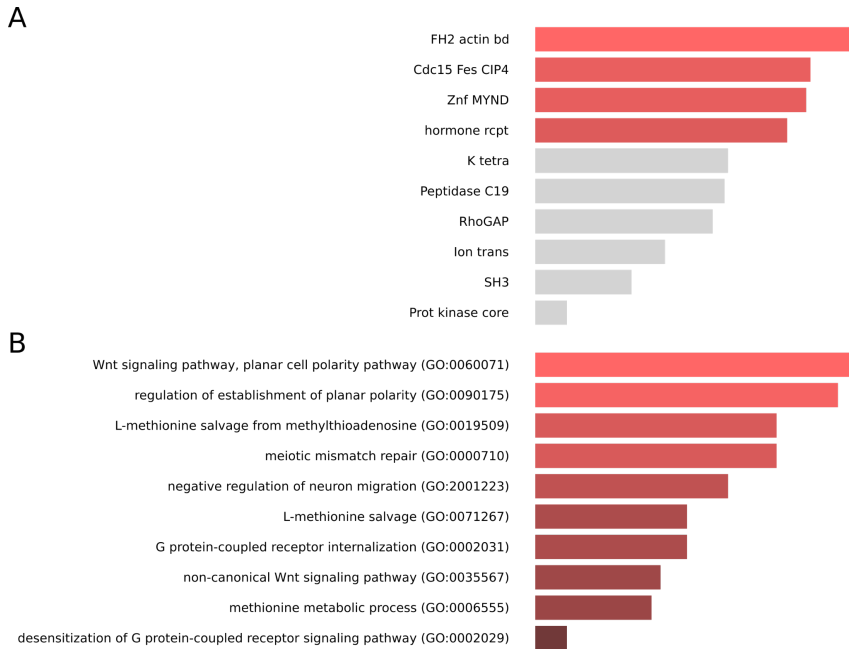


Figure IV.10. Gene set enrichment analysis between WT and KO mice hippocampi from PD21 using Enrichr. A) Pfam InterPro Domains enrichment analysis. B) GO Biological Process enrichment analysis. Analysis performed using Enrichr (<https://maayanlab.cloud/Enrichr/>).

5. Neurological alterations upon Daam1 microexon KO in adult mice

Proper locomotor behaviour and cognitive performance during adulthood are crucial aspects essential for normal functioning. Impairments during the early neuronal development may not always translate directly to the performance during adulthood, since they can be corrected with time. In line with this idea, some developmental differences during the early postnatal stages (PD7 and PD10) described in Chapter 4 were lost during later stages of the development (PD14). Hence, in this chapter, we have decided to analyze the neurological alterations upon Daam1 microexon removal in adult mice. We used 3-5-month-old mice as this is the most commonly considered “adult” age and it is characterized by a high phenotypic stability (Jackson et al., 2017). All experiments have been performed twice independently to ensure reproducibility. Each replicate consisted of 24 animals, where both males and females have been analyzed to avoid potential, commonly omitted sex biases (Will et al., 2017; Zucker and Beery, 2010). Each experimental group thus contained an equal number of WT and KO mice (i.e. 6 WT males and 6 KO males), and pairs of siblings of the same sex but different genotype were used in most cases.

5.1. Activity, motor coordination and balance

Some experiments described in Chapter 4 hinted at impaired neuromotor behaviours during early developmental stages. In this subchapter, we investigated plausible impairments of strength, balance, motor coordination and generally activity upon microexon removal in adults. Deficits in motor function have been well documented in many neuropsychiatric disorders, including autism spectrum disorder (ASD), depression, schizophrenia and many others (Eltokhi et al., 2021). In some cases, specific features are considered landmarks of the illness and its severity. As these motor phenotypes vary between different neuropsychiatric disorders, we have decided to use multiple complementary experiments to have a full overview of possible phenotypes during adulthood.

a) Grip Strength

First, we have evaluated the muscle strength of our mice. This was done by direct measurement of the force developed using a dynamometer in the grip force test (Figure V.1A, left panel). Focusing on forelimb strength, significant differences between sexes and genotypes were observed while analyzing maximal peak force developed (Figure V.1 right panel, the effect of sex $p = 0.010$; effect of genotype, $p = 0.036$, ANOVA). This further supports the findings from early development where heterozygous mice performed better during the forelimb suspension test.

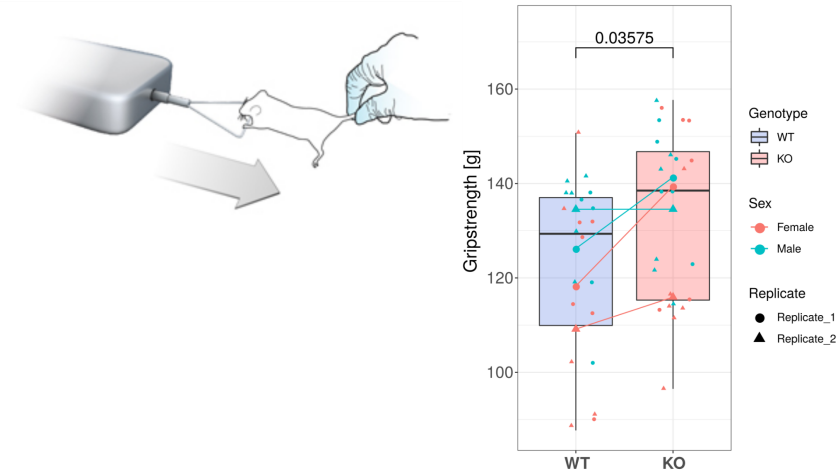


Figure V.1. Daam1 microexon removal increases forelimb grip strength during adulthood. Left panel - schematic representation of the experiment performed. Adapted from www.myologica.com. Right panel - analysis of the maximal peak force developed during the experiment. Grip strength was measured by a grip-strength meter (Bio-GS3 Grip-Test, Bioseb Vitrolles, France).

b) Beam Balance

The beam balance test (otherwise known as the beam walking assay) was used to investigate motor coordination and balance. We analyzed the latency to reach the end of the beam (considered as an escape route), as well as granted points depending on the mouse's performance. Our scoring system was based on an easy and intuitive assessment of mouse performance, namely:

3 points - mouse reached the beam edge,

2 points - mouse did not reach the edge, yet it moved away from the start boundary (beam middle),

1 point - mouse did not move from the start point,

0 points - mouse fell down from the beam.

Figure V.2A (upper panel) shows a schematic representation of the experiment performed. Interestingly, our first observation focused on an unexpected slipping behaviour that was observed mainly in female KO mice. This impaired “equilibrium” for females was observed together with near-complete falling and hanging underneath the beam. Figure V.2A describes the phenotype observed in WT (upper panel) and KO (lower panel) female mice. We have observed that the number of paw slips of our KO mice is significantly higher in females (Figure V.2B; males: $p = 0.31$, females: $p = 0.025$, student's t-test) and when considering replicates and sex differences between WTs and KOs ($p = 0.010$, ANOVA). No significant point-based score differences were observed as the majority of the animals reached the escape route without the genotype specificity (Figure V.2C, males $p = 0.38$, females $p = 0.62$,

student's t-test). As a result of the increased slipping behavior, female KOs showed a non-significant trend to taking longer to reach the periphery of the beam (Figure V.2D, n.s., males $p = 0.38$, females $p = 0.62$, student's t-test).

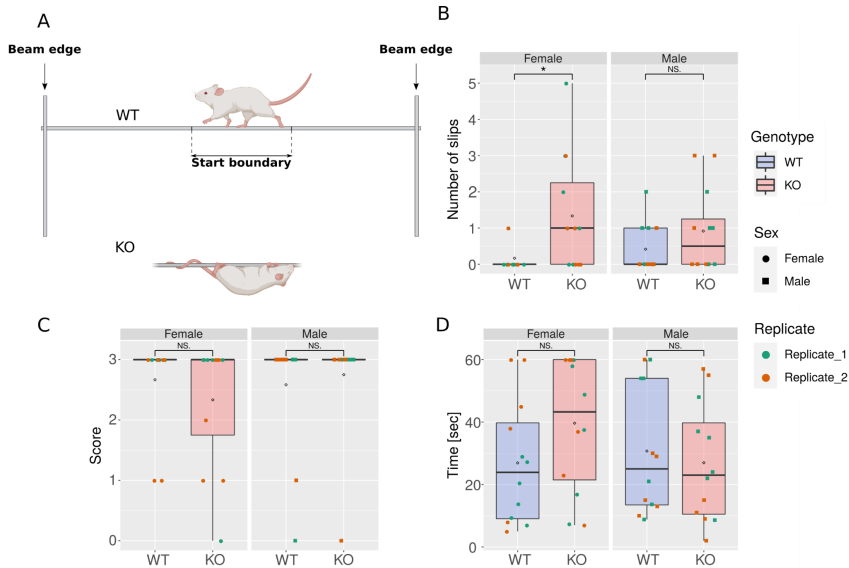


Figure V.2. Daam1 microexon removal impairs the balance of female mice.

A) Schematic representation of the experiment performed created with BioRender.com B) Number of slips from the beam. C) Performance score where: 3 points - mouse reached the beam edge, 2 points - mouse did not reach the edge yet moved away from the start boundary (beam middle), 1 point - mouse did not move from the start point, 0 points - mouse felt down from the beam. D) Performance latency when counted as the time needed to reach the beam edge. Significance codes: * $p \leq 0.05$, ** $p \leq 0.01$, *** $p \leq 0.001$.

c) Rotating Rod (Rotarod)

Motor coordination was also evaluated by the rotating rod test (Rotarod). Schematic representation of the rotarod is described in Figure V.3.A. Three separate sessions of the Rotarod experiment were evaluated, referred to here as the training, coordination and acceleration sessions.

During the training session, mice were exposed to the rotating rod for the first time. Here, the ability to withstand 60 seconds without falling down was evaluated and the number of sessions needed to fulfil the criteria was compared among groups. The KO animals from both sexes performed slightly better in the training session yet did not reach significance (Figure V.3.B).

Next, for the analysis of motor coordination, the latency to fall was recorded during several sessions, where the speed was kept constant at 7, 10, 14, 24 and 34 rpm, with a maximum residence time of 2 min. No significant differences were observed indicating no genotype-dependent effect (Figure V.3.C).

Finally, we subjected the animals to an acceleration cycle in which the speed of the roller goes automatically from 4 to 40 rpm in 1 min. We observed no phenotype in both the acceleration time and the acceleration speed reached (Figure V.3.D and E respectively).

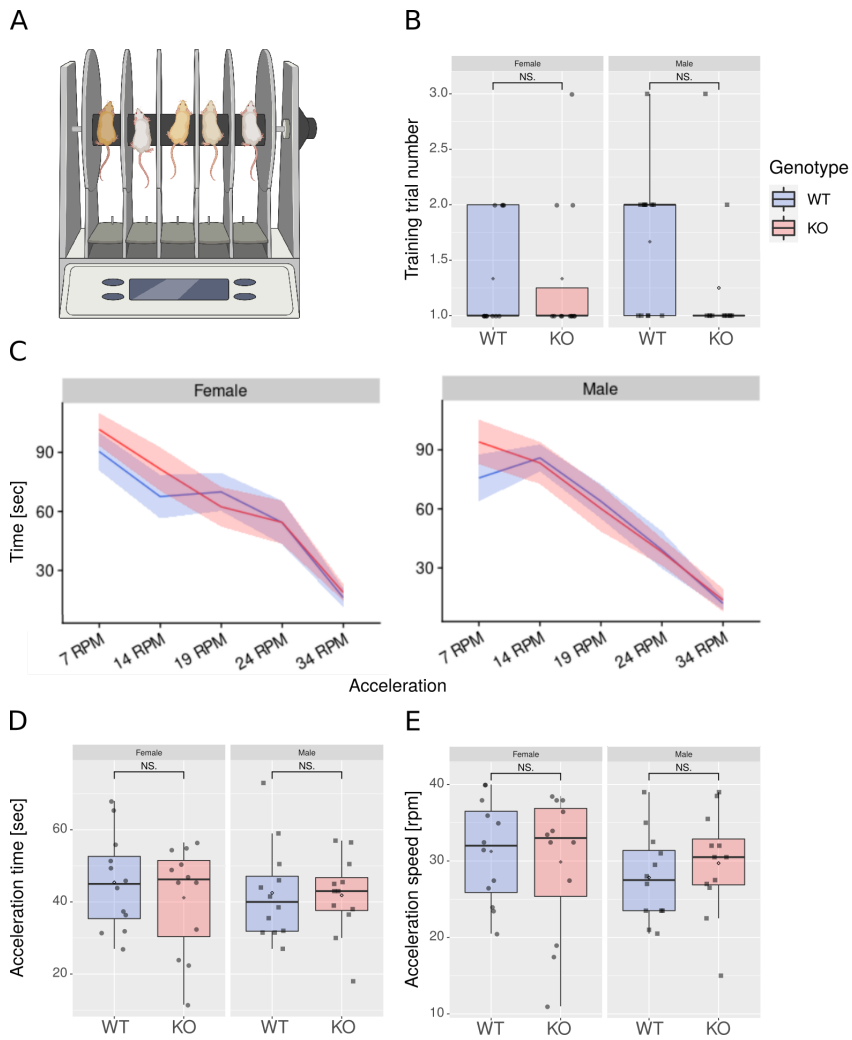


Figure V.3. Rotarod test. A) Schematic representation of the Rotarod test created with BioRender.com B) Training session described as the number of trials needed to perform 1 min run. C) Coordination session with constant speed. Two trials per animal were performed and time compared. Next, acceleration cycle was performed twice and the latency to fall was recorded as acceleration D) time and E) speed.

d) Open Cage

The habituation step from the Novel Object Recognition experiment (see next subchapter Learning and Memory formation) was used to test the adaptation to the open field, and we refer to it here as the “open cage experiment”. In this experiment, mice were exposed to a novel environment for 5 minutes, where they were allowed to explore freely. Here, anxiety-related behaviours can be analyzed by comparing the time spent in the centre of the arena and its periphery. The cage was divided *in silico* into centre and outer region and resting time, latency to enter the centre and velocity of mice were analyzed. Sex-dependent differences were observed between WT and KO animals, with only males showing significant differences.

Microexon-lacking mice were characterized by a decreased resting time in the central zone, reaching significant levels for males (Figure V.4B, genotype effect, males $p = 0.036$, females = 0.89, student's t-test). Additionally, we observed significantly higher mean speed in the centre region of the cage, especially in males (Figure V.4C, genotype effect, males $p = 0.038$, females $p = 0.74$, student's t-test). This phenotype might be a hallmark of anxiety, as stressed animals tend to avoid open spaces. Moreover, to further test this hypothesis we analyzed the thigmotaxis, usually defined as the time that an animal remains close to the walls. Parallel index in centre is significantly higher in male KOs compared to male WTs (Figure V.4D, genotype effect, males $p = 0.016$, females $p = 0.95$, student's t-test), while in the outer region it showed a

near-significant values (Figure V.4E, genotype effect, males $p = 0.086$, females $p = 0.14$, student's t-test). Due to observed phenotypes, we decided to perform two additional experiments specifically tailored for anxiety assessment. These experiments, namely the actimeter and the elevated plus-maze will be discussed next.

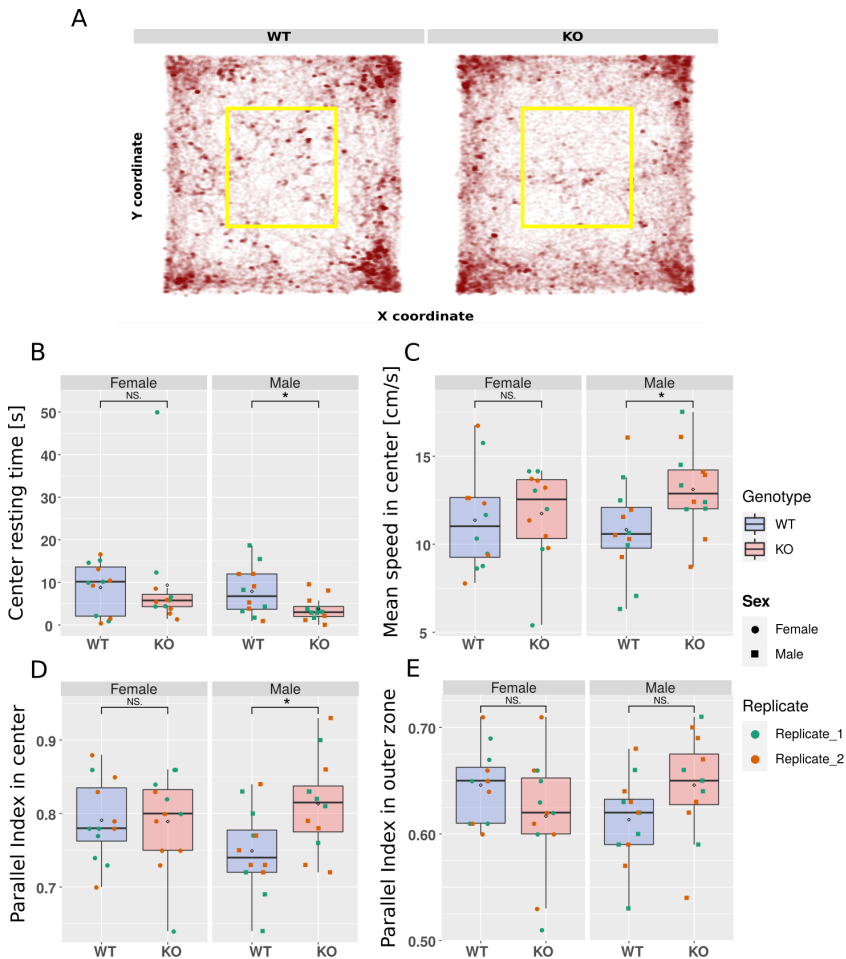


Figure V.4. Open cage test. A) Scheme of the arena and its central zone (yellow) with trajectories of the male wild type and microexon knockout animals from experimental replicate 1. B) Resting time [sec] in the central zone. C) Mean speed in the central zone [cm/sec]. D) Parallel index calculated

in the central zone of the open cage. D) Parallel index calculated in the outer zone of the open cage. Significance codes: * $p \leq 0.05$, ** $p \leq 0.01$, *** $p \leq 0.001$.

e) Actimeter

The actimeter is used to study spontaneous locomotor activity. The great advantage of this equipment is the ability to analyze animal behaviour for longer periods of time including night and day activity analysis. Here, similarly to the open cage test above, a mouse was exposed to a semi-novel environment where it is allowed to explore freely. A semi-novel environment is characterized by the addition of familiar wood shavings at the apparatus base. Additionally, each mouse has sufficient amounts of water and food for a long experiment. 23-hour periods of animal activity were analyzed in three separate phases: habituation (1st hour), night (12h with the lights off), and the total 23h period. No global changes were seen in locomotor activity in the 23h period, including activity, velocity, distance travelled, and resting time. Figure V.5 describes the average distance travelled by unit of time, separated by sex (upper panel, Female (F) and Male (M)). The lower panel depicts the associated statistical test for each corresponding time window based on randomizations (see Methods for details). Together, this result suggests no gross effect on the locomotor activity, nor strong anxiety-like differences between WT and KO animals analyzed.

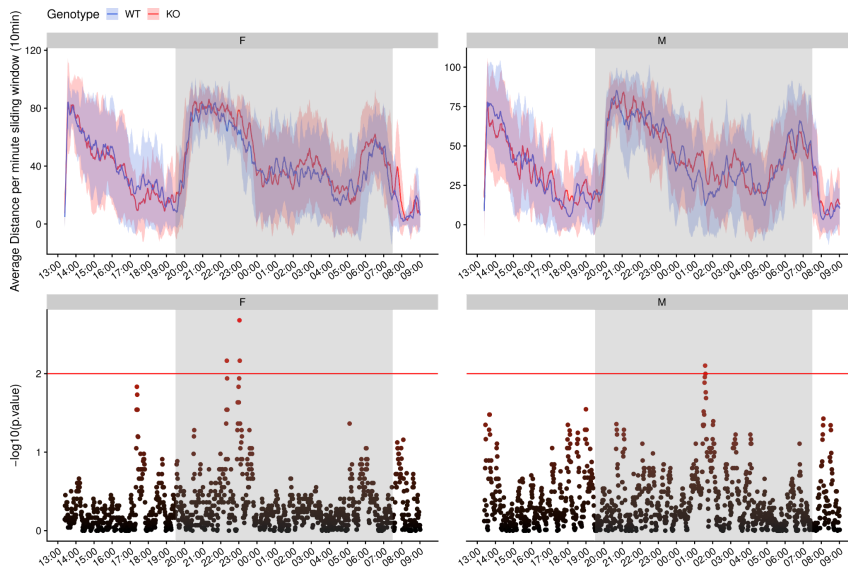


Figure V.5. Spontaneous locomotor activity of wild type and microexon knockout mice in the 23h time period. A) Plot A describes the average distance travelled per genotype in 10 minutes (sliding window 1 min). B) \log_{10} p-value corresponding to A). The horizontal red line describes the significance threshold, gray area marks light off/dark phase of the night cycle. X-axis describes time and corresponds to the 24-hour notation in the form hh: mm

Upon closer inspection of the data, I observed a distinct pattern during the night period of the experiment (Figure V.6.). During the night, the microexon-lacking animals show consistently higher distance travelled, stereotaxis and mean velocity, suggesting higher activity during the night. Unfortunately, mentioned phenotypes did not reach significance levels yet their contribution should be further investigated.

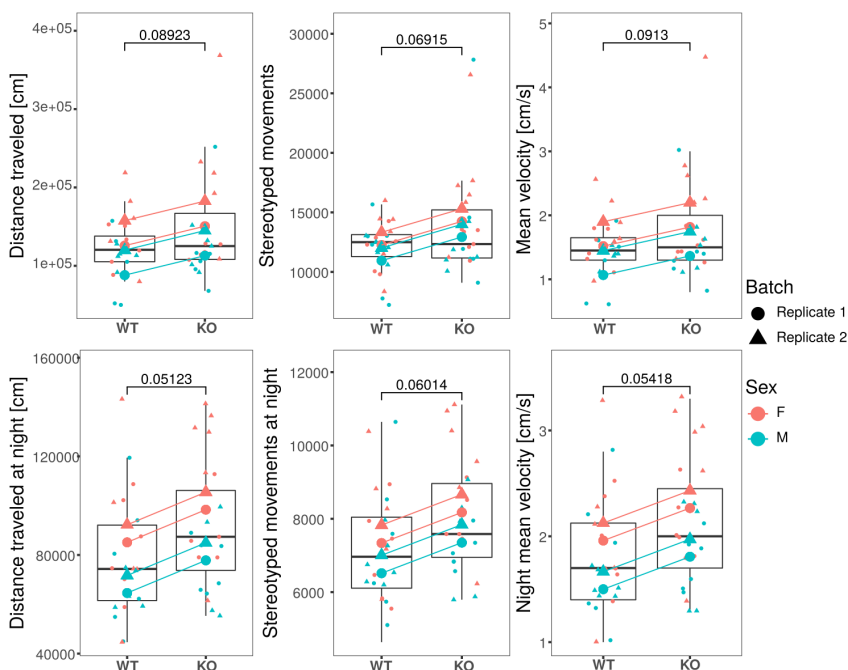


Figure V.6. Spontaneous locomotor activity of wild type and microexon knockout mice in the 23h time period and during the 12h night period. Analysis of the A) Distance travelled, B) Stereotaxis, and the C) Mean velocity during the whole experiment period (23h). Analysis of the D) Distance travelled, E) Stereotaxis, and the F) Mean velocity during the lights off, night period of the experiment performed (12 h). ANOVA

f) Elevated Plus Maze

Elevated Plus Maze is a test that allows evaluating the activity in an aversive environment and it is specifically aimed to study anxiety-related behaviour (Walf and Frye, 2007). The apparatus stands 40 cm above the ground and consists of four arms, two closed (high walls) and two opened forming a “+” shape (Figure V.7 A). Rodents are naturally afraid of open and elevated areas, so they have an aversion towards open arms. Multiple parameters were analyzed, which suggest anxiety-like behaviour in females. Firstly,

the number of entries into the open end zone was significantly lower in KO females (genotype effect, males $p = 0.44$, females $p = 0.046$, student's t-test). Additionally, 1st latency of entering the centre of the maze also showed significant differences (genotype effect, males $p = 0.42$, females $p = 0.023$, student's t-test). Lastly, the minimal speed in the open arms was significantly higher for female mice (genotype effect, males $p = 0.55$, females $p = 0.043$, student's t-test).

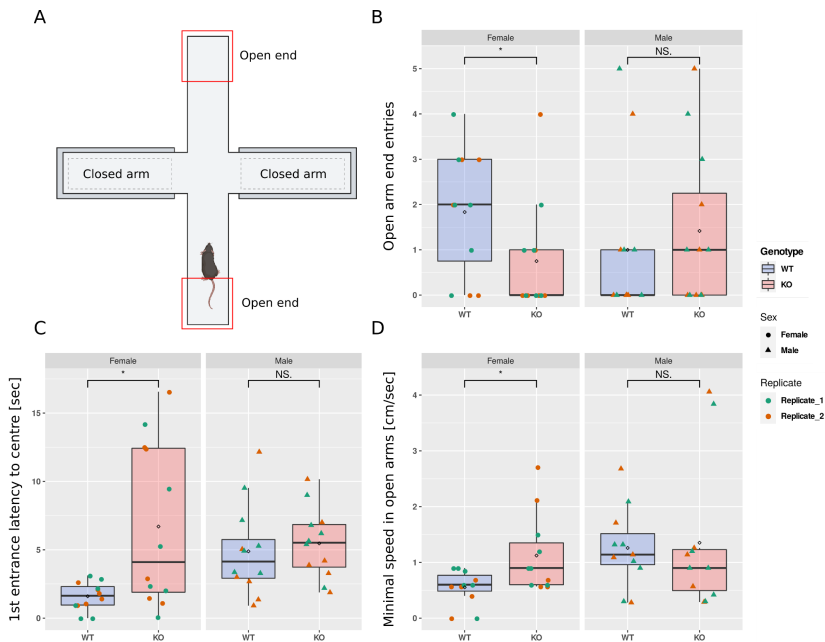


Figure V.7. Anxiety analysis using the Plus maze test.

A) Schematic representation of the experiment performed. A red rectangle describes the open arm end. Figure created with BioRender.com. B) The number of open arms end entries per animal. C) Latency for the entrance to the central zone of the plus-maze measured in the unit of time. D) Minimal speed developed in the open arms [cm/sec]. Significance codes: * $p \leq 0.05$, ** $p \leq 0.01$, *** $p \leq 0.001$.

5.2. Learning and memory formation

The neurobehavioural analyses described above revealed pre-weaning developmental alterations upon microexon KO and specific motor impairments in adults. However, our results also suggest higher neuronal activity in the dentate gyrus, the sub-region of the hippocampus known to play a critical role in learning and memory. Therefore, we decided to investigate a possible involvement of the microexon of *Daam1* in cognition. First, we performed a commonly used hippocampal-dependent task, called novel object recognition (NOR). Second, we performed the Morris water maze (MWM) to address the possible changes in the spatial memory upon microexon removal.

a) Novel Object Recognition (NOR)

We assessed the memory retrieval capabilities of our model, using a well-validated novel object recognition (NOR) task (Leger et al., 2013; Lueptow, 2017). This experiment is easy to perform and does not require additional training sessions, which makes it one of the most widely used memory tests in rodents. Moreover, this test depends directly on the PFC and Hippocampal circuit, which is a crucial system responsible for cognitive processing (Warburton and Brown, 2015, Helfrich and Knight, 2016). The experiment consists of 3 sessions with habituation, familiarization and discrimination (length of 5 min, 10 min, and 5 min, respectively), separated by 24h intervals, a time frame commonly used to evaluate long-term memory in rodents (Figure V.8).

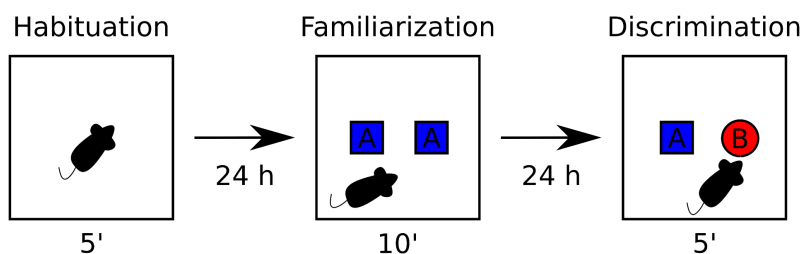


Figure V.8. Schematic representation of the Novel Object Recognition (NOR) experiment performed. The experiment consists of 3 sessions habituation, familiarization and discrimination (length of 5 min, 10 min, and 5 min accordingly). Each stage was separated by 24 h.

Habituation consists in the exposure of the animal to the empty cage, so it becomes used to the new environment. Next, during the familiarization phase animals can explore freely two identical objects, located in the centre of the box. Twenty-four hours later, a discrimination phase was performed where mice were exposed to one familiar and one novel object (pattern and colour changed). Discrimination is based on the innate exploratory behaviour of a WT animal to explore a novel object. Here, in order to be able to recognize the exchanged, novel object, the animal needs to utilize its recognition memory to differentiate a familiar object from a novel one.

Exploration was defined as object sniffing or touching with the nose, while climbing, running around or just sitting on the object was not recorded as exploration (Leger et al., 2013; Lueptow, 2017). No significant differences were observed between WT and KO mice in the total exploration time (neither in the familiarization nor in the discrimination stage; Figure V.9 A and C respectively,

Familiarization exploration time: female $p=0.67$, male $p=0.84$;
Discrimination exploration time: female $p=0.35$, male $p=0.24$;
Wilcoxon rank-sum test). Additionally, we analyzed object climb
delay as the measurement of decisiveness and certainty. No
significant differences were observed during the familiarization
phase (Figure V.9B, female $p=0.19$, male $p=0.6$; Wilcoxon
rank-sum test), but females KO mice had a significantly higher
climb delay compared to female WT mice in the discrimination
phase (Figure V.9 D, females $p =0.024$, WT $n=8$ vs. KO $n= 7$ mice;
males $p =0.48$, WT $n=11$ vs. KO $n= 9$ mice; Wilcoxon rank-sum
test). Next, the recognition memory was assessed using the d2
discrimination index ($(\text{Novel Object Exploration Time} - \text{Familiar}$
 $\text{Object Exploration Time}) / \text{Total Exploration Time}$). As expected,
during the discrimination phase WT mice preferentially explored
the novel object (Figure V.9E). On the other hand, KO mice
explored the novel object significantly less, exhibiting impaired
performance relative to wild type mice in both females and males
(Figure V.9E, females $p= 0.007$, males $p= 0.007$; Wilcoxon
rank-sum test). This impaired performance indicates recognition
memory deficits or neophobia upon Daam1 microexon removal.

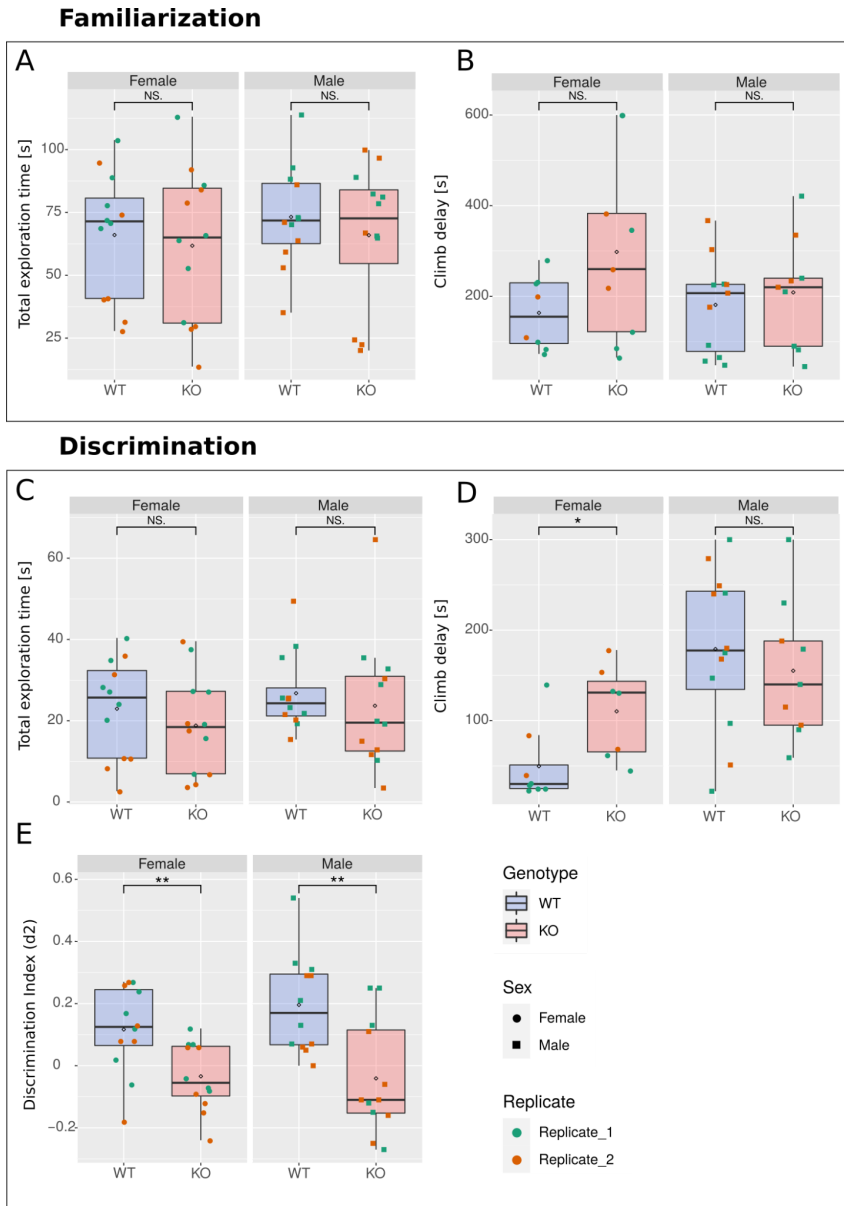


Figure V.9. Daam1 microexon removal causes recognition learning impairments in adult mice. Familiarization: A) Analysis of the total exploration time defined as object sniffing and B) object climb delay during the NOR familiarization phase. **Discrimination:** C) Analysis of the total exploration time defined as object sniffing, D) object climb delay, as well as the Discrimination index (d2) quantified during the NOR discrimination phase. Discrimination index (d2) was quantified as the (*Novel Object Exploration*

Time - Familiar Object Exploration Time) / Total Exploration Time).
Significance codes: * $0.01 \leq p < 0.05$, ** $0.001 \leq p < 0.01$, *** $p < 0.001$.

b) Morris Water Maze (MWM)

Lastly, spatial memory was assessed using a modification of the Morris water maze (MWM) task, summarized in Figure V.10A. The aim of the experiment is to analyze the ability of an animal to navigate around the perimeter in order to find a hidden escape route, a submerged platform. During the acquisition phase, the animal has to create a “memory map” of the place using distal cues that are provided as reference points. Spatial learning is assessed by the ability of an animal to learn and then find the platform in subsequent experiments (Vorhees and Williams, 2006). Both KO and WT mice showed a progressive reduction in the escape latency time. No significant differences were recorded between the latencies for WT and KO females (Figure V.10B upper panel). However, the ability of KO males to find the hidden platform was reduced in comparison to WTs. Between days 4 and 6, the KO males did not show any improvement in finding the hidden platform and did not reach the same execution levels (Figure V.10B lower panel, fourth session $p = 0.002$, fifth session $p = 0.068$, sixth session $p = 0.042$, ANOVA).

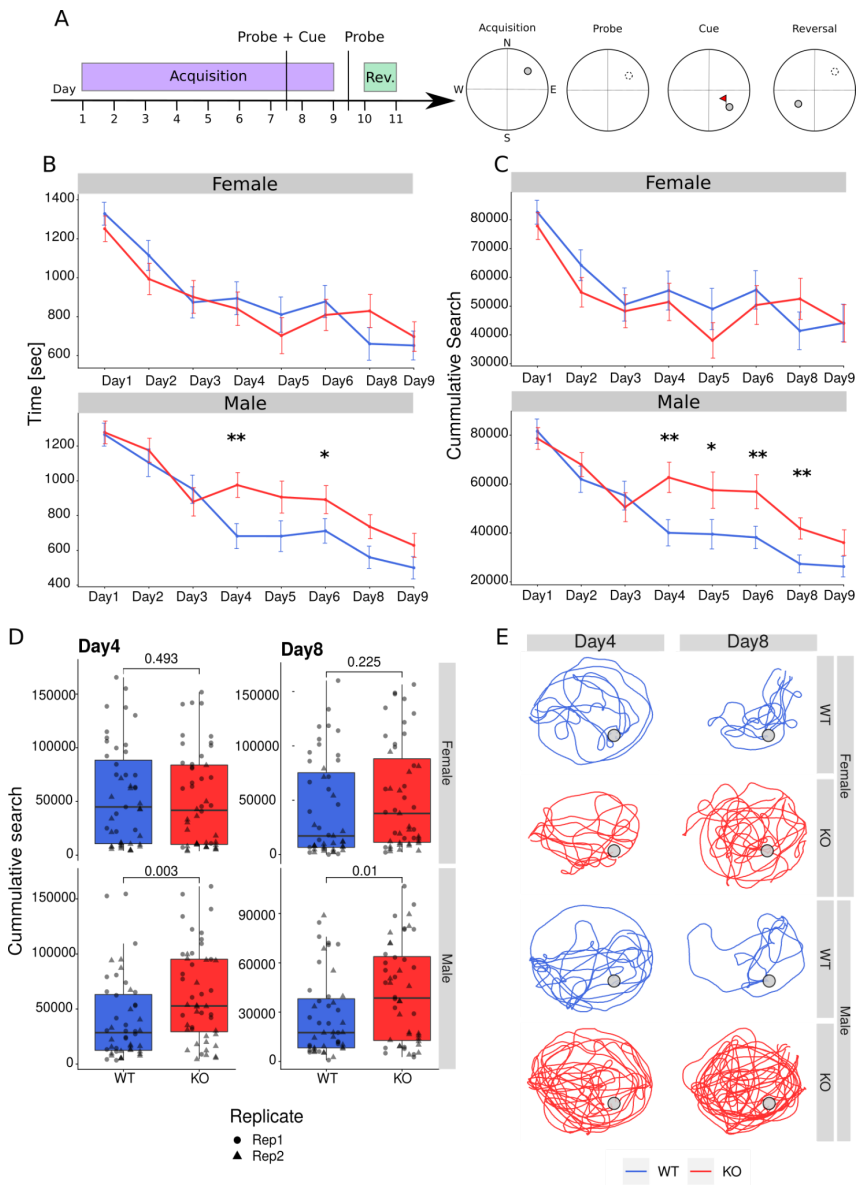


Figure V.10. Daam1 microexon removal causes spatial learning impairments in adult male mice. A) A schematic representation of the Morris water maze protocol was performed. Mice were trained for 8 days to locate a hidden platform. A probe trial was performed on the seventh and tenth day when the platform was removed. The hidden platform was moved to the opposite quadrant during reversal training. A flag was placed on the hidden platform during the visible training phase on day 7 and day 10. B) Latency to find the escape route (hidden platform) in the unit of time during the

acquisition phase for females (upper panel) and males (lower panel). C) Cumulative index during the acquisition phase for females (upper panel) and males (lower panel). D) Quantification of the cumulative index during the 4th and 8th day of the acquisition phase. E) Representative trajectories of control and microexon lacking mice during the acquisition phase of the Morris water maze. Significance codes: * $p \leq 0.05$, ** $p \leq 0.01$, *** $p \leq 0.001$.

In order to determine if other factors, unrelated to learning, impact the performance of our mice, we have decided to add visually dependent cued trials. Here the platform localization was marked additionally by a cue (flag) and the performance was assessed. No significant differences between the genotypes were observed, as nearly all animals performed the visually cued sessions. Afterwards, two additional acquisition days were performed to assess improvement. During day 8 (24h after the last cue session), the overall performance improved, yet the KO males remained worse at performing the task (Figure V.10B lower panel, eighth session $p = 0.058$, ninth session $p = 0.155$, ANOVA).

Additionally, we have decided to calculate the cumulative search error (Tomás Pereira and Burwell, 2015), derived from the proximity measures suggested by Gallagher et al., 1993. These measures are developed specifically in order to better recognize the search strategy the rodent employs and is based on the constant assessment of the distances between the animal and the localization of the platform. With this analysis, we further confirmed the impaired spatial memory specific to KO males (Figure V.10 C; females: fourth day $p = 0.493$, fifth day $p = 0.173$, sixth day $p = 0.385$, eight-day $p = 0.225$, ninth day $p = 0.983$; males: fourth day $p = 0.003$, fifth day $p = 0.044$, sixth day $p = 0.005$, eight-day $p = 0.01$,

ninth day $p=0.122$; ANOVA). Statistical summary of Day 4 and Day 8 performance, and example trajectories can be found in Figure V.10 D and Figure V.10 E respectively.

Probe session (platform removal)

To test if the mice indeed learned the spatial location of the escape route (platform), the probe trial was conducted in which the platform was removed and the animal behaviour analyzed. The probe trials were performed twice, after the cued session (Day 7) and after the last day of the acquisition (Day 10). Figure V.11A describes the representative trajectories of the WT and KO mice separated by sex during the removal phase Day10. The latency to first cross the position where the platform was previously hidden was similar in both genotypes (Figure V.11 B, Day 7, females $p = 0.552$, males $p=0.936$; Day 10, females $p = 0.857$, males $p=0.368$; ANOVA). Similarly, the number of crosses was similar between genotypes (Figure V.11 C, Day 7, females $p = 0.906$, males $p=0.472$; Day 10, females $p = 0.195$, males $p=0.397$; ANOVA).

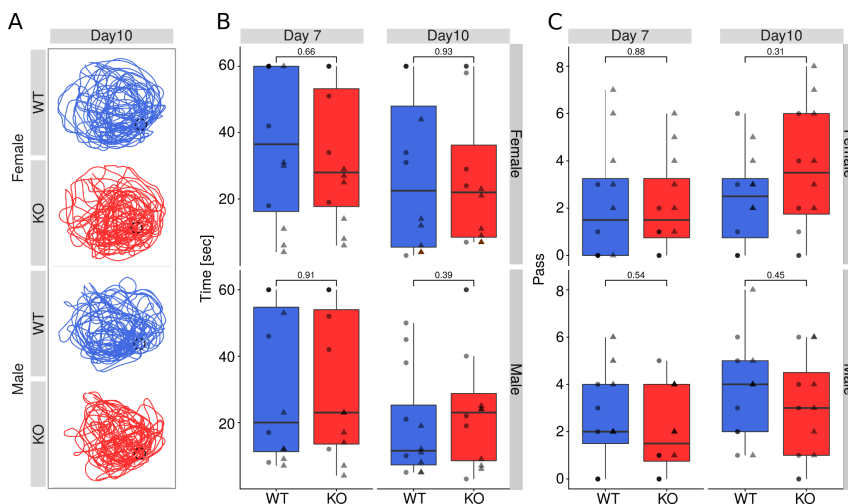


Figure V.11. Removal phase of the Morris water maze. A) Representative trajectories of control and microexon lacking mice during the removal phase of the Morris water maze. B) Analysis of the latency to first pass through the old escape route (hidden platform) localization in the unit of time. C) Number of passes through the old escape route (hidden platform) localization.

Reversal session

Lastly, we performed two days of the reversal sessions. Here, the submerged escape platform is reintroduced to the tank at the new location (Figure V.10.A). This test allows to assess the re-learning ability, which enhances the detection of potential spatial learning impairments. Figure V.12 A describes the representative trajectories of WT and KO mice separated by sex during the reversal phase Day11. No significant differences between WT and KO were observed in both sexes (Figure V.12 B, females $p = 0.88$, males $p=0.64$; ANOVA).

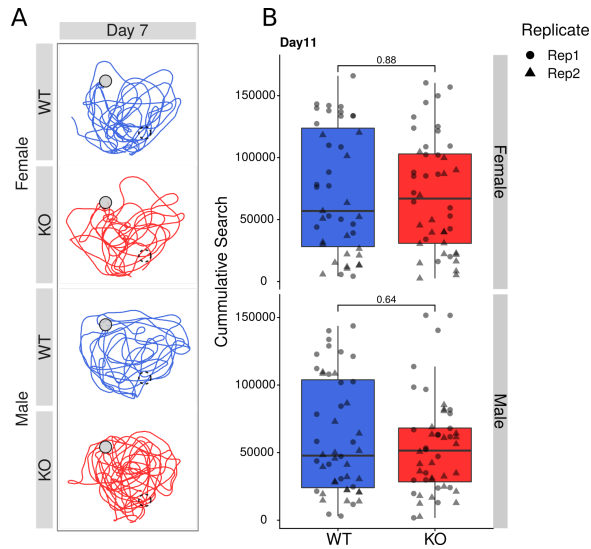


Figure V.12. Reversal phase of the Morris water maze. A) Representative trajectories of control and microexon lacking mice during the reversal phase of the Morris water maze. B) Analysis of the cumulative index during the Day 11 of the reversal phase for females (upper panel) and males (lower panel).

Discussion

In this thesis, we show that the removal of Daam1 microexon directly impacts actin dynamics, resulting in higher activity of glutamatergic neurons and motor and learning deficits in mutant mice. Our results provide the first evidence for the role of the alternative splicing-driven modification of Daam1, which might be associated with human neurological impairments like bipolar disorder.

Our results show that DAAM1 microexon causes insertion of ten amino acids in the disordered region of the FH2 domain. This insertion does not cause extensive changes in the general domain structure but substantially elongates its linker region. Elongation of the linker does not impact the homodimerization capabilities of the domain but impairs its actin-binding abilities. Our biochemical data suggest robust differences in the mode of action between the two splice variants of purified DAAM1 fragments. The microexon-lacking variant (-MIC) is more effective in its actin-binding capabilities, causing faster nucleation of actin fibers and higher actin-bundling. The strong binding of the -MIC homodimer abolished efficient actin elongation presented by the microexon containing variant (+MIC). The +MIC variant also causes actin branching, initiating the formation of higher-order actin networks. These observations can be explained by structural differences between the isoforms of DAAM1. A shorter linker region translates to short distances between the monomers of the homodimer. The short distance causes tighter F-actin filament

binding, lower flexibility of the domain, and lower processivity of the -MIC variant. Previous research addressed the problem of DAAM1's weak actin polymerization activity (Lu et al., 2007), where Yamashita et al. 2007 found the linker length to be directly responsible for it. Our results support that claim and expand it, by providing the optical explanation for the changes in actin dynamics in time. Moreover, we addressed the linker expansion as a naturally occurring AS-driven event, which is unique among formins. Nevertheless, further biochemical and structural studies are required to capture the conformational differences essential to explain the actin assembly process of both splice variants. One possibility would be application of Electron Microscopy, allowing to observe all possible conformations of FH2 domain on actin fiber.

Interestingly, linker elongation by microexon inclusion increased the complexity of actin-based structures. These structural differences could relate to the neuronal-specific character of this splice-variant. Neurons are characterized by high morphological complexity, enabling the formation of networks that are essential for higher cognitive functions. Many AS events probably evolved around the time of emergence of the vertebrate lineage increasing neural transcriptome complexity (e.g. Torres-Méndez et al., 2019). One hypothesis is that the introduction of certain AS exons (including the microexon of DAAM1), greatly expanded the proteome, probably enhancing the functional and morphological complexity of the neural lineages. Previous studies performed in fruit fly (Matusek et al., 2008; Szikora et al., 2017), planaria (Beane et al., 2012), chicken (Avilés and Stoeckli, 2016), zebrafish

(Colombo et al., 2013), mouse (Kawabata Galbraith et al., 2018) and human (van der Lee et al., 2019; Mollink et al., 2019) highlight DAAM1 as a relevant player in neuronal morphology, and consecutively brain connectivity.

Surprisingly, our data show no extensive effect on early neuronal differentiation with no considerable differences in the filopodia formation, neurite, or growth cone morphology. The reason for this might be trinal: 1) the cellular system or the developmental stage chosen prevented detection of morphological differences, 2) the microexon removal causes molecular changes yet a compensation occurs, preventing the morphological impairments from happening at measurable levels, and 3) the microexon of Daam1 does not contribute notably to early neuronal morphology. First, the neuronal differentiation system chosen was already used in previous research, proving impaired neuritogenesis upon protrudin microexon removal (Ohnishi et al., 2017). Additionally, Daam1 microexon seems to be included at the mRNA level already at DIV0, four hours before our morphology analysis. This time should be enough for transcript translation and subsequent protein functioning, contributing to morphological changes (Koltun et al., 2020). Secondly, cellular differentiation is a temporal event during which a cell has enough time to adjust its gene expression and the proteome, averting sizable morphological defects. Indeed, Daam1 is one of the fifteen genes encoding formin proteins, suggesting that a possible compensation mechanism can likely occur. Moreover, calcium imaging experiments performed show no calcium flux differences at the early stages of neuronal differentiation, further implying a minor

role for this microexon at these stages. Ultimately, the possibility of microexon lack-of-function during early neuronal differentiation is pending and should be a subject of complementary investigations.

On the other hand, calcium imaging experiments performed show higher calcium influx in KO neurons starting at DIV14. Studies show increased electrophysiological properties of ES cell-derived neurons from DIV12 (Bibel et al., 2004), implying a role for Daam1 microexon in synaptic function, rather than early differentiation. Interestingly, blocking the activity of formin proteins using a small molecular inhibitor of formin FH2 domains (SMIFH2) caused increased calcium influx in WT glutamatergic neurons, similar to that observed in the microexon KO cells. These related phenotypes upon microexon KO and SMIFH2 exposure further confirm our *in vitro* observations, where microexon removal impaired efficient F-actin polymerization (Chapter 2, TIRF microscopy). Interestingly, a recent study suggests a leading role of formin-dependent actin assembly in synaptic vesicles (SVs) endocytosis (Soykan et al., 2017). These authors proposed that formin-driven actin filaments are crucial for membrane fission, essential for membrane tension, and sequentially exocytosis. Interestingly the authors observed that SMIFH2 exposure in neurons resulted in robust endocytosis inhibition followed by higher calcium inflow although the molecular mechanism remains elusive.

On the other hand, Latrunculin A (LatA) caused an opposite effect, lowering calcium influx. These effects were stronger in KO than in WT cell lines, indicating that the pre-existing imbalance of the

synaptic actin network has synergistic effects. LatA promotes F-actin depolymerization by sequestering available G-actin monomers (Spector et al., 1999). LatA treatment causes a significant delay in synaptic vesicles recruitment in the Calyx of Held (Sakaba and Neher, 2003), and in the rat hippocampal slices a reduction in the miniature excitatory postsynaptic currents (mEPSCs) (Kim & Lisman 1999). Unfortunately, using pharmacological drugs like the LatA is never straightforward, and neurological systems are complex in their mode of function. Different studies suggest that in hippocampal synapses, LatA treatment promotes neurotransmitter release, increases the frequency of mEPSCs (Morales et al. 2000), and increases the rate of exocytosis (Sankaranarayanan et al. 2003). Collectively, these observations create an opportunity for future studies where the Daam1's microexon role in SV cycling should be evaluated.

We further confirmed the higher neuronal activity of KO neuronal cultures by the immunostaining of Activity-regulated cytoskeleton-associated protein (Arc). Arc is an F-actin interacting protein thought to have a crucial role in long-term synaptic plasticity (Nikolaienko et al., 2018; Park et al., 2008). An increase in the number of cells expressing Arc protein was further confirmed in the hippocampi of KO mice (PD21), presumably a direct consequence of Daam1 microexon removal. Higher Arc-expressing neurons were observed together with accelerated development of KO mice, reflected in higher limb strength and improved cranio-caudal behavior. Interestingly, some of the developmental differences, like limb strength, persisted till adulthood. On the

contrary, differences related to the cranio-caudal development characterized by shorter walk latency at postnatal day 7 (PD7) in KO pups, were followed by a delay in latency at PD10 and no significant differences at PD14. Unfortunately, gene perturbations that impair dynamic processes such as development are heterogeneous, possibly involving compensation mechanisms intended to self-rescue the system. One of many examples would be the *Daam1* gene KO itself, which showed variable lethality from E10.5 till E16.5 due to placental development defects (Nakaya et al., 2020). We did not observe viability problems upon microexon removal, but a detailed analysis of embryonic lethality is pending.

Misregulated axon guidance or impaired neuronal migration might be one additional explanation for the developmental differences observed. Hippocampal RNA-seq data highlights a few differentially expressed genes involved in neuronal migration (*Srgap2* (Guerrier et al., 2009)), or neurite outgrowth (*Cntn4* (Osterhout et al., 2015)). Additionally, Gene Ontology analysis highlights the Wnt signaling pathway as the most significantly enriched term. Multiple publications describe the process of *Daam1* activation where its autoinhibition is released upon interaction with Dishevelled, a key player of Wnt (Gao and Chen, 2010; Liu et al., 2008). Wnt signaling is essential for many aspects of an axon, dendrite, and synapse development, consecutively impacting memory-related processes (He et al., 2018). One possibility that could explain the increased strength of KO mice could be related to the Wnt-Frizzled interaction, shown to be crucial in the formation of neuromuscular junctions in *Drosophila*. Our analysis shows that

the microexon of Daam1 is not in proximity to the Dishevelled interacting DAD domain. Nevertheless, RNA-seq results might indicate some role of the microexon ultimately affecting the Wnt pathway, opening a possibility for future studies.

Furthermore, multiple aspects of locomotor and cognitive behavior in adult mice were impaired. Of particular interest are the reduced spatial and recognition memory of microexon KO mice. Impaired synapse functioning, connected with exocytosis delay and/or endocytosis impairments, could explain the learning deficits. Interestingly, RICH2 gene knockout mice exhibit similar phenotypes, with a cFos IEG increase, an anxiety-related phenotype, and neophobia in the novel object test (Sarowar et al., 2016; Grabrucker, 2017). The authors of this work connected these phenotypes with actin polymerization changes, causing altered spine morphology in the amygdala, a probable explanation of the increased fear they observed. Inspired by these discoveries, soon we will perform the spine density and morphology analysis. Hopefully, this will allow us to understand the molecular basis of memory impairments upon microexon KO.

Unfortunately, the authors of the RICH2 study did not report any sex differences, as we have observed. Nevertheless, different behavior between males and females is a common factor in neurobiology studies, which sometimes can be explained by housing condition differences or estrous cycle (Frick and Gresack, 2003; van Goethem et al., 2012). Substantial sex-differences in behavior were in fact observed in a mouse model KO for the master

regulators of microexons *Srrm4* (Quesnel-Vallières et al., 2016), which matched the patterns observed in human children with autism spectrum disorder.

Finally, our bioinformatics analysis of publicly available RNA-seq datasets suggested that the inclusion of DAAM1 microexon might be dysregulated in individuals with bipolar disorder. Bipolar disorder is a complex neuropsychiatric disorder characterized by alternating manic and major depressive episodes that affects more than 1% of the global population (Merikangas et al., 2011). To date, multiple mouse models of bipolar disorder exist, where some of the characteristic features involving, increased hyperactivity, decreased habituation, Wnt pathway alterations, or reduced synaptic plasticity, match our reported phenotypes (Gould and Einat, 2007; Vieta et al., 2018). Although these observations are very promising, a possible role of the *Daam1* microexon in bipolar disorder should be investigated in future studies.

To summarize, we provide evidence that the microexon of *Daam1* is a crucial factor in actin dynamics, essential for proper neuronal function, and its impairments can cause locomotor and cognitive defects.

Conclusions

- 1) The microexon in DAAM1 is an alternative splicing event, characterized by tight neuronal inclusion and evolutionary conservation in vertebrates.
- 2) The microexon inclusion does not impair the general structure of the protein, or the homodimerization capabilities of the FH2 domain, but directly modulates the length of the linker region, essential for homodimer flexibility.
- 3) At the molecular level, microexon inclusion modulates actin dynamics, allowing more efficient F-actin polymerization and branching that further translates to formation of higher-order structures *in vitro*.
- 4) Daam1 microexon does not impair early neuronal morphology and is not essential for differentiation towards glutamatergic neurons *in vitro*.
- 5) Microexon removal enhances the activity of mature glutamatergic neurons *in vitro*.
- 6) Deletion of Daam1 microexon in mice affects males and females differently but is not lethal.
- 7) Deletion of Daam1 microexon impairs proper motor development in early postnatal stages. In adulthood, it causes enhanced forelimb strength, mild hyperactivity, and anxiety-like behaviors.
- 8) Deletion of Daam1 microexon does not result in gross morphological alterations in the hippocampus, but leads to impairments in hippocampal-dependent cognitive processes including memory formation and learning.

Materials and Methods

Protein Structure Retrieval and Modeling

Crystal Structure of human DAAM1 FH2 domain (2z6e.pdb) was used to model the mice Daam1 FH2 domain with and without microexon using Robetta (<http://new.robetta.org/>).

ESC maintenance

129-B13 mouse Embryonic Stem Cells (mESCs) were kindly provided by [Kyung-Min Noh](#) (EMBL Heidelberg, Noh Group). mESC were grown on 0.1% gelatine-coated (Millipore, ES-006-B) plates (Thermo Scientific Nunc Cell-Culture Treated Multidishes, 140675) in ESC media. Gelatine coating was performed for a minimum of 5 minutes before plating the cells. ESC media consisted of: Glasgow's Minimum Essential Medium (GMEM) BHK-21 (Gibco, 21710-025) supplemented with 10% foetal bovine serum (Seralab, A1060013 EU-000-H), Minimum Essential Medium non-essential amino acids solution (Gibco, 11140-050), 1mM L-Glutamine (Gibco, 25030-024), 0.5mM Sodium Pyruvate (Gibco, 11360-070), 0.1mM 2-Mercaptoethanol (Millipore, ES-007-E) and recombinant mouse LIF protein 1000U/ml ESGRO (Millipore, ESG1107). ESCs were routinely dissociated using 1x TrypLE Express Enzyme (Gibco, 12605028), split and plated again after quenching with media and 5min centrifuging at 300g. Long term storage of mESCs was performed by cryopreservation in FBS (Gibco, 10270106) and 10% Dimethyl sulfoxide Hybri-Max (Sigma Aldrich, D2650).

CRISPR/Cas9 gene-editing

mESC Knock Out (KO) cell lines were prepared using the CRISPR-Cas9 system (Ran et al., 2013) with a double guide RNA strategy (Sakuma et al., 2015). Each guide RNA targeted one of the two flanking introns and the closest possible (in regards to the exon) and most efficient gRNAs were selected based on MIT score based on Doench et al. 2016. The best gRNAs pair was chosen after testing six independent gRNAs in all possible combinations and

selecting the best editing efficiency. KO was performed by transfection of 1 μ g of Multiplex CRISPR vector into ESCs with Lipofectamine 2000 (Invitrogen, 11668019). mESCs were plated with ~70% confluency on 100mm dishes at 1000 cells/dish and 10000 cells/dish concentration. Transfection of an empty vector was used as a wild type control. 5 hours after the transfection media was changed to reassure survivability. Consecutively, puromycin selection was performed using a concentration of 1 μ g/ml (Sigma, P8833). Puromycin selection was performed after 24 hours from transfection and lasted 4 days. After the selection cells were hand-picked into the 96-well plates. Individual disaggregated colonies were genotyped. Further, positive KO cells and WT controls were expanded and frozen for long term storage as described before. Positively classified cell lines were karyotyped, KO was further confirmed on mRNA level and cell lines were expanded and cryopreserved.

Karyotyping of ESC lines

ESCs of ~70% confluency were passed to a 6-well plate, and the media was changed the following day. Two hours later 0.2 μ g/ml of KaryoMax Colcemid Solution (Gibco, 15212012) was added to the media. After 1-hour cells were dissociated (TrypLE Express Enzyme (Gibco, 12605028)), washed with DPBS 1x (Gibco, 14190) and sedimented by centrifuging for 3 min at 300 g. Cells were resuspended in cold hypotonic KCl 0.56% solution, and kept at room temperature for 6 minutes. Next cells were pelleted again, resuspended in 0.5ml of the supernatant and 2 ml of ice-cold freshly-made fixative made by mixing Methanol: Glacial Acetic Acid (3:1) (Merck, 1060182500) was added dropwise while gently vortexed. Cells were pelleted again by centrifugation (as before) and the fixation step was repeated. Metaphase chromosome spreads were made by resuspension of cell pellets in 1ml of fixative and pipetting the suspension onto fixative-washed slides from a high distance (approximately 1,5 meters). Slides were dried and stained using DAPI containing Fluoroshield (Sigma, F6057). An oil immersion microscope was used for visualization with 100x magnification.

Neuronal differentiation

The protocol was adapted from Bibel et al., 2007. Mouse embryonic stem cells (mESC) were harvested by trypsinization with TrypLE™ Express for 5 min at 37°C (Heracell™ 240i CO₂ Incubator). Trypsin was quenched with an equal volume of EB medium (10% FBS, 1% Non-Essential Amino Acids, 1% Penicillin and Streptomycin, 1% GlutaMax, 1% Sodium Pyruvate, 0.1% B-mercaptoethanol, 86% DMEM High Glucose) and cells were counted manually. mESC were plated at a density of 4x10⁶ cells per bacteriological petri dish (10 cm Ø) in 15 ml of EB medium per dish. This time point is marked as the start of the experiment and is further called Day In Vitro -8 (DIV-8). Cells were cultured at 37°C with 5% of CO₂. On day 2 medium with the Embryoid Bodies (EB) was transferred to the falcon tube, and after 5 min supernatant was aspirated and pelleted EBs were resuspended in fresh EB medium (DIV-6). Resuspended EBs were dispensed into new bacteriological Petri dishes (10 cm Ø) in EB medium volume up to 15 ml per dish, and incubated as earlier. On day 4 (DIV-4) and day 6 (DIV-2) the medium was changed as before using EB medium supplemented with 5µM retinoic acid. On day 8 (DIV0) EBs were collected as before and washed twice with 10 ml of PBS. Subsequently, EBs were resuspended in 1ml T medium (0.05% Trypsin, 0.05% EDTA dissolved in PBS) and incubated with constant shaking for 3 min in a 37°C water bath. Trypsinized EB's were quenched with 1 ml of ESC medium and cells were pelleted down using Eppendorf 5810R Centrifuge (180 g for 5 min). The supernatant was aspirated and the cells were resuspended in 5 ml of N2 medium which was then filtered through a 70µm cell strainer. The cells were counted as before and plated at 11.34x10⁶ cells per Nunclon Plate (10 cm Ø) coated with poly-D-Lysine followed by laminin (Roche). Cells were cultured as earlier in the Incubator set up at 37°C with 5% of CO₂. After 2, 24 and 48 hours from plating, the N2 medium was changed. Consecutively, media was changed to B27 and fresh media was provided every second day. Neuronal differentiation was conducted till DIV23.

RNA extraction and cDNA synthesis

Total RNA for microexon splicing validation and for RNA-seq was extracted using the RNeasy Plus Mini kit (Qiagen, 74136). Consequently, total eukaryotic RNA samples were treated with

DNase using TURBO DNA-free™ Kit (Thermo Fisher Scientific) in order to remove DNA contamination. RNA was stored at -80°C for further experiments or for Reverse Transcription. Reverse transcription was performed using SuperScript III Reverse transcriptase (Invitrogen, 18080044) as advised by the manufacturer. 5 uM oligo(dT)₂₀ (Sigma, own design) were used together with an 1 mM dNTP mix (Invitrogen, 10297018) and incubated for 5 min at 65°C. Samples were stored for 3 minutes at 4°C, and a Reverse Transcription Master Mix was added (1ul of SuperScript III Reverse transcriptase (100U), 4ul of 5x first-strand RT buffer, 1ul of DTT 0.1M, 1 ul of Ribolock RNase inhibitor (20U, Thermo, EO0381), and 4 ul of RNase-free H₂O. The reaction was incubated for 50 minutes at 50°C, and next for 15 minutes at 70°C. The cDNA samples were stored at -20°C.

RNA-seq library preparation and sequencing

Library preparation and the RNA-seq were performed by the CRG Genomics Core Facility. Briefly, TruSeq Stranded mRNA Sample Prep Kit v2 (Illumina, RS-122-2101/2) was used according to the manufacturer's instructions. Poly(A)-mRNA selection was performed by incubation of the Total RNA with streptavidin-coated magnetic beads, and subsequently fragmentation. cDNA synthesis following the Protocol for use with NEBNext Poly(A) mRNA Magnetic Isolation Module (NEB E7490). cDNA was purified using AMPure XP beads (Agencort) following end repair, the addition of a single dA, and ligation with indexed adaptors (NEB E7500). Adaptor ligated DNA samples were purified using AMPure XP beads (Agencort) enriched by 14 cycles of PCR (NEB E7490) using the ProFlex™ 3 x 32-well PCR System. Prepared libraries were quantified and the quality of the library was assessed using Agilent DNA 1000 chip. Quantification was performed by qPCR-RT with KAPA Library Quantification Kit (KapaBiosystems, KK4835). 50 bp single-end sequencing was performed on Illumina HiSeq 2500.

PCR and RT-PCR

GoTaq G2 Flexi DNA Polymerase enzyme (Promega, M7806) was used according to the manufacturer's instructions. PCRs were performed using thermal-cyclers (Applied Biosystems, 2720). Standard PCR conditions were used as advised and the time of

elongation and the temperature of annealing were adjusted depending on amplicon size and the primers respectively. The PCR product was size-fractionated using 1% or 2.5% ultrapure agarose (Invitrogen, 16500500) depending on amplicon size. For visualization, SYBR Safe DNA Gel Stain (Invitrogen, S33102) was used. Gel electrophoresis was performed using 1x TBE (89mM Tris, 89mM boric acid, 2mM EDTA at 100V till full band separation. Amplicons were using GelDoc transilluminator (Biorad).

Molecular cloning of Daam1 FH2 domain

In order to clone the functional FH2 domain of DAAM1, we have used RNA extracted from Human Embryonic Kidney 293 (HEK-293T) cells as well as SH-SY5Y cells. RNA samples were extracted from 1 million cells using the RNeasy Mini Kit (50) (QIAGEN). Consequently, RNA samples were treated with DNase using the TURBO DNA-free™ Kit (Thermo Fisher Scientific) in order to remove DNA contamination. Afterwards, 1000 ng of RNA was reverse transcribed into cDNA using High-Capacity cDNA Reverse Transcription Kit (Thermo Fisher Scientific). Standard PCR procedure was used to amplify FH2 domains of DAAM1 as described previously.

Protein expression and purification

To investigate the role of microexon in the FH2 domain of DAAM1, 2 constructs (with and without microexon) of human DAAM1 homolog have been prepared. FH2 domain (residues 594-1077) was expressed as a fusion protein with N-terminal IgG tag plus C-terminal Strep-tag in *E. coli* strain BL21-CodonPlus(DE3)-RIL strain (Agilent Technologies). All cells were cultured at 37°C until OD_{600nm} reached 0.5, following which the media was cooled to 18°C and Isopropyl β-D-1-thiogalactopyranoside (IPTG; ROTH) was added to the final concentration of 0.1mM to induce protein expression respectively. Bacterial cultures were grown overnight at 18°C in the incubator

following which cells were harvested by centrifugation at 4°C (15min, 4000rpm) and disrupted either by sonication.

Sonication was conducted in HEKG 10 buffer (20 mM HEPES, pH 7.4, 1 mM EDTA, 50 mM KCl, 10% glycerol) with 1 mM DTT supplemented with cOmplete EDTA-free Protease Inhibitor Tablet (Roche). After centrifugation (Eppendorf 5810R Centrifuge) at 4°C (20min, 20000rpm), the proteins of interest were purified using StrepTrap HP column (GE Healthcare) at 4°C. The N-terminal tag was cleaved with His-C3 protease and the C-terminal tag with His-TEV protease. Both proteases were further removed using Ni-NTA Agarose beads. Individual pooled target proteins were further purified by a passage through a Superose 6 column (GE Healthcare).

Immunofluorescence stainings and confocal imaging of cultured neurons.

Cells on DIV0 or on DIV21 were washed with phosphate-buffered saline (PBS), fixed in 4% paraformaldehyde in PBS for 10 minutes, next permeabilized in 0.3% Triton X-100/PBS for 10min, blocked for 1h in 0.3% Triton X-100/PBS/6% bovine serum albumin and incubated in primary antibodies at 4°C overnight. Following overnight primary antibody incubation, cells were incubated with corresponding secondary antibodies for 1h at room temperature and mounted in FluoroShield with DAPI for imaging. Images were taken on an SP8 confocal microscope (CRG, Advanced Light Microscopy Unit) using identical settings for each condition in a given experiment with a dry 20x objective or 63X oil-immersion objective depending on the experiment. Confocal sections were Z stack projected with maximum intensity selection and were analyzed in ImageJ software. Compared cell lines had the same amounts of confocal sections.

Immunohistochemical Visualization of mice Hippocampus

Mice hippocampal sections were prepared as described (Hoeymissen et al., 2020), briefly: Mice were euthanized with CO₂, perfused transcardially with 0.1M PBS followed by 4% paraformaldehyde in PBS till complete tissue clearance of blood. Post-fix brains were extracted and stored in 4% paraformaldehyde at 4 °C for 24 hr and in sucrose 30% with 0.01% azide in PBS for the following 24 hrs. Prepared tissues were cut into 40 µm coronal sections, in serial order throughout the dorsal hippocampus (Bregma sections between -1.34mm to -2.54mm). Sectioning was performed by an in house Tissue Engineering Unit (CRG).

A detailed list of all stainings and primary antibodies used:

	Stain	Host	Catalog n°	Dilution
Primary antibody	Synaptophysin 1	Guinea pig	101004	1:1000
	DAAM1	Rabbit	14876-1-AP	1:100
	Arc (C-7)	Mouse	sc-17839	1:100
	β-3 Tubulin (TUBB3)	Rabbit	PRB-435P	1:400
	α-Tubulin (DM1A)	Mouse	3873	1:1000
Secondary antibody	anti-Rabbit IgG – Alexa Fluor 488	Goat	A-11034	1:1000
	anti-Guinea Pig IgG – Alexa Fluor 555	Goat	A-21435	1:1000
	anti-Mouse IgG – Alexa Fluor 594	Goat	A-11005	1:1000
	anti-Rabbit IgG – Alexa Fluor 647	Chicken	A-21443	1:1000
Reagent	Phalloidin-iFluor 647	-	ab176759	1:2000
	SiR-Actin	-	SC001	1:1000
	Fluoroshield™ with DAPI	-	F6057-20ml	-

Actin assembly assays

Pyrene labelled actin protein (UniversalBiologicals) was prepared as suggested by the manufacturer, shortly: Actin was equilibrated for 1h at 4°C in G-buffer (5 mM Tris-HCl (pH 8.0), 0.2 mM CaCl₂), spun 30min 14,000 rpm and after addition of the 10x Polymerization buffer (500mM KCl, 20 mM MgCl₂, 10mM ATP), and used for the experiments. Actin assembly was measured in 60 µl reactions using 96 Well Black Polystyrene Microplate (Corning®, CLS3904). Pyrene fluorescence was monitored over-time at 24°C at an excitation of 365 nm and emission of 407 nm in a fluorescence spectrophotometer (Tecan Infinite 200 PRO). Rates of actin assembly were calculated from the slopes of the assembly curves at 50% polymerization as described by Doolittle et al. 2013.

TIRF Microscopy

TIRF-based F-actin polymerization experiments were performed using manually assembled flow-cells consisting of piranha-cleaned, silanized, PEG-passivated glass coverslips (22 X 22 mm #1.5 (i.e. 170 +/- 5 um) from MARIENFELD (Cat # 0107052)) and a PLL-PEG passivated glass slide. Flow cells were primed by flushing 55 ul of a solution of 5% Pluronic F-127 (P2443, Sigma-Aldrich) and then incubated for 10 minutes at room temperature. Next, flow cells were washed twice with 55 ul of kappa-Casein (1:100 in 1X G buffer of 5 mg/ml stock in 1X Brb80 buffer). Absorptive paper (Whatman filter paper) was used to flush the chamber by holding the paper on one side of the channel while adding the solution dropwise on the other side. Next, chambers were equilibrated with the G-buffer and the reaction mixture was loaded. The actin polymerization reaction mix contained the protein of interest and actin, which were diluted in freshly prepared buffer containing 5 mM Tris-HCl (pH 8.0), 0.2 mM CaCl₂, 50 mM KCl, 2mM MgCl₂, 2mM ATP, 2mM DTT, 1% (w/vol) glucose, 0.2mM Brij-35, oxygen scavengers (180 mg/ml catalase (C40, Merck) and 752 mg/ml glucose oxidase (22778.01, Serva)), 0.15% (w/vol) methylcellulose (4000 cP, Sigma-Aldrich); actin labelling was achieved using SiR-Actin (TeuBio). After loading the reaction mixture, flow cells were finally sealed with vacuum grease and placed onto the microscope stage for observation.

Dual-colour TIRF imaging has been performed with a custom assembled microscope (Cairn Research, Faversham, UK) using a 100X oil-immersion objective (Nikon CFI SR Apo, NA = 1.49), 488 nm and 640 nm simultaneous laser excitation at a TIRF angle of 80 deg, and two EMCCDs for fluorescent detection using a dichroic (T565lpxr, Chroma) to split the fluorescence and a 525/50 bandpass filter (284337, Chroma) for DAAM1-SNAP-Alexa488 detection and a 655 long-pass filter (283943, Chroma) for SiR-actin detection. Imaging was performed at room temperature for 2 hours taking 1 image every 2 minutes in 3 to 5 different sample locations chosen randomly and using 100 ms exposure time and 100 and 250 EM gain values, respectively for SiR-actin and DAAM1-SNAP-Atto488 detection.

Experimental mice

Chimeric mice were obtained by blastocyst injection of genetically modified mouse embryonic stem (mES) cells ([129xC57Bl/6 background](#)) into albino BL6 embryos (pseudopregnant CD1 female derived). Consecutively, parental backcross one mice were derived by fur colour selection after the chimeric mice cross with CD1 females. Daam1_dMIC mice and wild-type (WT) littermates were obtained by 4 backcrosses of backcross 1 mice with C57BL6. The colony was maintained at the Animal Facility of the Barcelona Biomedical Research Park (PRBB).

All procedures were approved by the PRBB Animal Research Ethics Committee and the Generalitat de Catalunya and were carried out in accordance with the guidelines of the European Union Council (2003/65/CE) and Spanish regulations (BOE 252/34367-91, 2005).

In Utero Cortical Electroporation

Performed as described in (Meyer-Dilhet and Courchet, 2020) with small modifications. Cortical electroporation was performed with CAG-GFP plasmid mixed with Fast Green FCF dye (Sigma F7252, dye concentration at 1/10). Unipolar electroporation was performed with 5 pulses at 35V, with pulse duration 50msec and interval 950msec.

Behavioural and Motor Tests in a Neonatal Mouse

A battery of motor tests has been performed as described in Feather-Schussler and Ferguson (2016) and Roper et al. 2021 with some adjustments. The following tests were performed on PDs 4, 7, 10, 14:

Pivoting and walking

Pivoting is a voluntary exploratory behaviour displayed by young mice before the forward locomotion. To measure pivoting, mice were placed on a flat surface and allowed to move freely for 1 minute. The number of times the animals made a 90° turn was recorded. Pivoting was measured based on the body axis with the help of a cross marking 90° angles on the experimental surface. The

latency to walk in a straight line after the end of the pivoting behaviour was also measured. Two trials were performed per animal.

Righting reflex

In order to study the righting reflex, mice were placed on their back on a padded table top. The time taken for the animals to right themselves back to four paws through 180° was measured for a maximum of 1 min. The direction of turning was also recorded. The experiment was performed 3 times per animal.

Preyer's reflex

The Preyer's reflex is a startle response triggered by sharp auditory stimuli is used to assess hearing in rodents (Jero, Donald E. Coling, Anil K. Lal, 2001). The experimenter made a sharp clapping sound by stretching and releasing a rubber glove onto the hand in the proximity of the mouse and recorded the presence of rapid whole-body movement.

Front-limb suspension

To measure forelimb strength, mice were allowed to grasp with both forepaws on a horizontal bar suspended above a padded drop zone. The latency to fall was measured in three trials per animal.

Hindlimb suspension

To measure hindlimb strength, mice were lowered into a 50ml conical tube and released with their hindlimbs hung over the rim. The latency to fall was measured for up to 30s. Hindlimb posture upon falling was scored 0-4 based on the limb spread, as described in Feather-Schussler and Ferguson (2016). The experiment was performed only once unless the animal fell down immediately due to bad placement.

Grasping reflex

The animals were held by the scruff of the neck and each paw was touched by a toothpick to elicit the grasping reflex. Performance was scored 0-4, assigning one point per paw in the presence of grasping. Left and right paw preference was also noted.

Cliff aversion

Cliff aversion tests the labyrinth reflexes, as well as normal strength and coordination. Mice were placed on top of a box elevated ~10cm above the surface, with their snout and part of their forepaws just over the edge. The presence of aversive movement away from the cliff within the 30s was recorded. If the pup fell down, one additional trial was performed.

Negative geotaxis (NG)

NG is an automatic vestibular response to geogravitational stimuli and is used to measure motor coordination in pups. Mice have been primarily placed head-facing uphill on a plastic platform with an inclination of 45° covered with Surface Protector Paper and spunlace wipes (VWR). On PD 4, the incline was adapted to 30°. After ~5s, the pups were turned by 180° to face downhill, and their movement was observed for 1 min. Two trials were performed, turning the animal in opposite directions to the start position to avoid left-right bias. Animals were given 0.5 points per 45° of turning. If a full 180° turn was performed, the latency was also recorded. Left and right turning preferences were also noted.

Homing test

Homing was performed as described in Roper et al. 2021 with adjustments. The homing test is a measurement of social olfactory, cognitive, and sensorimotor abilities required to navigate towards olfactory cues from the pup's own cage. A pup is removed from the home cage and is placed in the corner of a new clean cage (12.5 × 45 cm w × h) facing the wall. The new cage is filled with clean wood shavings, familiar nesting material from their own home cage is provided in the opposite corner. The time for the pup to reach the area containing the nesting material is recorded in seconds, with a maximum time of 2 min.

Behavioural tests in Adult Mouse

Locomotor activity in open cage

Motor activity was evaluated under two different conditions: in a short 5 min cycle in a novel environment, and in a semi-familiar 23h cycle using the activity cage.

Spontaneous basal locomotor day and night activity in an open cage was measured for 23h using an infrared Actimeter (PANLAB SA, Spain). Individual mice were placed in the open field (25 x 25 cm), and their position in time was recorded based on the disruption of IR beams in the x and y axes. The arena was covered with a layer of wood shavings, and sufficient water and food were provided.

Short-term locomotor activity in a novel environment was measured in the Habituation phase of the Novel Object Recognition Test (see NOR). This provided a measurement of activity, thigmotaxis and anxiety-related behaviour in a novel environment, using the parameters recorded by the SMART 3.0 software (System Motor Activity Record and Tracking, PANLAB SA, Spain). This system analyses horizontal activity through parameters, such as distance travelled and average speed. It can also differentiate between activities in self-defined areas within the experimental setup.

NOR (Novel Object Recognition) - recognition memory.

The NOR test measures recognition memory based on the visual paired-comparison paradigm (Leger et al., 2013; Lueptow, 2017). The experiment consists of three sessions carried out on consecutive days: habituation, familiarisation, and discrimination. Recordings during habituation were also used to measure short-term locomotor behaviour in the open field.

The experiment was performed in a 38.5 cm x 38.5cm arena with long, 38.5cm high dark plastic walls and an open top. The arena was illuminated from the top, and the animals were tracked using video recording and the Smart 3.0 software (System Motor Activity Record and Tracking, PANLAB SA, Spain). To minimise stressors interfering with the experiment, a curtain was mounted separating the arena from the experimenters. The arena and the objects were cleaned with 70% ethanol between each mouse to remove odours.

Cages were transferred to the experimental room 30min before the trials to acclimatise. The test was carried out under slightly aversive conditions (white light 50 lux).

Habituation: On the first day, animals were placed into the arena facing the wall and were recorded for 5min. Their movement was measured separately by the Smart 3.0 software in a central (20 x 20 cm) and a peripheral zone. Apart from habituating animals to the area, this trial served to measure short-term activity.

Familiarisation: On the second day, two identical objects (A and B) were placed in the centre of the box, 18 cm apart. Animals were placed into the box facing the wall and were recorded for 10min. The time spent exploring each object was measured manually using a timer. The latency to climb on top of the objects was also noted. The exploration was defined as the time spent sniffing the object from a close distance, excluding the time spent climbing on the object. Exploration threshold was established at 20 seconds.

Discrimination: On the third day, one of the objects was replaced with a novel object of a different shapes and colours. Animals were placed into the box facing the wall as before and were recorded for 5 min. The time spent exploring each object was measured manually using a timer. The latency to climb on top of the old and novel objects was noted.

Discrimination and preference indices were calculated for familiarisation and discrimination for each animal based on the manual exploration time recordings, as described in Lueptow et al. (2017).

Elevated Plus Maze - Anxiety-related behaviour.

Anxiety-related behaviour was measured in the Elevated plus maze, as described by Walf and Frye, 2007 with some modifications. The apparatus consisted of a cross-shaped platform with four arms (30cmx5cm) elevated 40cm off the ground. Two arms were open and two were enclosed by 15cm high black methacrylate walls. The open arms create an aversive environment for the mouse, while the dark enclosed space of the closed arms is considered safe. The number of open arm entries and the relative time spent in the open

arms is indicative of anxiety-related behaviour. Animals that avoid open arms are considered more anxious.

Mice were lowered onto the end of the same closed-arm facing the walls and their movement was recorded for 5min using the Smart 3.0 software. Separate zones were set up for each arm, the ends of the arms (5cmx5cm) and the centre of the cross (5cmx5cm). Measurements included the percentage of the time, entries, distance travelled, and average speed in each zone. Rearings and head dippings from the central zone were recorded manually. The arena was cleaned with 70% ethanol between each animal to remove odours.

Morris Water Maze – Spatial learning and reference memory

Learning and visual-spatial memory were tested in the Morris water maze (Morris, 1984), with some modifications (Vorhees and Williams, 2006). In this experiment, mice must learn the spatial location of a submerged platform to escape from the water by building a cognitive allocentric map with the help of external visual cues. The experiment consists of the following phases: training trials, removal, cued trials, and reversal training.

A metal tank (150 cm in diameter) was filled with water (22-23°C) with added white, non-toxic finger paint to conceal the location of the platform. The platform (12 cm in diameter) was submerged 0.7 cm below the water surface. Four quadrants (NE, NW, SE, SW) and a platform zone were defined using the Smart 3.0 software, with the platform located in the centre of one quadrant (NE). A curtain was mounted around the tank to separate it from the experimenters and minimise external visual cues. Three distal visual cues, a square, a triangle and a circle were placed on the curtains around the tank at equal distances, ~30cm above the water surface.

Training trials: During training, the mice learn the task and the location of the platform. Four 1-minute training trials were performed each day, with an inter-trial interval of ~1h. 8 training days were performed to achieve sufficient learning. Mice were released into the water. The latency to reach the platform was recorded and the animal was removed from the water. 5 to 15 s platform localization learning and positive reinforcement was used

by placing the animal on the platform depending on performance (goal accomplishment and its lack accordingly).

Removal: the platform is removed from the tank and the animals are tested for 1 min 24h after the last training. Animals were released from the location furthest away from the original platform (SW). Mice that remember the location of the platform are expected to spend more time in the platform quadrant (NE).

Cued trials: In these guided learning trials, the platform is placed back to its original location and is marked by a local visual cue. Animals have an inherent tendency to swim towards the flag. Therefore, these trials can detect issues with swimming, visual perception and/or motivation to perform the task. A flag (~10cm above the water surface) fixed to a metal bar was used as a local cue. Distant visual cues were removed. Two 1-minute cued trials were performed ~1h after the removal session.

Reversal training: During a spatial reversal, the platform is placed opposite to its original location (SW). Mice must flexibly re-learn the spatial location of the platform. 4 trials were performed for 2 days, as described in the training trials.

In all trials, the latency to reach the platform and platform crossovers were measured. Animals were tracked using the Smart 3.0 software, allowing measurement of time, speed and distance travelled in each quadrant. Distances from the platform were used to calculate cumulative search error and mean proximity as additional measurements of spatial learning (Pereira & Burwell, 2015). Floating was also measured manually.

Grip strength

The grip strength experiment is a measurement of neuromuscular function and limb muscle strength. Mice were held by the tail and lowered onto the metal grid of the apparatus (Grip Strength Meter, Bioseb, France), allowing them to grip with their paws. Mice were next pulled backwards along the grid at a consistent speed, while the apparatus measured the force exerted by the animals on the grid. Grip strength was measured for forelimbs only with 3 consecutive trials. Best, average, and mean grip strengths were calculated.

Rotarod – coordination and balance

The Rotarod test measures coordination, balance and fatigue resistance (Deacon, 2013). Mice are placed on a rotating horizontal rod and must walk on it to avoid falling. The Rotarod apparatus (PanLab Rotarod LE8200, Spain) consists of 5 separated lanes on a horizontal rod (5 cm in diameter and 10 cm long) elevated 20cm above the ground. Falling is detected by a lever on the landing site, which automatically records falling latency and rotation speed. Mice were lowered onto the rod by the tail facing away from the direction of rotation. Sessions were re-started if the mouse fell down within 5s due to bad placement.

First, animals were trained to walk on the rod at 4rpm. Training sessions were performed until the mouse managed to walk on the rod for 1 min. After training, test sessions were performed at five constant speed settings (7, 14, 19, 24, 34 rpm). Two trials were carried out per speed, with a maximum length of 2 min. Finally, two trials were performed where the rotation speed accelerated constantly from 4 to 40 rpm in the 60s. Two trials were carried out per speed, with a maximum length of 2min. Finally, two trials were performed where the rotation speed accelerated constantly from 4 to 40 rpm in the 60s.

Beam Balance

Balance, coordination, and vestibular function were measured in the Beam Balance experiment (Luong et al., 2011). Mice were placed in a standing position in the centre of a narrow wooden beam (1cmx50cm) elevated 45cm above the ground. They were scored 0-3 based on how far they walked on the beam within 1 min (0: falls off; 1: <10cm; 2: >10cm; 3: reaches the end). Falls and the number of slips were recorded. Latency to reach one of the ends and the direction of movement (left/right) were also noted.

Measurement of intracellular $[Ca^{2+}]$

Cytosolic Ca^{2+} signal was determined at room temperature in cells loaded with 4,5 mM FURA2-AM (30 min incubation at 37°C). Ca^{2+} responses were calculated as the ratio of emitted fluorescence (510 nm) after excitation at 340 and 380 nm, relative to the ratio measured prior to cell stimulation (FURA2-AM ratio 340/380). Briefly, cells were maintained in an isotonic solution containing (in mM): 140 NaCl, 5 KCl, 1.2 CaCl₂, 0.5 MgCl₂, 5 glucose, 10 HEPES (305 mosmol/l, pH 7.4 with Tris) for 2 minutes and then stimulated with a 30 mM KCl solution (115 NaCl, 30 KCl, 1.2 CaCl₂, 0.5 MgCl₂, 5 glucose, 10 HEPES) to activate voltage-gated calcium entry. As indicated in the respective figure legends, cells were treated with 5 μM Latrunculin A (LatA), 50 μM small-molecule inhibitor of Formin Homology 2 domains (SMIFH2) or vehicle (DMSO). The treatment was maintained for the duration of the experiment (40 minutes). In the case of SMIFH2, its effect on neuronal cultures was measured after 90 min exposure to 50 μM SMIFH2. All experiments were carried out at room temperature as described previously (Fernandes et al., 2008). AquaCosmos software (Hamamatsu Photonics) was used for capturing the fluorescence ratio at 510 nm obtained post-excitation at 340 and 380 nm, respectively. Images were computed every 5 s. Measurements were processed using SigmaPlot 10 software.

Sample-to-sample correlation distance matrices and principal component analysis

Read alignment and transcript abundance quantification was performed with Salmon 13.1 (Patro et al., 2017). Mus musculus (house mouse) genome assembly GRCm38 (mm10) from Genome Reference Consortium was used. For analysis of gene expression, DESeq2 has been used (Love et al., 2014) where filtering and normalization were performed following the standard pipeline. Principal component analysis (PCA) was done using the top 500 most variable genes and plotted using the part of DESeq2::plotPCA R package.

Differential Gene Expression (DGE) analysis

Differential gene expression (DGE) analysis between samples was performed using independent hypothesis weighting (IHW; (Ignatiadis et al., 2016)) and log fold change shrinkage (LFC). DGE

was calculated for the hippocampal samples compared to control wild-type vs Daam1 microexon lacking mice while taking into consideration the age of the mice, sex and sample extraction. We used a 0.05 FDR cut-off to call differentially expressed genes.

Gene enrichment analysis

Calculated p values and adjusted p values using THE DESeq2 R package were used for gene enrichment analysis using Enrichr (Chen et al., 2013; Kuleshov et al., 2016; Xie et al., 2021). Statistical significance of GO-term enrichment was defined using p-values.

Bibliography

Ahuja, R., Pinyol, R., Reichenbach, N., Custer, L., Klingensmith, J., Kessels, M.M., and Qualmann, B. (2007). Cordon-bleu is an actin nucleation factor and controls neuronal morphology. *Cell* *131*, 337–350.

Anand, K.S., and Dhikav, V. (2012). Hippocampus in health and disease: An overview. *Ann. Indian Acad. Neurol.* *15*, 239–246.

Arganda-Carreras, I., Fernández-González, R., Muñoz-Barrutia, A., and Ortiz-De-Solorzano, C. (2010). 3D reconstruction of histological sections: Application to mammary gland tissue. *Microsc. Res. Tech.* *73*, 1019–1029.

Avilés, E.C., and Stoeckli, E.T. (2016). Canonical wnt signaling is required for commissural axon guidance: Canonical Wnt Signaling in Axon Guidance. *Dev. Neurobiol.* *76*, 190–208.

Azevedo, F.A.C., Carvalho, L.R.B., Grinberg, L.T., Farfel, J.M., Ferretti, R.E.L., Leite, R.E.P., Filho, W.J., Lent, R., and Herculano-Houzel, S. (2009). Equal numbers of neuronal and nonneuronal cells make the human brain an isometrically scaled-up primate brain. *J. Comp. Neurol.* *513*, 532–541.

Beane, W.S., Tseng, A.-S., Morokuma, J., Lemire, J.M., and Levin, M. (2012). Inhibition of Planar Cell Polarity Extends Neural Growth During Regeneration, Homeostasis, and Development. *Stem Cells Dev.* *21*, 2085–2094.

Bibel, M., Richter, J., Schrenk, K., Tucker, K.L., Staiger, V., Korte, M., Goetz, M., and Barde, Y.-A. (2004). Differentiation of mouse embryonic stem cells into a defined neuronal lineage. *Nat. Neurosci.* *7*, 1003–1009.

Bibel, M., Richter, J., Lacroix, E., and Barde, Y.-A. (2007). Generation of a defined and uniform population of CNS progenitors and neurons from mouse embryonic stem cells. *Nat. Protoc.* *2*, 1034–1043.

Breitsprecher, D., Kiesewetter, A.K., Linkner, J., and Faix, J. (2009). Analysis of Actin Assembly by In Vitro TIRF Microscopy. In *Chemotaxis*, T. Jin, and D. Hereld, eds. (Totowa, NJ: Humana Press), pp. 401–415.

Budday, S., Steinmann, P., and Kuhl, E. (2015). Physical biology of human brain development. *Front. Cell. Neurosci.* *9*, 257.

Chen, E.Y., Tan, C.M., Kou, Y., Duan, Q., Wang, Z., Meirelles, G.V., Clark, N.R., and Ma'ayan, A. (2013). Enrichr: interactive and

collaborative HTML5 gene list enrichment analysis tool. *BMC Bioinformatics* *14*, 128.

Cingolani, L.A., and Goda, Y. (2008). Actin in action: the interplay between the actin cytoskeleton and synaptic efficacy. *Nat. Rev. Neurosci.* *9*, 344–356.

Colombo, A., Palma, K., Armijo, L., Mione, M., Signore, I.A., Morales, C., Guerrero, N., Meynard, M.M., Pérez, R., Suazo, J., et al. (2013). Daam1a mediates asymmetric habenular morphogenesis by regulating dendritic and axonal outgrowth. *Development* *140*, 3997–4007.

Corkin, S. (2002). What's new with the amnesic patient H.M.? *Nat. Rev. Neurosci.* *3*, 153–160.

Da Silva, J.S., and Dotti, C.G. (2002). Breaking the neuronal sphere: regulation of the actin cytoskeleton in neurogenesis. *Nat. Rev. Neurosci.* *3*, 694–704.

Deacon, R.M.J. (2013). Measuring Motor Coordination in Mice. *J. Vis. Exp.* 2609.

Dillon, C., and Goda, Y. (2005). THE ACTIN CYTOSKELETON: Integrating Form and Function at the Synapse. *Annu. Rev. Neurosci.* *28*, 25–55.

Dogterom, M., and Koenderink, G.H. (2019). Actin–microtubule crosstalk in cell biology. *Nat. Rev. Mol. Cell Biol.* *20*, 38–54.

Doolittle, L.K., Rosen, M.K., and Padrick, S.B. (2013). Measurement and Analysis of In Vitro Actin Polymerization. In *Adhesion Protein Protocols*, A.S. Coutts, ed. (Totowa, NJ: Humana Press), pp. 273–293.

Eltokhi, A., Kurpiers, B., and Pitzer, C. (2021). Comprehensive characterization of motor and coordination functions in three adolescent wild-type mouse strains. *Sci. Rep.* *11*, 6497.

Feather-Schussler, D.N., and Ferguson, T.S. (2016). A Battery of Motor Tests in a Neonatal Mouse Model of Cerebral Palsy. *J. Vis. Exp.* 53569.

Foldi, I., Szikora, S., and Mihály, J. (2017). Formin' bridges between microtubules and actin filaments in axonal growth cones. *Neural Regen. Res.* *12*, 1971.

Gasperini, R.J. (2017). How does calcium interact with the cytoskeleton to regulate growth cone motility during axon pathfinding? *Mol. Cell. Neurosci.* *7*.

Gonatopoulos-Pournatzis, T., Niibori, R., Salter, E.W., Weatheritt, R.J., Tsang, B., Farhangmehr, S., Liang, X., Braunschweig, U., Roth, J., Zhang, S., et al. (2020). Autism-Misregulated eIF4G

Microexons Control Synaptic Translation and Higher Order Cognitive Functions. *Mol. Cell* 77, 1176-1192.e16.

Gould, T.D., and Einat, H. (2007). Animal models of bipolar disorder and mood stabilizer efficacy: A critical need for improvement. *Neurosci. Biobehav. Rev.* 31, 825–831.

Grienberger, C., and Konnerth, A. (2012). Imaging Calcium in Neurons. *Neuron* 73, 862–885.

Hoeymissen, E.V., Philippaert, K., Vennekens, R., Vriens, J., and Held, K. (2020). Horizontal Hippocampal Slices of the Mouse Brain. *JoVE J. Vis. Exp.* e61753.

Ignatiadis, N., Klaus, B., Zaugg, J.B., and Huber, W. (2016). Data-driven hypothesis weighting increases detection power in genome-scale multiple testing. *Nat. Methods* 13, 577–580.

Irimia, M., Weatheritt, R.J., Ellis, J.D., Parikshak, N.N., Gonatopoulos-Pournatzis, T., Babor, M., Quesnel-Vallières, M., Tapial, J., Raj, B., O’Hanlon, D., et al. (2014). A Highly Conserved Program of Neuronal Microexons Is Misregulated in Autistic Brains. *Cell* 159, 1511–1523.

Jackson, S.J., Andrews, N., Ball, D., Bellantuono, I., Gray, J., Hachoumi, L., Holmes, A., Latcham, J., Petrie, A., Potter, P., et al. (2017). Does age matter? The impact of rodent age on study outcomes. *Lab. Anim.* 51, 160–169.

Jaiswal, R., Breitsprecher, D., Collins, A., Corrêa, I.R., Xu, M.-Q., and Goode, B.L. (2013). The Formin Daam1 and Fascin Directly Collaborate to Promote Filopodia Formation. *Curr. Biol.* 23, 1373–1379.

Jero, Donald E. Coling, Anil K. Lal, J. (2001). The Use of Preyer’s Reflex in Evaluation of Hearing in Mice. *Acta Otolaryngol. (Stockh.)* 121, 585–589.

Jumper, J., Evans, R., Pritzel, A., Green, T., Figurnov, M., Ronneberger, O., Tunyasuvunakool, K., Bates, R., Žídek, A., Potapenko, A., et al. (2021). Highly accurate protein structure prediction with AlphaFold. *Nature* 596, 583–589.

Jung, M., Kim, D., and Mun, J.Y. (2020). Direct Visualization of Actin Filaments and Actin-Binding Proteins in Neuronal Cells. *Front. Cell Dev. Biol.* 8, 588556.

Kawabata Galbraith, K., Fujishima, K., Mizuno, H., Lee, S.-J., Uemura, T., Sakimura, K., Mishina, M., Watanabe, N., and Kengaku, M. (2018). MTSS1 Regulation of Actin-Nucleating Formin DAAM1 in Dendritic Filopodia Determines Final Dendritic Configuration of Purkinje Cells. *Cell Rep.* 24, 95-106.e9.

- Koltun, B., Ironi, S., Gershoni-Emek, N., Barrera, I., Hleihil, M., Nanguneri, S., Sasmal, R., Agasti, S.S., Nair, D., and Rosenblum, K. (2020). Measuring mRNA translation in neuronal processes and somata by tRNA-FRET. *Nucleic Acids Res.* *48*, e32.
- Konietzny, A., Bär, J., and Mikhaylova, M. (2017). Dendritic Actin Cytoskeleton: Structure, Functions, and Regulations. *Front. Cell. Neurosci.* *11*, 147.
- Kozareva, D.A., Cryan, J.F., and Nolan, Y.M. (2019). Born this way: Hippocampal neurogenesis across the lifespan. *Aging Cell* *18*, e13007.
- Kühn, S., and Geyer, M. (2014). Formins as effector proteins of Rho GTPases. *Small GTPases* *5*, e983876.
- Kuleshov, M.V., Jones, M.R., Rouillard, A.D., Fernandez, N.F., Duan, Q., Wang, Z., Koplev, S., Jenkins, S.L., Jagodnik, K.M., Lachmann, A., et al. (2016). Enrichr: a comprehensive gene set enrichment analysis web server 2016 update. *Nucleic Acids Res.* *44*, W90–W97.
- La Rosa, C., Parolisi, R., and Bonfanti, L. (2020). Brain Structural Plasticity: From Adult Neurogenesis to Immature Neurons. *Front. Neurosci.* *14*, 75.
- Lamprecht, R. (2021). Actin Cytoskeleton Role in the Maintenance of Neuronal Morphology and Long-Term Memory. *Cells* *10*, 1795.
- van der Lee, S.J., Knol, M.J., Chauhan, G., Satizabal, C.L., Smith, A.V., Hofer, E., Bis, J.C., Hibar, D.P., Hilal, S., van den Akker, E.B., et al. (2019). A genome-wide association study identifies genetic loci associated with specific lobar brain volumes. *Commun. Biol.* *2*, 285.
- Leger, M., Quiedeville, A., Bouet, V., Haelewyn, B., Boulouard, M., Schumann-Bard, P., and Freret, T. (2013). Object recognition test in mice. *Nat. Protoc.* *8*, 2531–2537.
- Leterrier, C., Dubey, P., and Roy, S. (2017). The nano-architecture of the axonal cytoskeleton. *Nat. Rev. Neurosci.* *18*, 713–726.
- Love, M.I., Huber, W., and Anders, S. (2014). Moderated estimation of fold change and dispersion for RNA-seq data with DESeq2. *Genome Biol.* *15*, 550.
- Lu, J., Meng, W., Poy, F., Maiti, S., Goode, B.L., and Eck, M.J. (2007). Structure of the FH2 Domain of Daam1: Implications for Formin Regulation of Actin Assembly. *J. Mol. Biol.* *369*, 1258–1269.
- Lueptow, L.M. (2017). Novel Object Recognition Test for the Investigation of Learning and Memory in Mice. *J. Vis. Exp.* 55718.

- Luong, T.N., Carlisle, H.J., Southwell, A., and Patterson, P.H. (2011). Assessment of Motor Balance and Coordination in Mice using the Balance Beam. *J. Vis. Exp.* 2376.
- Mattila, P.K., and Lappalainen, P. (2008). Filopodia: molecular architecture and cellular functions. 9.
- Matussek, T. (2006). The *Drosophila* formin DAAM regulates the tracheal cuticle pattern through organizing the actin cytoskeleton. *Development* 133, 957–966.
- Matussek, T., Gombos, R., Szecsenyi, A., Sanchez-Soriano, N., Czibula, A., Pataki, C., Gedai, A., Prokop, A., Rasko, I., and Mihaly, J. (2008). Formin Proteins of the DAAM Subfamily Play a Role during Axon Growth. *J. Neurosci.* 28, 13310–13319.
- McLeod, F., and Salinas, P.C. (2018). Wnt proteins as modulators of synaptic plasticity. *Curr. Opin. Neurobiol.* 53, 90–95.
- Merikangas, K.R., He, J., Burstein, M., Swendsen, J., Avenevoli, S., Case, B., Georgiades, K., Heaton, L., Swanson, S., and Olfson, M. (2011). Service Utilization for Lifetime Mental Disorders in U.S. Adolescents: Results of the National Comorbidity Survey–Adolescent Supplement (NCS-A). *J. Am. Acad. Child Adolesc. Psychiatry* 50, 32–45.
- Meyer-Dilhet, G., and Courchet, J. (2020). In Utero Cortical Electroporation of Plasmids in the Mouse Embryo. *STAR Protoc.* 1, 100027.
- Mollink, J., Smith, S.M., Elliott, L.T., Kleinnijenhuis, M., Hiemstra, M., Alfaro-Almagro, F., Marchini, J., van Cappellen van Walsum, A.-M., Jbabdi, S., and Miller, K.L. (2019). The spatial correspondence and genetic influence of interhemispheric connectivity with white matter microstructure. *Nat. Neurosci.* 22, 809–819.
- Morris, R. (1984). Developments of a water-maze procedure for studying spatial learning in the rat. *J. Neurosci. Methods* 11, 47–60.
- Moseley, J.B., Maiti, S., and Goode, B.L. (2006). Formin Proteins: Purification and Measurement of Effects on Actin Assembly. In *Methods in Enzymology*, (Elsevier), pp. 215–234.
- Nikolaienko, O., Patil, S., Eriksen, M.S., and Bramham, C.R. (2018). Arc protein: a flexible hub for synaptic plasticity and cognition. *Semin. Cell Dev. Biol.* 77, 33–42.
- Nishimura, T., Honda, H., and Takeichi, M. (2012). Planar Cell Polarity Links Axes of Spatial Dynamics in Neural-Tube Closure. *Cell* 149, 1084–1097.
- Niven, J.E., and Laughlin, S.B. (2008). Energy limitation as a

selective pressure on the evolution of sensory systems. *J. Exp. Biol.* *211*, 1792–1804.

Otomo, T., Tomchick, D.R., Otomo, C., Panchal, S.C., Machius, M., and Rosen, M.K. (2005). Structural basis of actin filament nucleation and processive capping by a formin homology 2 domain. *433*, 7.

Papandréou, M.-J., and Leterrier, C. (2018). The functional architecture of axonal actin. *Mol. Cell. Neurosci.* *91*, 151–159.

Park, S., Park, J.M., Kim, S., Kim, J.-A., Shepherd, J.D., Smith-Hicks, C.L., Chowdhury, S., Kaufmann, W., Kuhl, D., Ryazanov, A.G., et al. (2008). Elongation Factor 2 and Fragile X Mental Retardation Protein Control the Dynamic Translation of Arc/Arg3.1 Essential for mGluR-LTD. *Neuron* *59*, 70–83.

Patro, R., Duggal, G., Love, M.I., Irizarry, R.A., and Kingsford, C. (2017). Salmon: fast and bias-aware quantification of transcript expression using dual-phase inference. *Nat. Methods* *14*, 417–419.

Polder, G., Hovens, H., and Zweers, H. Measuring shoot length of submerged aquatic plants using graph analysis. *30*.

Pollard, T.D. (2016). Actin and Actin-Binding Proteins. *Cold Spring Harb. Perspect. Biol.* *8*, a018226.

Purro, S.A., Galli, S., and Salinas, P.C. (2014). Dysfunction of Wnt signaling and synaptic disassembly in neurodegenerative diseases. *J. Mol. Cell Biol.* *6*, 75–80.

Quesnel-Vallières, M., Irimia, M., Cordes, S.P., and Blencowe, B.J. (2015). Essential roles for the splicing regulator nSR100/SRRM4 during nervous system development. *Genes Dev.* *29*, 746–759.

Quesnel-Vallières, M., Dargaei, Z., Irimia, M., Gonatopoulos-Pournatzis, T., Ip, J.Y., Wu, M., Sterne-Weiler, T., Nakagawa, S., Woodin, M.A., Blencowe, B.J., et al. (2016). Misregulation of an Activity-Dependent Splicing Network as a Common Mechanism Underlying Autism Spectrum Disorders. *Mol. Cell* *64*, 1023–1034.

Raj, B., and Blencowe, B.J. (2015). Alternative Splicing in the Mammalian Nervous System: Recent Insights into Mechanisms and Functional Roles. *Neuron* *87*, 14–27.

Ran, F.A., Hsu, P.D., Wright, J., Agarwala, V., Scott, D.A., and Zhang, F. (2013). Genome engineering using the CRISPR-Cas9 system. *Nat. Protoc.* *8*, 2281–2308.

Rizzoli, S.O., and Betz, W.J. (2005). Synaptic vesicle pools. *Nat. Rev. Neurosci.* *6*, 57–69.

Roper, R.J., Goodlett, C.R., de Lagrán, M.M., and Dierssen, M.

(2020). Behavioral Phenotyping for Down Syndrome in Mice. *Curr. Protoc. Mouse Biol.* *10*, e79.

Ruhela, R.K., Soni, S., Sarma, P., Prakash, A., and Medhi, B. (2019). Negative geotaxis: An early age behavioral hallmark to VPA rat model of autism. *Ann. Neurosci.* *26*, 25–31.

Sakuma, T., Nishikawa, A., Kume, S., Chayama, K., and Yamamoto, T. (2015). Multiplex genome engineering in human cells using all-in-one CRISPR/Cas9 vector system. *Sci. Rep.* *4*.

Salomon, S.N., Haber, M., Murai, K.K., and Dunn, R.J. (2008). Localization of the Diaphanous-related formin Daam1 to neuronal dendrites. *Neurosci. Lett.* *447*, 62–67.

Schönichen, A., and Geyer, M. (2010). Fifteen formins for an actin filament: A molecular view on the regulation of human formins. *Biochim. Biophys. Acta BBA - Mol. Cell Res.* *1803*, 152–163.

Sellers, K.J., Elliott, C., Jackson, J., Ghosh, A., Ribe, E., Rojo, A.I., Jarosz-Griffiths, H.H., Watson, I.A., Xia, W., Semenov, M., et al. (2017). Amyloid β synaptotoxicity is Wnt-PCP dependent and blocked by fasudil. *Alzheimers Dement.*

Soykan, T., Kaempf, N., Sakaba, T., Vollweiler, D., Goerdeler, F., Puchkov, D., Kononenko, N.L., and Haucke, V. (2017). Synaptic Vesicle Endocytosis Occurs on Multiple Timescales and Is Mediated by Formin-Dependent Actin Assembly. *Neuron* *93*, 854-866.e4.

Su, C.-H., D, D., and Tarn, W.-Y. (2018). Alternative Splicing in Neurogenesis and Brain Development. *Front. Mol. Biosci.* *5*, 12.

Szikora, S., Földi, I., Tóth, K., Migh, E., Vig, A., Bugyi, B., Maléth, J., Hegyi, P., Kaltenecker, P., Sanchez-Soriano, N., et al. (2017). The formin DAAM is required for coordination of the actin and microtubule cytoskeleton in axonal growth cones. *J. Cell Sci.* *jcs.203455*.

Tomás Pereira, I., and Burwell, R.D. (2015). Using the spatial learning index to evaluate performance on the water maze. *Behav. Neurosci.* *129*, 533–539.

Torres, V.I., and Inestrosa, N.C. (2017). Vertebrate Presynaptic Active Zone Assembly: a Role Accomplished by Diverse Molecular and Cellular Mechanisms. *Mol. Neurobiol.*

Torres-Méndez, A., Bonnal, S., Marquez, Y., Roth, J., Iglesias, M., Permanyer, J., Almudí, I., O’Hanlon, D., Guitart, T., Soller, M., et al. (2019). A novel protein domain in an ancestral splicing factor drove the evolution of neural microexons. *Nat. Ecol. Evol.* *3*, 691–701.

Vieta, E., Berk, M., Schulze, T.G., Carvalho, A.F., Suppes, T., Calabrese, J.R., Gao, K., Miskowiak, K.W., and Grande, I. (2018). Bipolar disorders. *Nat. Rev. Dis. Primer* 4, 18008.

Vorhees, C.V., and Williams, M.T. (2006). Morris water maze: procedures for assessing spatial and related forms of learning and memory. *Nat. Protoc.* 1, 848–858.

Wagh, D., Terry-Lorenzo, R., Waites, C.L., Leal-Ortiz, S.A., Maas, C., Reimer, R.J., and Garner, C.C. (2015). Piccolo Directs Activity Dependent F-Actin Assembly from Presynaptic Active Zones via Daam1. *PLOS ONE* 10, e0120093.

Walf, A.A., and Frye, C.A. (2007). The use of the elevated plus maze as an assay of anxiety-related behavior in rodents. *Nat. Protoc.* 2, 322–328.

Wilhelm, B.G., Mandad, S., Truckenbrodt, S., Krohnert, K., Schafer, C., Rammner, B., Koo, S.J., Classen, G.A., Krauss, M., Hauke, V., et al. (2014). Composition of isolated synaptic boutons reveals the amounts of vesicle trafficking proteins. *Science* 344, 1023–1028.

Will, T.R., Proaño, S.B., Thomas, A.M., Kunz, L.M., Thompson, K.C., Ginnari, L.A., Jones, C.H., Lucas, S.-C., Reavis, E.M., Dorris, D.M., et al. (2017). Problems and Progress regarding Sex Bias and Omission in Neuroscience Research. *ENeuro* 4, ENEURO.0278-17.2017.

Xie, Z., Bailey, A., Kuleshov, M.V., Clarke, D.J.B., Evangelista, J.E., Jenkins, S.L., Lachmann, A., Wojciechowicz, M.L., Kropiwnicki, E., Jagodnik, K.M., et al. (2021). Gene Set Knowledge Discovery with Enrichr. *Curr. Protoc.* 1.

Yamashita, M., Higashi, T., Suetsugu, S., Sato, Y., Ikeda, T., Shirakawa, R., Kita, T., Takenawa, T., Horiuchi, H., Fukui, S., et al. (2007). Crystal structure of human DAAM1 formin homology 2 domain: DAAM1 FH2 structure. *Genes Cells* 12, 1255–1265.

Ziv, N.E., and Garner, C.C. (2004). Cellular and molecular mechanisms of presynaptic assembly. *Nat. Rev. Neurosci.* 5, 385–399.

Zucker, I., and Beery, A.K. (2010). Males still dominate animal studies. *Nature* 465, 690–690.